Atomic-scale characterization of diamond surfaces and fullerene self-assembly

Dissertation
zur Erlangung des Grades
“Doktor der Naturwissenschaften”
im Promotionsfach Chemie

am Fachbereich Chemie, Pharmazie und Geowissenschaften
der Johannes Gutenberg-UniversitätMainz

Markus Franz Willy Nimmrich

geboren in Georgsmarienhütte

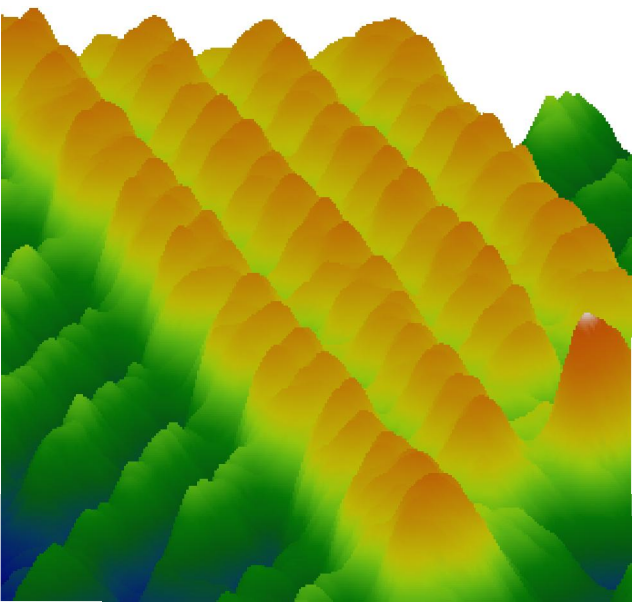

Mainz, den 23. Juni 2012

This dissertation was supervised by *name removed for privacy* and was carried out at the Universität Osnabrück and the Johannes Gutenberg-Universität Mainz from April 2009 to June 2012.

D77 (Dissertation Johannes Gutenberg-Universität Mainz)

Dean of the faculty	*name removed for privacy*
1st report	*name removed for privacy*
	Johannes Gutenberg-Universität Mainz
2nd report	*name removed for privacy*
	Johannes Gutenberg-Universität Mainz
Submitted:	June 2012
Oral examination:	July 16^{th} 2012

Contents

List of Abbreviations

AFM	atomic force microscopy
bct	body-centered tetragonal
CBM	conduction band minimum
CF	Conflat
CVD	chemical vapor deposition
EA	electron affinity
ESR	electron spin resonance
fcc	face-centered cubic
FFT	fast Fourier transformation
FIB	focused ion beam
HOMO	highest occupied molecular orbital
HPHT	high-pressure-high-temperature
HREELS	high-resolution electron energy loss spectroscopy
IGP	ion getter pump
LEED	low-energy electron diffraction
LUMO	lowest unoccupied molecular orbital
MBE	molecular beam epitaxy
NC-AFM	non-contact atomic force microscopy
NEA	negative electron affinity
NV	nitrogen vacancy
ODMR	optically detected magnetic resonance
PEF	paramagnetic endohedral fullerene
PLL	phase-locked loop
PSD	photo sensitive detector
QCM	quartz crystal microbalance
QMS	quadrupole mass spectrometer
RT	room temperature
STM	scanning tunneling microscope
TPD	temperature programmed desorption
TSP	titanium sublimation pump
UHV	ultra-high vacuum
VBM	valence band maximum

1 Introduction

Since their first discovery in stone-age India about 8000 to 10000 years ago[1], diamonds have been an unceasing source of fascination for mankind. In the early ages, this fascination was often expressed by the attribution of magic properties to diamonds. Diamonds were believed to have the power to prevent harm and to grant strength as well as resistance to disease. As a consequence, diamonds were worn as charms by those wealthy enough to afford it, which constitutes the origin of diamond as a most valuable gemstone. And although this superstitious believe in miraculous powers of diamond does of course not withstand scientific examination, it already reflects on the most remarkable characteristics of diamond: unique durability and hardness. With a score of 10 on Mohs scale of mineral hardness, diamond is harder than any other natural material. Because of this, diamond has always been more than just a jewel. Its practical value as a supreme cutting and drilling tool has been exploited since at least 3000 BC[1] and still is today.

Its long history of cultural relevance is also apparent in the fact that diamond was already subject to scientific research in ancient civilizations. This is yet reflected in the name "diamond", which is derived from the ancient Greek "adámas", meaning "unconquerable" or "unbreakable". Centuries of scientific interest in diamond revealed many other unique properties of diamond besides its hardness, most notably its thermal conductivity, which is the highest of all natural materials[2], and its extraordinary chemical inertness.

A completely new chapter of diamond research was opened in the

second half of the 20^{th} century with the development of techniques that allow for the synthesis of artificial diamond. Diamond growth by means of chemical vapor deposition (CVD), for example, enables the synthesis of high purity, single crystalline diamond with well-controlled doping, making diamond a much sought-after material for semiconductor applications beyond the scope of the current silicon-based technology. The early enthusiasm regarding diamond as the next generation semiconductor, however, has faded a bit recently since major obstacles such as the generation of an adequate number of conduction electrons by doping have yet to be overcome.

In the related field of spintronics, on the other hand, CVD diamond has emerged as a most promising material. This is mostly due to the existence of nitrogen-vacancy centers (NV-centers) in diamond, which provide single, individually addressable electron spins. This feature in principle allows for the use of NV-centers as qubits of an atomic-scale quantum computer operated at room temperature. In recent years, this finding has caused a great run towards the implementation of the first fully functional diamond quantum register, following a variety of different approaches[3–8].

This thesis is part of a project funded by the Volkswagen Foundation that itself aims at the realization of such a quantum computer. The fundamental concept followed in this particular approach is to make use of molecular self-assembly of endohedral fullerenes, which can spin-couple to NV-centers, on the diamond surface.

As a first objective, both, the bare and the hydrogen-terminated diamond C(100) surface, had to be suitably prepared and characterized on the atomic scale. This was done done in the framework of this thesis using non-contact atomic force microscopy (NC-AFM). As a result, the first atomically-resolved NC-AFM images of those surfaces are presented in the following. Atomic scale characterization is an indispensable foundation for the second step towards the implementation of the quantum computer, as it allows for the in-detail study of the interaction of fullerenes with aforementioned surfaces. In this context, C_{60} and $C_{60}F_{48}$ adsorption on diamond surfaces were studied with focus on con-

ditions for molecular self-assembly and direct manipulation using an AFM tip. Particular regard is given to the influence of charge transfer doping on the morphology of C_{60} island formation on the hydrogenated diamond surface.

First steps towards the creation of subsurface NV-centers in diamond were taken in cooperation with the group of *name removed for privacy* (AG Quantum, Physics Department, Johannes Gutenberg-Universität Mainz). In particular, argon cations were implanted into the surface of (111) oriented CaF_2 crystals using the focused ion beam technique. The effects of the implantation on the surface were visualized using AFM and are presented in this thesis as well.

Since the diamond quantum computer concept also requires the deposition of unsublimable, endohedral fullerenes on diamond surfaces under ultra-high vacuum (UHV) conditions, ways have to be found to deposit those molecules from solution. The most promising way is deposition by pulse injection[9], which was tested in the framework of this thesis. The tests were performed in a UHV chamber that was custom-designed by me for this and other tasks.

2 Non-contact atomic force microscopy (NC-AFM)

Contents

The main experimental technique used in this thesis is non-contact atomic force microscopy (NC-AFM). This technique will be explained to some detail in this chapter. An introduction into the theory behind NC-AFM is given as well as a description of the experimental realization.

2.1 Theory

Atomic force microscopy (AFM) is a scanning probe microscopy technique and was developed in the 1980s by Quate, Binnig and Gerber[10]. It is related to the more common scanning tunneling microscope (STM)[11], for which Binnig and Gerber have been awarded the Nobel Prize for Physics in 1986. Both techniques, AFM and STM, use a sharp tip as a probe to raster scan the surface. The signal derived from the interaction of probe and surface is then used to compute an image of the surface. The difference between AFM and STM lies in the nature of this interaction. In STM, the interaction is purely electronic in the sense that electrons tunnel from the tip to the sample or the other way round. The exponentially distance-dependent tunneling current can therefore be used to map the electronic states of the surface, which by nature are related to the surface structure. STM allows for atomic-resolution imaging in air, liquids and vacuum environments with relatively little technical and experimental effort. Thus, it quickly became the most commonly used real-space imaging technique on the atomic scale. However, STM has one profound disadvantage: it is limited to conducting surfaces.

In AFM, on the other hand, forces acting between tip and sample are measured, allowing for imaging of insulators as well. This is done by mounting the tip to the end of a small cantilever (usually 100 µm to 200 µm in length and 20 µm to 40 µm in width), as can be seen in Fig. 2.1. If a force is acting on the tip, a change in the cantilever position or oscillation characteristics results. This change can be measured and correlated with the force.

The most commonly used method to detect the cantilever deflection is a beam deflection setup. Here, a laser spot is focused on the back of the cantilever at the tip position. From there, the light is reflected to a photo sensitive detector (PSD). As a result of the photoelectric effect, a small localized current is generated on the face of the PSD by the incident light. This current is converted into a voltage corresponding to the position of the laser spot. Hence, when the cantilever is deflected, so is the laser reflection on the PSD, resulting in an alteration in PSD voltage.

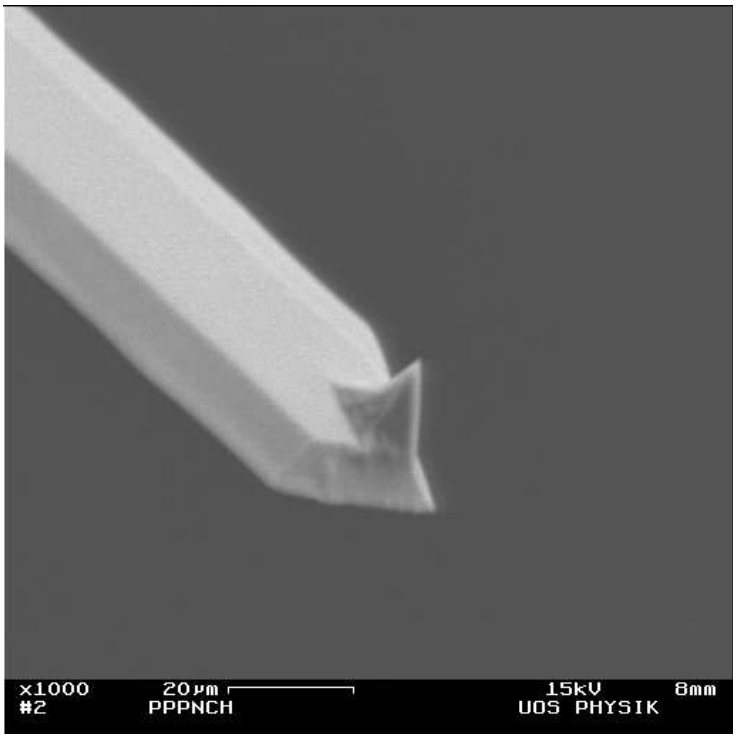

Figure 2.1: Electron microscopy image of an NCH-PPP 300 kHz AFM tip prior to use. Courtesy of J. Lübbe, University of Osnabrück.

The raster movement as well as the approach of the tip to the sample is usually executed by a piezo tube actuator, to which the cantilever or the sample is mounted.

There are several ways to operate an AFM, with NC-AFM being one of them. In general, a difference is made between AFM operated in **contact mode**, **tapping mode** and **non-contact mode**. Those basic categories are partially further divided into submodes as outlined in the following.

Contact mode

As already indicated by the name, the probe is in physical contact with the surface when an AFM is operated in contact mode (Fig. 2.2). The cantilever deflection therefore follows the cor-

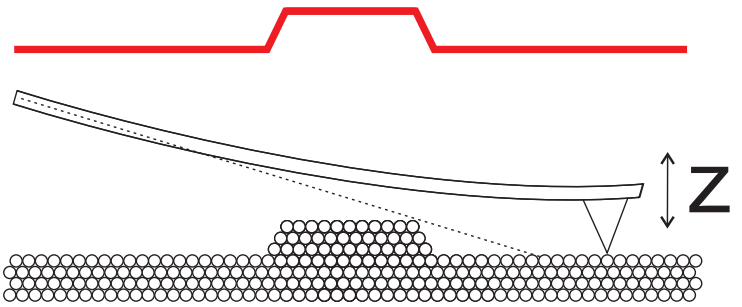

Figure 2.2: AFM operated in contact mode. The cantilever movement is depicted in red.

rugation of the surface when raster scanned, unless there are significant differences in surface hardness. Using Hooke's law ($F = -k\Delta z$), the force acting on the cantilever can be calculated from the height change Δz and the spring constant of the cantilever k. In general, the AFM is operated in the regime of repulsive interaction in contact mode. The interaction area usually involves several hundreds of atoms and is not sensitive to the single atom, with one notable exception: Ohnesorge and Binnig were able to achieve true atomic resolution on the $(10\bar{1}4)$ surface of calcite using contact AFM in 1993 [12].

Constant height

In the constant height mode, the height position of the cantilever is kept constant and does not react to a change in surface corrugation. The deflection of the cantilever is used as the imaging signal for mapping the surface. The deliberate omission of a height-controlling feedback loop eliminates a possible source of error and allows for straight-forward data analysis. In addition, the constant height mode can be operated with a high raster speed, which reduces the influence of thermal drift. As a major drawback, though, this mode can only be used on very smooth surfaces, otherwise unintended collisions between tip and surface features are inevitable.

Constant force

The other possible contact AFM mode is the constant force mode. Here, a constant setpoint for the force acting on the cantilever is set and fed into a feedback loop controlling the distance between tip and surface. When scanning in this mode, the tip is pressed onto the surface with a force equaling the setpoint. When a protrusion of the surface interacts with the tip, this is registered by the stronger cantilever deflection as an increase in force, which causes the feedback loop to increase the tip-surface distance until the measured force matches the setpoint again.

Equivalently, the tip-surface distance is decreased by the feedback loop when the force acting on the cantilever drops below the setpoint. The tip thus traces the surface corrugation and the image information is not longer provided by the deflection of the cantilever but by its distance to the surface. The active distance regulation allows for imaging of rough as well as smooth surfaces, but is limited to a lower scanning speed since the response of the feedback loop requires additional time.

A disadvantage both modes, constant height and constant force, have in common is the strong physical contact between tip and surface. This can cause abrasion of the cantilever tip, resulting in a large tip apex that limits the resolution of the scan. In addition, surface structures may be changed or damaged during the scan. This is less problematic for hard surfaces such as those of single crystals, but can significantly hamper the imaging of susceptible surfaces as often found in biological systems.

In order minimize the contact time and the damage inflicted on the surface, another mode called “intermittent contact” or simply “tapping” is often used.

Tapping mode

In tapping mode, the tip is not in permanent contact with the sample, but only for short periods of time. This is realized by oscillating the cantilever at a fixed frequency using a piezo ac-

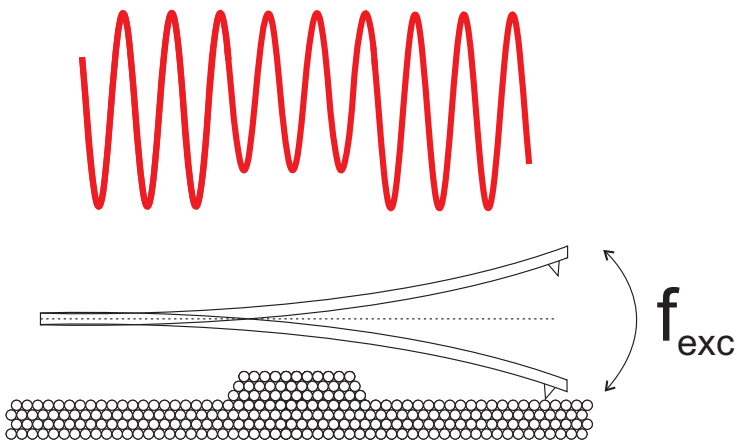

Figure 2.3: AFM operated in tapping mode.The cantilever movement is depicted in red.

tuator and bringing it in close vicinity to the surface (Fig. 2.3). The distance is chosen in such a way that the tip only touches the surface in the lower turning point of the oscillation cycle. This "tapping" contact causes the oscillation amplitude to decrease according to the force acting between tip and surface. This amplitude modulation can therefore be used as the imaging signal.

Tapping-mode AFM of course also enables the use of constant height or constant force mode like in contact AFM, with the difference that the amplitude signal is used for distance regulation instead of the cantilever deflection. Due to the contact being only intermittent, tapping AFM often inflicts less damage on the imaged surfaces. Especially the risk to cut through or drag along adsorbents with the tip is reduced.

Non-contact mode

A further sophistication is the operation of an AFM in non-contact mode (Fig. 2.4). In frequency modulated NC-AFM, the tip is oscillated at its resonance frequency and is raster scanned over the surface in close proximity but without direct physical contact. When the tip is close enough to the surface to interact with the surface force field, a shift in resonance frequency (also called "de-

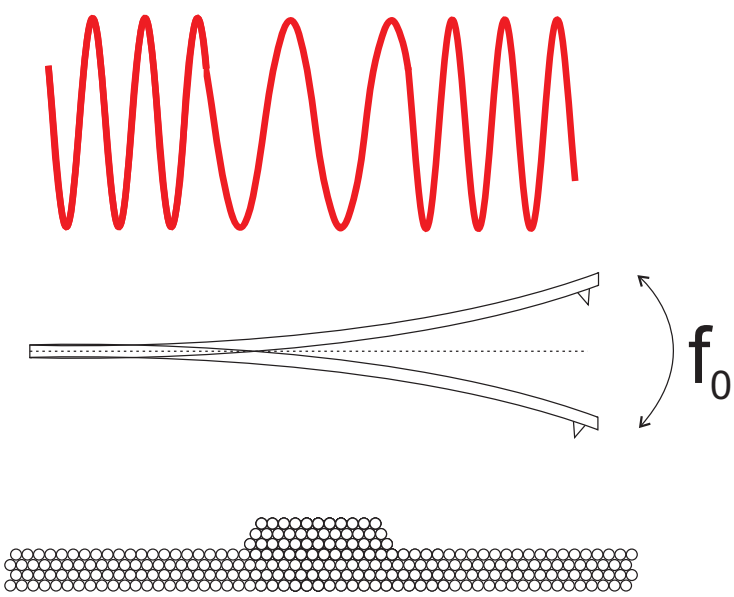

Figure 2.4: AFM operated in non-contact mode. The cantilever movement is depicted in red. In this example, the resonance frequency is decreased over the protrusion. This is only the case when the tip is still far enough away from the surface for attractive forces to be dominant over repulsive forces, which is usually the case in the NC-AFM studies of this thesis. When, on the contrary, the cantilever is operated in the repulsive regime, the resonance shift is towards higher frequencies.

tuning") can be observed. In a simplified picture, the frequency increases upon repulsive interaction and decreases upon attractive interaction[13]. Like the cantilever deflection in contact AFM and the amplitude change in tapping AFM, the detuning therefore is a direct indicator of the forces acting on the tip and can be used to control the tip-surface distance by a feedback loop. This enables the operation of NC-AFM in constant height mode or constant detuning mode.

The relation between frequency shift (Δf) and the overall tip-sample interaction force (F_{TS}) is given by the following equation:

$$\Delta f(z) = -\frac{f_0^2}{kA}\left\langle F_{TS}\cdot q'\right\rangle = -\frac{f_0}{k\pi A^2}\int_{-A}^{A} F_{TS}\frac{(z-q')q'}{\sqrt{A^2-q'^2}}\mathrm{d}q' \quad (2.1)$$

Here, the brackets indicate averaging over one oscillation cycle. As can be seen, the frequency shift is a function of the tip-surface distance z, the cantilever deflection q' (as depicted in Fig. 2.5), the spring constant k of the cantilever, the oscillation amplitude A, the resonance frequency f_0 and of course the tip-sample interaction force F_{TS}. Due to the fact that the tip is not in contact with the sample during scanning, there is no wear affecting the tip. Hence, the tip does normally not degrade

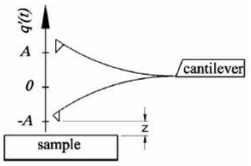

Figure 2.5: Schematic view of the cantilever oscillation[14].

and can even be purposely functionalized by the attachment of single molecules or atoms. Since the tip apex is what mainly defines the resolution limit, NC-AFM allows for surface imaging on the atomic scale, as was first demonstrated by F.J. Giessibl in 1995 on the silicon Si(111)-(7×7) surface[15]. Further development of this technique has been done since then, now even allowing for the atomically resolved imaging of single molecules on a surface[16].

As a drawback, the technical effort necessary to achieve atomic resolution is substantial. In order to detect frequency shifts corresponding to the atomic corrugation of the surface, the cantilever oscillation has to be of extraordinary high quality. While the quality factor Q_C of a cantilever is an intrinsic characteristic, the quality factor Q of the cantilever oscillation is strongly influenced by damping. Hence NC-AFM works best under vacuum conditions, where the damping by friction is minimized.

In addition, a low background pressure is also necessary to keep the surface free of unwanted adsorbates from the environment. Since it takes only an exposure to 1 L (1 s at 1×10^{-6} mbar background pressure) for a surface with a sticking coefficient of 1 to be covered with a monolayer of adsorbates[17], an NC-AFM is usually operated in UHV. Operation under liquid conditions is, however, possible[18], but requires considerable more effort to improve the signal-to-noise performance of the instrument[19].
The experimental setup of the NC-AFM used in this thesis is described in detail in Sec. 2.3.

2.2 Forces

Since AFM is based on the measurement of forces interacting between tip and sample, it is expedient to characterize those forces in a bit more detail concerning their origin and range. Hence, the most significant tip-sample interaction forces divided by range are explained in the following.

Long-range forces

Van-der-Waals forces

Van-der-Waals is the overarching term for three related, but not identical dipole interaction forces called *Keesom* interaction, *Debye* interaction and *London* dispersion interaction.

Keesom interaction describes the forces acting between two permanent dipoles[20], while **Debye interactions** refers to the interaction of a dipole and a polarizable molecule that is turned into a temporary dipole under the influence of a neighboring dipole[20]. The **London Dispersion force**, which is often inaccurately used synonymously with Van-der-Waals force as a whole, acts between non-polar objects. It is ascribed to quantum fluctuations that cause the spontaneous polarization of molecules, which then induce temporary dipole moments into neighbored molecules[20,21].

In NC-AFM, all Van-der-Waals forces are considered long-range forces (up to 100 nm distance) and therefore influence the resonance frequency of the cantilever long before scanning distance is reached. Since the London dispersion is affecting non-polar molecules, Van-der-Waals forces are present whenever two objects of any kind are approximated. Here, the force gradient as a function of the distance is highly dependent on the shape of the objects. For the most simple case of two point-shaped objects, the potential decreases with the distance to the sixth power ($V \sim z^{-6}$)[22]. In a more realistic model, the tip is resembled by a parabola and the surface by a plane perpendicular to the center

line of the parabola. In this geometry, the overall Van-der-Waals potential amounts to:

$$|V_{VdW}(z)| = -A_H \frac{R}{6} \frac{1}{z} \tag{2.2}$$

In this equation[23], explaining the long-range character of Van-

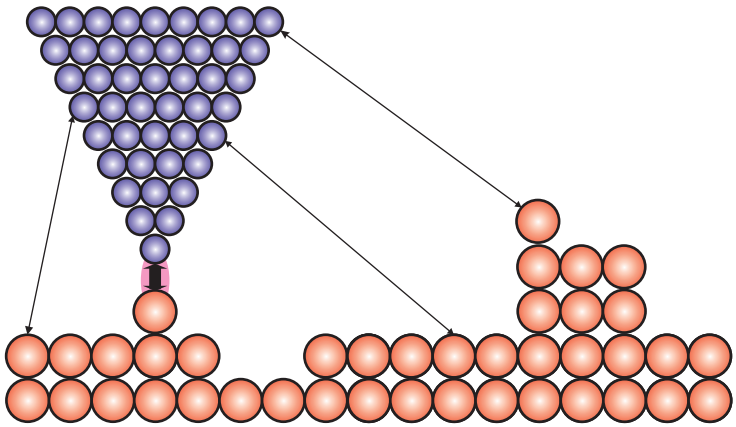

Figure 2.6: Model of a tip scanning a surface. The short-range forces (short arrow on magenta background) are strongly localized and therefore in principle sensitive to the single atom. Long-range forces (long arrows) are often affecting large parts of the tip and thus do not enhance contrast formation.

der-Waals forces, A_H is the Hamaker constant[24] and R is radius of the tip apex.

In NC-AFM, the Van-der-Waals forces are in general considered to provide a constant force offset during the scan. This assumption is justified since Van-der-Waals is an interaction between large parts of tip and surface (see Fig. 2.6). Therefore, those forces are not very sensitive to the single atom and do not contribute to contrast formation on the atomic scale.

Coulomb forces

Another long-range force important to AFM is the Coulomb force. This force accounts for the interaction of charged objects. For two point charges q_1 and q_2 of distance z, the Coulomb potential is given by the following equation:

$$|F_{Coul}(z)| = \frac{1}{4\pi\epsilon_0} \frac{q_1 q_2}{z} \tag{2.3}$$

As can be seen, the Coulomb potential decreases linearly with the distance and increases by the product of the two charges. In AFM, Coulomb forces often arise when imaging insulators, because the insulating nature of the surface does not allow for charge carriers to dissipate. The coulomb interaction of the tip with such a charged surface is delocalized in a manner similar to Van-der-Waals interaction, affecting large parts of the tip and surface. Since it is not specific to the last tip atom and the single atom on the surface, it does not contribute to image resolution on the molecular scale. Unlike the Van-der-Waals interaction, the non-local Coulomb force affecting the measurement can be nullified by applying an electric potential of the same value but reverse direction between tip and sample. If this compensation is done anew in every raster point during scanning, the resulting "charge map" can even provide additional surface information. This AFM modification is called Kelvin Probe Force Microscopy (KPFM)[25] and can, for example, be used to visualize charge transfer effects, localized charged patches or catalytic processes on a surface.

It has to be kept noted, however, that, in case of ionic crystals, the surface ions can exhibit a strongly localized electrostatic force on the the tip if the tip is charged. In this case, the Coulomb force naturally contributes to contrast formation on the atomic scale.

Short-range forces

Pauli exclusion forces

Pauli exclusion forces arise from a fundamental law of quantum mechanics, the Pauli principle. It states that two fermions (for example electrons) have to differ in at least one quantum number if they are to occupy the same space. As a consequence, a single molecular orbital can contain a maximum of two electrons and this only if those two electrons differ in their spin quantum number. Hence, a repulsion force arises whenever two fully occupied orbitals are approximated. Due to the underlying principle, this force is called "Pauli exclusion force" or "exchange interac-

tion force".

Covalent binding force

If two half-filled orbitals overlap, on the other hand, a covalent bond can be formed. The strength of the covalent bond depends on the overall orbital overlap. For example, there is stronger overlap between carbon atoms in the sp_3 hybridization than in the sp_2 hybridization, explaining the much more stable interatomic bonds in diamond compared to graphite. Like the Pauli exclusion forces, binding forces are extremely short range, the bond length typically is in the range of 100 pm to 200 pm [22].

Combination of short and long range forces

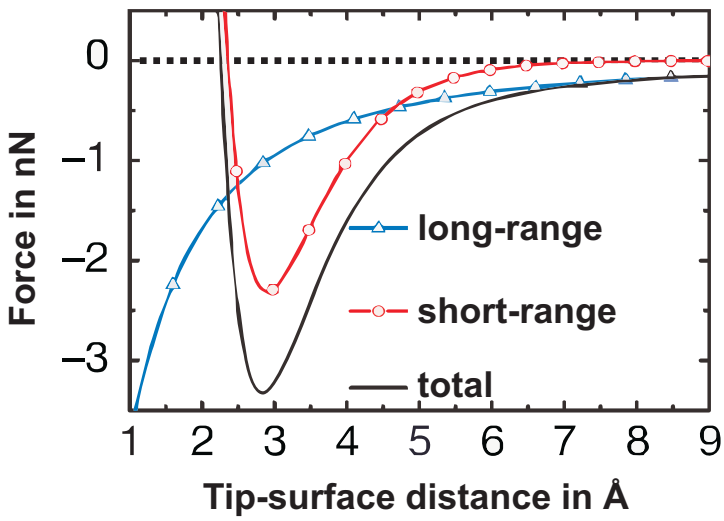

Figure 2.7: Tip-surface forces. [26]

When quantifying the distance dependence, a Lennard-Jones potential is often used, treating short-range interactions with a z^{-12} distance dependence and long-range interactions with a z^{-6} dependence. The derivative of the sum of short- and long-range potentials results in a force-distance diagram as shown in Fig.

2.7. However, the applicability of this model to the real tip-surface interaction is limited since it does not adequately account for the influences of the tip geometry to the interaction forces. In addition, this model is not sufficient to describe the force-distance dependence for scanning under ambient conditions because it does not consider capillary forces that usually arise between a water adlayer on the surface derived from air humidity and the AFM tip. The model also neglects oscillatory solvation forces that occur when doing AFM in liquids[27]. Hence, the Lennard-Jones potential in this form is, strictly speaking, only of (limited) applicability for UHV AFM.

2.3 NC-AFM setup

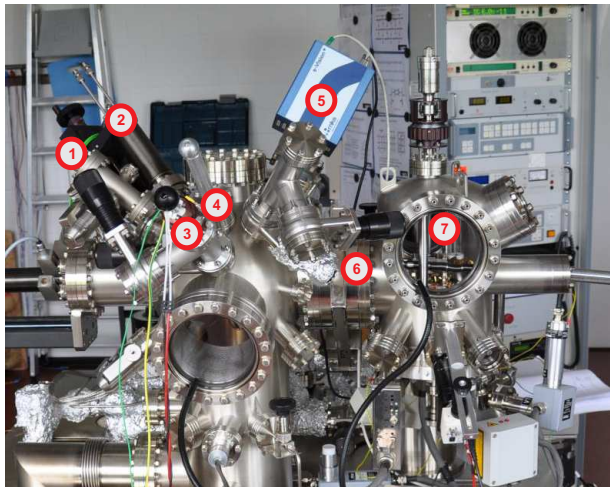

Figure 2.8: Photograph of the NC-AFM UHV chamber. (1) sputter gun, (2) QCM, (3) molecule sublimator, (4) crystal cleaver, (5) QMS, (6) gate valve, (7) NC-AFM scan head.

For the NC-AFM measurements presented in this thesis, a commercial VT-AFM 25 (Omicron Nanotechnology, Taunusstein, Germany) in combination with a Nanosurf easyPLL Plus phase-locked loop detector and amplitude controller (Nanosurf, Liestal, Switzerland) was used. The VT-AFM allows for STM and AFM imaging at temperatures ranging from 25 K to 1500 K. The AFM is operated in a UHV chamber with a background pressure below 1×10^{-10} mbar. As can be seen in Fig. 2.8, the UHV systems consists of the AFM chamber and a preparation chamber, separated by a gate valve. The preparation chamber allows for the preparation of tips and samples without leaving the UHV environment. The tips used in this thesis (Nanosensors PPP-NCH) are silicon cantilevers featuring quality factors of 20000 to 40000 and eigenfrequencies of about 300 kHz. The tips were Ar^+ sputtered prior to use in order to remove contaminants.

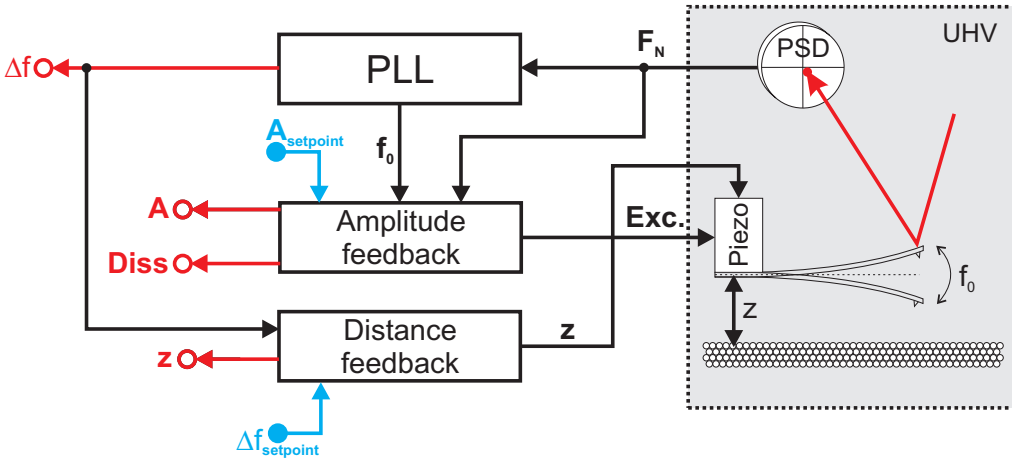

Figure 2.9: Setup of an NC-AFM.

NC-AFM operation

An outline of the NC-AFM setup is depicted in Fig. 2.9. As can be seen, two feedback loops and one phase-locked loop (PLL) are used to process the deflection signal.

The PLL tracks the cantilever oscillation frequency to maintain excitation at resonance. In order to do so, the PLL works as a demodulator, extracting the frequency shift and feeding it into the distance feedback loop. The detuning is of course also mapped in each raster point and displayed as the main imaging signal.

The amplitude feedback loop compares the actual cantilever amplitude as derived from the PSD signal (F_N) with a setpoint value for every oscillation cycle. The amplitude feedback then generates the excitation signal for the cantilever oscillation.
When the microscope is operated in the *constant amplitude mode*, as was done in this thesis, the feedback also regulates the excitation amplitude to the constant setpoint value anew in each cycle. The actual amplitude, which is measured in every raster point, can be mapped as an amplitude image. In addition, an image displaying the difference between the actual oscillation and the excitation amplitude can be recorded, mapping the energy dissipation of the tip due to the interaction with the surface.

The function of the distance feedback loop was already described to some degree in Sec. 2.1. It regulates the distance between tip and sample by moving the piezo actuator, onto which the cantilever is mounted, in order to keep the detuning to a setpoint value. The tip-surface distance is therefore recorded in every raster point and displayed as the "topography" image.

NC-AFM images are usually obtained by line-by-line raster scanning the surface with a fixed raster speed. For each line, a forward and a backward scan is done, resulting in two different sets of images. Since detuning, topography, amplitude and dissipation are mapped, this results in a total of eight images for one scan frame.

3 Substrates and molecules

Contents

Substrates and molecules used for this thesis are described in the following.

The main substrate is diamond, of which two surface modifications were studied with NC-AFM (Chap. 7 and Chap. 8): the pure **C(100)**(2×1) surface and the hydrogen-terminated **C(100)**(2×1)**:H** surface. In addition, **CaF_2(111)** was used in the framework of an AFM study regarding the effect of focused ion implantation (Chap. 6).

Since the main subject of the thesis is directed towards the implantation of a molecular quantum computer, the adsorption of two kinds of fullerenes, $\mathbf{C}_{60}$ and $\mathbf{C}_{60}\mathbf{F}_{48}$ on diamond surfaces was studied.

On a side note, salicylic acid was used together with several solvents in pulse injection experiments. In the aim of this study,

however, the only significant quality of salicylic acid and its solvents is their respective solubility, other properties are of no importance. Hence, those chemicals are given no further attention in the following chapter. In order to evaluate the potential of molecule deposition by pulse injection, Au(111) was imaged with STM. The relevance of this substrate, however, is limited to the calibration of the pulse valve and will therefore also not be presented in detail in the following chapter.

3.1 Substrates

Diamond C(100)

In this section, the emphasis is on the properties of the specific diamond samples used in the framework of this thesis. For a more detailed description of general characteristics of diamond, please refer to Chap. 4.

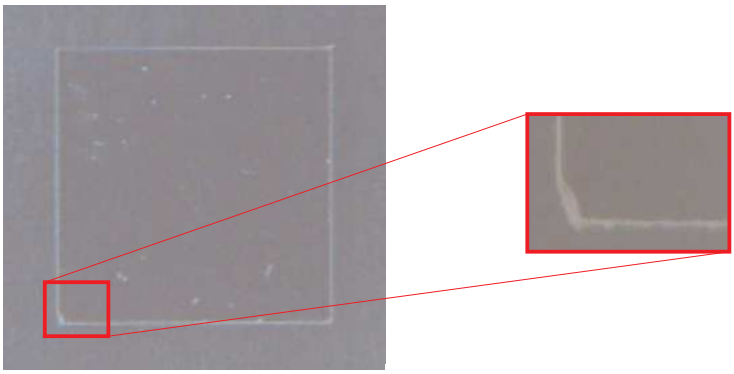

Figure 3.1: Light microscopy image of a diamond sample. The cut in the lower left corner serves as a distinctive feature to distinguish the two main sides of the sample.

The diamond samples used for this thesis (Fig. 3.1) were purchased from Diamond Detectors (Poole, UK). They are 3.0 mm × 3.0 mm × 0.5 mm in size and of type IIa (see Chap. 4). This means the samples are undoped and therefore non-conducting, which is already indicated by their colorless appearance. The total impurity concentration is below 1 ppm with nitrogen being the largest portion. The diamond samples have been synthesized by chemical vapor deposition (CVD) and were polished by the supplier in order to smoothen the surface. The diamonds are monocrystalline with the main sides featuring a (100) surface (Fig. 7.7).

Two types of samples were used, differing in the polishing grade. This results in different surface roughnesses, amounting to R_A =0.10 nm for the more polished and R_A =0.31 nm for the less polished samples. This roughness values, however, were determined by the manufacturer using an optical profiler (Veeco Wyko NT9100), which averages over a large surface area (1 mm^2).

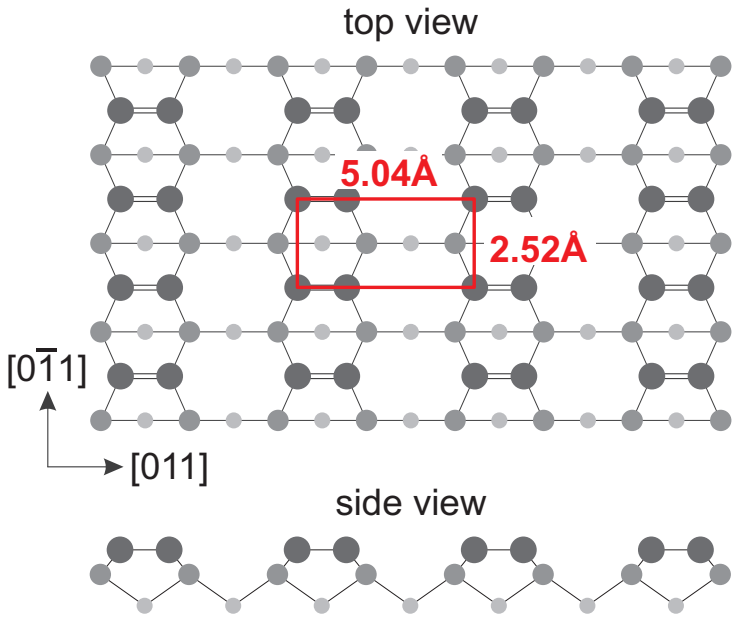

Figure 3.2: Model of the diamond C(100)(2 × 1) reconstructed surface. Protruding carbon atoms are displayed larger and with darker color. The red box represents a surface unit cell.

Hence, the obtained roughness parameters do not necessarily provide evidence for a smooth surface on the atomic scale. This is supported by contact AFM measurements (Fig. 3.3) that show a flat, but strongly furrowed surface on the nanometer scale.

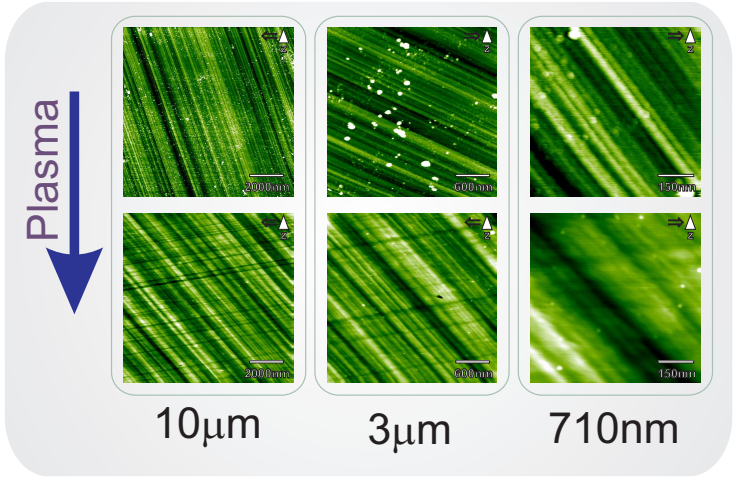

Figure 3.3: Tapping AFM topography images of a (100) surface of a diamond sample before (upper row) and after (lower row) plasma treatment. The image scale decreases from left to right.

However, it was shown by Stallcup *et al.* that it is possible to increase the terrace size by exposure of the diamond surface to a hydrogen plasma[28]. Even more importantly, the plasma treatment is capable of removing non-diamond carbon as well as organic impurities from the surface. It is therefore the procedure of choice when aiming at a clean and well-defined hydrogen-terminated surface. Consequently, all the diamond samples used in this thesis were plasma cleaned prior to use. This was done at the group of Prof. *name removed for privacy* (Molecular Nanoscience Group, ISMO, Université de Paris XI) with the help of *name removed for privacy*.

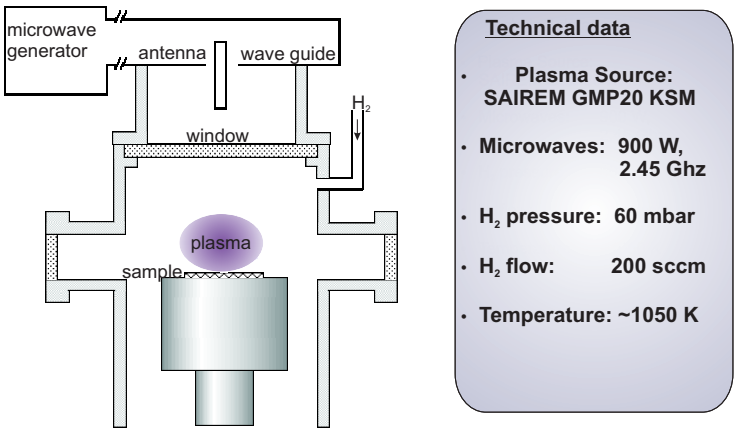

Figure 3.4: Experimental setup of the plasma chamber.

The experimental setup of the plasma chamber is depicted in Fig. 3.4. A photograph of samples and plasma during the process can be seen in Fig. 3.5. The diamond plates are placed on an extendable column, facing a window through which a microwave beam (λ =2.45 GHz, P =950 W) is directed onto the samples. The chamber is evacuated to high vacuum (2×10^{-6} mbar) and subsequently filled with hydrogen. When a pressure of 2 mbar is reached, a hydrogen plasma can be ignited using microwave radiation. The hydrogen concentration is further increased to a partial pressure of 60 mbar, then the diamond samples are lifted into the plasma. A hydrogen flow of 200 sccm is maintained during operation in order to keep the substrate in incessant contact with atomic hydrogen. The samples are exposed to the plasma for 1 h at a temperature of 1050 K. The sample temperature originates solely from the plasma, no additional annealing is re-

Figure 3.5: Diamond samples exposed to the hydrogen plasma.

quired. Consequently, the temperature can be steered by careful positioning of the samples in the conus of the plasma. A difference of 1 cm in distance towards the plasma center roughly equals a change in sample temperature of 20 K to 30 K.

As a result of the polishing, the samples feature a distinctive stripe-like surface pattern prior to plasma exposure (see Fig. 3.3 upper row). Line profiles taken perpendicular to these polishing marks (Fig. 3.6) reveal a width of 20 nm to 50 nm and an average corrugation of 3.4 nm. In addition, several adsorbates

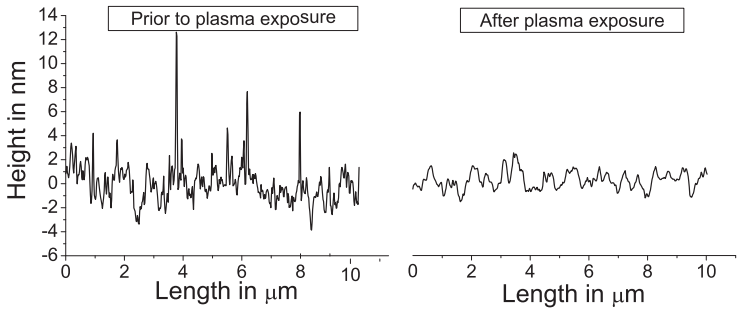

Figure 3.6: Line profiles of the C(100) surface before and after plasma treatment. The profiles were taken perpendicular to the polishing stripes on large-scale tapping AFM images.

cover the surface. Those impurities are most likely remnants of the polishing agent used by the supplier, a mixture of salts and nanodiamonds.

The influence of the plasma preparation is visible in Fig. 3.3. After the plasma treatment, the stripes are significantly less pronounced. The corrugation decreased to 1.4 nm, less than half of the previous value (see Fig. 3.6). In addition, the width of the polishing marks increased significantly to values of 50 nm to 200 nm. Also, the impurities ascribed to the polishing process were removed by the plasma. Overall, the plasma treatment led to a much cleaner and smoother surface.

Additionally, the diamond surfaces are almost perfectly hydrogen-terminated after the plasma preparation. Hence, a transition from C(100)-(2 × 1) to C(100)-(2 × 1):H has taken place. As explained in more detail in Chap. 4, the hydrogen-saturated surface is largely inert and stable for months even when exposed to air. The lifetime of the hydrogen layer can be further enhanced by storage under vacuum conditions and under dark, since the

hydrogen layer is photo sensitive to some degree[29]. For a detailed description of the properties of diamond and the characteristics of the diamond surfaces studied please refer to Chap. 4.

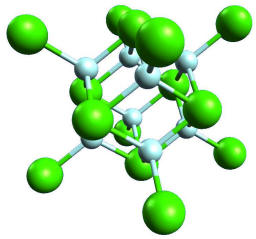

Figure 3.7: Crystal structure of CaF_2. Cyan: F^-, green: Ca^{2+}

Calcium fluoride $CaF_2(111)$

Calcium fluoride (CaF_2) is a halide condensating in the fluorite structure (see Fig. 3.7) with a lattice constant of 5.45 Å[30]. In this crystal lattice, the calcium cations are arranged in the face-centered cubic (fcc) structure while the fluoride anions occupy the tetrahedral holes in between. Calcium fluoride is insulating due to its large band gap of E_{gap} =12.1 eV[31] and a wide-range light transmitter (transmission range: 130 nm - 9 µm; see Fig. 3.9).

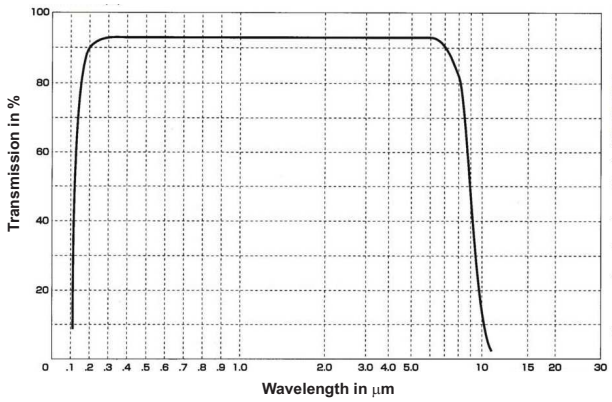

Figure 3.9: Transmission spectrum of CaF_2[32].

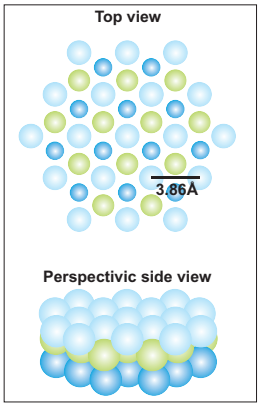

Figure 3.8: Model of the $CaF_2(111)$ surface. Cyan/blue: F^-, green: Ca^{2+}

The natural cleavage plane is the (111) plane. Since the cleaving occurs between two adjacent fluorine layers[33,34], the (111) plane created by cleaving is always fluorine terminated. A model of the $CaF_2(111)$ surface is shown in Fig. 3.8. Here, the topmost fluoride ions are arranged hexagonally with a nearest-neighbor distance of 3.86 Å.

The calcium fluoride samples used in this thesis were purchased from Korth Kristalle (Kiel, Germany). The crystals were annealed *in-situ* (1 h at 620 K to 650 K) prior to use to remove adsor-

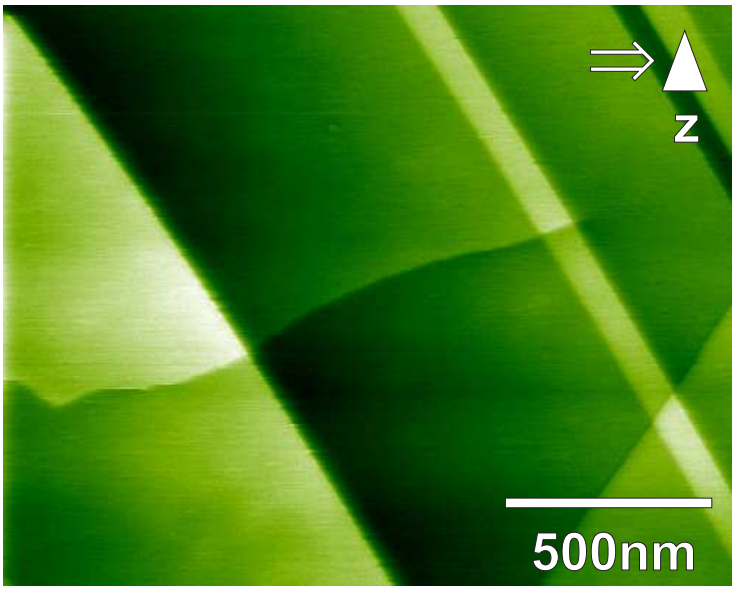

Figure 3.10: Large-scale NC-AFM topography image showing the $CaF_2(111)$ surface of a newly cleaved crystal. The surface usually features a large terrace size (several μm^2) and a low impurity concentration.

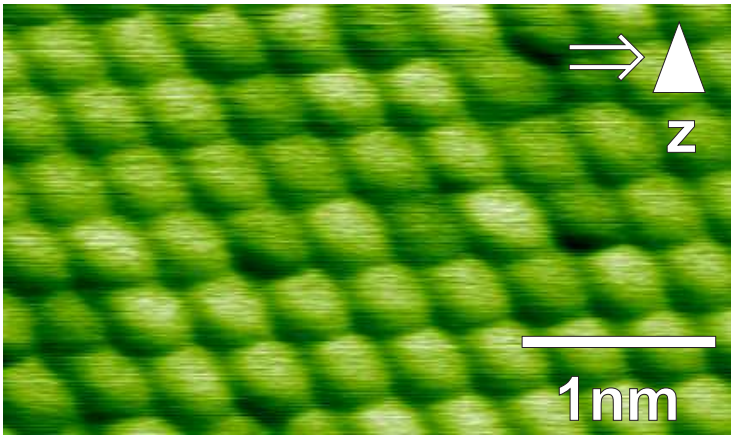

Figure 3.11: Small-scale NC-AFM topography image of the $CaF_2(111)$ surface, resolving single ions.

bates from air. Afterwards, the crystals were cleaved in order to prepare a clean (111) surface. Subsequent annealing (1 hour at 565 K to 580 K) removes charges that emerge as a result of the cleaving. The so prepared surface features atomically flat terraces that extend over several square micrometer (see Fig. 3.10). The surface is largely free of impurities and can be imaged with

NC-AFM in atomic resolution (Fig. 3.11).

3.2 Molecules

C_{60}

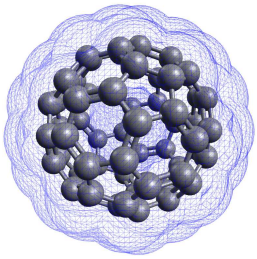

Figure 3.12: Geometric structure and Van-der-Waals frame of C_{60}.

The C_{60} used in this thesis was purchased from MER Corporation (Tucson, Arizona) and has a purity of 99.95 %. The geometrical and the Van-der-Waals structure is depicted in Fig. 3.12. The all-carbon molecule, which has a Van-der-Waals diameter of 10.0 Å, consists of twelve pentagonal and twenty hexagonal subunits. These polygons are arranged in such a way that every pentagon is surrounded by five hexagons. Therefore, every carbon atom is part of both, a pentagon as well as a hexagon subunit[35]. Consequently, every carbon atom is bound to three other carbon atoms over one double bond and two single bonds, which would typically be described as a sp^2 hybridization. However, a pure sp^2 hybridization requires the participating carbon atoms to be arranged completely in plane like in graphite, which is obviously not the case for C_{60}. To account for this "carbon buckling", the nature of the carbon hybridization in case of C_{60} fullerenes can best be described as a mixed state between sp^2 and sp^3 hybridization. Due to the stronger proportion of sp^2, this intermediate hybridization is sometimes described as $sp^{2.3}$[36]. Furthermore, the double bonds are localized in the hexagons, which is why the molecule is not completely conjugated[37].

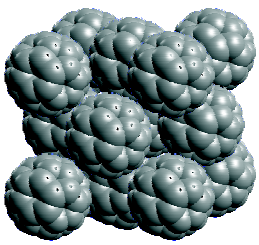

Figure 3.13: Crystal structure of C_{60}.

At room temperature, the C_{60} fullerenes condensate in an fcc structure (see Fig. 3.13) with the lattice constant being 14.15 Å, resulting in a mass density of $\rho = 1.65\,\mathrm{g/cm^3}$[38]. In this condensed structure, which is called fullerite, the fullerenes are bound only by Van-der-Waals interaction and sublimate at a temperature of about 870 K at normal pressure[39]. Under UHV conditions, sublimation already starts at 510 K (see Fig. 3.14). The pure Van-der-Waals character of intermolecular interaction is also apparent in the enthalpy of sublimation, which amounts to 1.65 eV[40].

Crystalline C_{60} is semiconducting with a band gap determined to be 1.5 eV to 2.3 eV, depending on the measuring technique used[41]. Due to the fact that a C_{60} fullerene is primarily sp^2 hybridized, it is an excellent electron acceptor (electron affinity χ =2.7 eV[42]). This is especially true for bulk C_{60} as in fullerite, because the energy gap between the lowest unoccupied

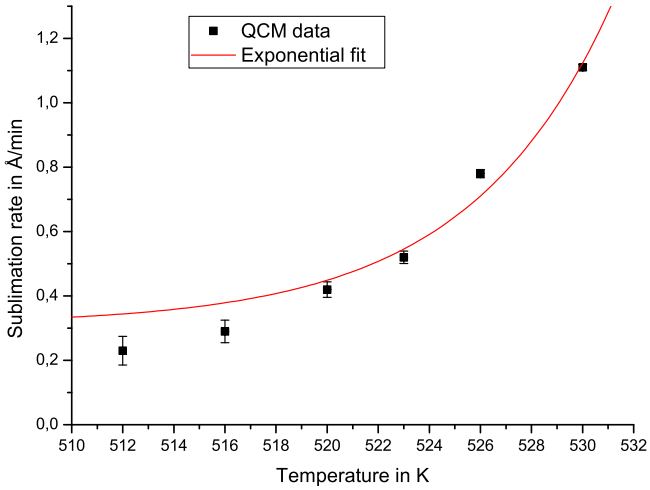

Figure 3.14: C_{60} sublimation behavior determined by QCM under UHV conditions.

and the highest occupied electronic state decreases significantly upon transition from the isolated molecule to the molecule bound in a crystal lattice[43]. This can be understood when looking at the Coulomb interaction that arises from the transfer of an electron to the lowest unoccupied electronic state of a fullerene. In case of the single fullerene, inclusion of another electron leads to an *intramolecular* relaxation of the electrons already present, the molecule is polarized[44]. In case of the fullerene bound in a crystal lattice, on the other hand, the polarizability extends across neighboring molecules as well. Hence, the overall coulomb repulsion between the additionally accepted electron and the existing electrons of the acceptor fullerene is lower when the fullerene is solidly bound in a fullerite crystal instead of being isolated. As a result, the energy gap between the highest occupied and the lowest unoccupied molecular orbital (HOMO and LUMO) of a single C_{60} molecule is considerably larger than the energy difference between conductance band minimum (CBM) and valence band maximum (VBM) of fullerite (1.75 eV to 1.98 eV[43]). In combination with a surface that has a negative electron affinity and is therefore readily donating electrons, electron transfer can be induced from the surface to bulk-like fullerenes (see Chap. 8).

As described in detail in Chap. 4, C_{60} can also be used as a carrier molecule for single atoms. In this case, the foreign atom (for example nitrogen) is encapsulated in C_{60} by ion bombardment, allowing for a stable storage of the atom.

$C_{60}F_{48}$

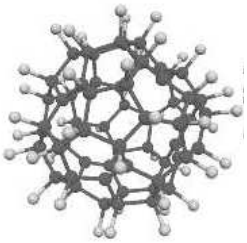

Figure 3.15: Geometric structure of $C_{60}F_{48}$

The $C_{60}F_{48}$ used in this thesis was provided by Dr. *name removed for privacy* from the Jožef Stefan Institute (Ljubljana, Slovenia) and has a purity of $> 96\,\%$. $C_{60}F_{48}$ is the fullerene with the highest grade of fluorination that can be selectively synthesized. Compared to completely fluorinated $C_{60}F_{60}$, twelve carbon atoms do not bind to a fluorine atom, but remain unsaturated (Fig. 3.15). The non-uniform distribution of the fluorine atoms results in a distorted geometry and the existence of two isomers[45]. Contrary to C_{60}, $C_{60}F_{48}$ condensates in the body-centered tetragonal (bct) with lattice constants of $a = 11.85\,\text{Å}$ and $c = 17.91\,\text{Å}$[46]. This is due to the much weaker intermolecular interactions in solid $C_{60}F_{48}$, resulting in a sublimation enthalpy of $1.13\,\text{eV}$[47].

The use of $C_{60}F_{48}$ in this thesis is motivated by its extraordinary high electron affinity, which amounts to $4.06\,\text{eV}$[48]. This attribute makes $C_{60}F_{48}$ an almost ideal molecule in order to study the electron transfer from hydrogenated diamond surfaces into the molecule in a transfer doping process[49].

4 Diamond

Contents

Since the main focus of this thesis is on the study of diamond surfaces, a thorough description of the nature of this substrate is expedient. This is provided in the following chapter, which highlights the most important diamond properties as well as its synthesis and application. Special attention is given to the C(100) surfaces of pure and hydrogen-terminated diamond.

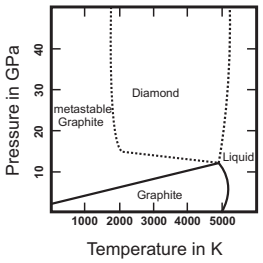

Figure 4.1: Phase diagram for carbon as derived from experimental studies[50].

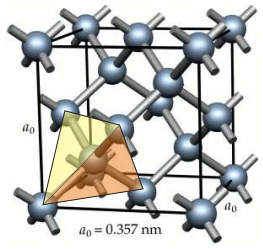

Figure 4.2: Crystal structure of diamond[53]. For illustration, one carbon tetrahedron was added (orange/yellow).

4.1 Properties of diamond

Diamond structure and characteristics

Due to the electronic configuration of carbon ($1s^2\ 2s^2\ 2p^2$), this element does occur in all possible hybridizations (sp^1, sp^2, sp^3). Therefore numerous allotropes of carbon exist, most notably graphite and diamond. Graphite is the most stable polymorph under standard conditions, while the diamond phase is only metastable (see figure Fig. 4.1). Due to the high activation energy of $E_A = 11.0 \pm 0.8\,\mathrm{eV}$[51], however, no significant transformation of diamond into graphite takes place at standard conditions[52].

In the diamond modification, all carbon atoms are sp^3-hybridized. In this hybridization, the $2s$-orbital is combined with the three $2p$ orbitals in order to form four uniform sp^3-hybridized orbitals, each containing one electron ($1s^2\ 2s^2\ 2p^2 \rightarrow 1s^2\ 4[sp^3]$). Since it is energetically favorable for the binding electrons to be as far away from each other as possible, the four hybridized orbitals align tetrahedrally with an angle of 109.5° between each other. Because of this orbital configuration, every carbon atom in diamond is covalently bound to four other atoms by single bonds in form of a tetrahedron with a C—C distance of 154 pm[54]. The diamond lattice is therefore of the fcc bravais type with a lattice constant of 0.357 nm[55] and a twofold base having the coordinates (0,0,0) and (1/4,1/4,1/4), as can be seen in Fig. 4.2.

Although this crystal structure was named for diamond, carbon is not the only element bound in the diamond cubic type. Because of their identical valence configuration, one would expect other elements of the carbon periodic group (IUPAC group 14) to exist in tetrahedral arrangements as well. This is, however, only the case for silicon, germanium and to some degree for tin (below 286 K). In case of lead, relativistic effects on electrons close to the nucleus (s-electrons) have to be taken into account, resulting in a shift in the electronic configuration. As a result, lead does condense in the simple fcc crystal structure.
A diamond cubic structure in which the two base coordinates are occupied by two different elements is called a zincblende structure. Most notably, type III/V semiconductors like gallium-arsenide and indium-antimonide exhibit a zincblende structure[56].

Due to the fact that only every second tetrahedral hole is occupied by a carbon atom, the atomic packing factor of diamond amounts to only 0.34. The atomic density of $1.76 \times 10^{23}\,\mathrm{cm}^{-3}$, however, is the highest of all elements known because of the small C—C bond length (154 pm). This leads to a mass density of $\rho = 3.52\,\mathrm{g/cm}^3$. The short length of the C—C bond in combination with the very high C—C binding energy of 7.4 eV/bond[57] results in a variety of unique electronic, mechanical, optical and thermal characteristics, which make diamond a multifunctional material[2,54,58]. Those characteristics are discussed in the following.

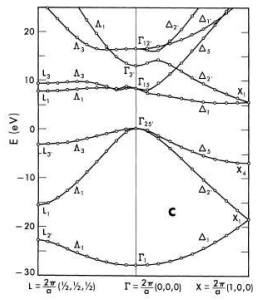

Figure 4.3: Band structure of diamond[59].

Electrical conductivity

Undoped diamond is a bulk insulator due to its band gap of 5.5 eV[59] (see band structure in Fig. 4.3), resulting in a high intrinsic resistivity of $\rho > 1 \times 10^{42}\,\Omega\,\mathrm{cm}^{-1}$. However, the band gap can be drastically reduced by doping the diamond, even allowing for the fabrication of semiconducting diamond[54].

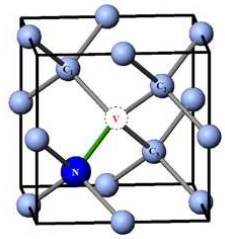

Figure 4.4: NV-center in diamond[60].

The most commonly used dopants in case of diamond are boron, nitrogen and phosphorus. Boron doping results in p-type semiconductivity while phosphorus or nitrogen doping make for an n-type semiconductor. Nitrogen implementation, in addition, is especially interesting for the selective creation of nitrogen vacancy centers (see Fig. 4.4) in diamond, which are photoluminescent and carry an electron spin. The targeted manipulation and control of those electron spins is of great importance with regard to the realization of a nanoscale quantum computer (see Sec. 4.1 for further details).

Hardness

The high C—C binding energy and small inter-atomic distances result in an extraordinary hardness. With a score of 10 on Mohs scale of mineral hardness, diamond is the hardest known natural material. Only a very small number of synthesized materials reach similar hardness, most notably aggregated diamond nanorods or cubic boron nitride[61]. The extraordinary hardness

makes diamond an ideal tool for many cutting, drilling or polishing applications. This is the main reason for the large industrial demand for diamond. Despite its exceptional hardness, diamond is relatively brittle and can be cleaved along certain crystal directions. The cleavage plane requiring the lowest applied pressure is the (111) plane[62].

Optical properties

As can be seen in Fig. 4.5, diamond exhibits broad band optical transparency, extending from the ultraviolet regime to the far infrared.
In combination with a high thermal conductivity (see below),

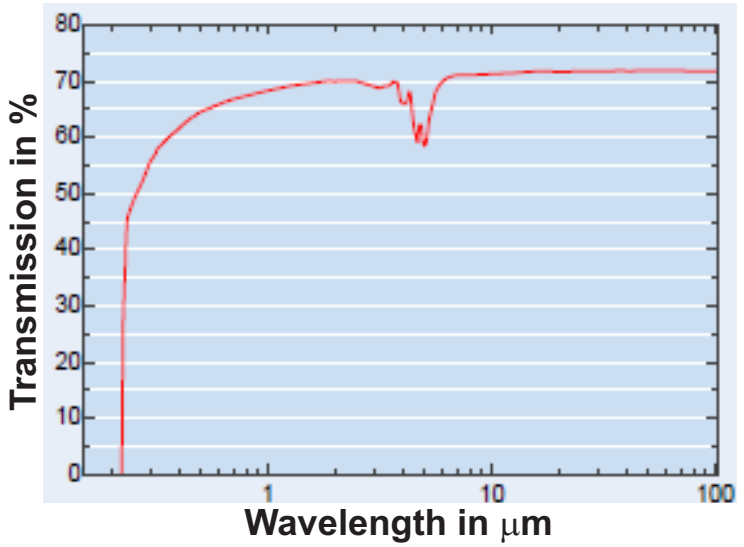

Figure 4.5: Optical transmission spectrum of diamond[63].

this makes diamond a promising window material for high power transmission applications like gyrotron microwave emission oder high-power CO_2 lasers, emitting light in the far infrared regime. In addition, diamond has a very high refractive index of 2.3 to 2.4 (depending on wavelength), which can be exploited to design high-efficiency reflectors[54]. It also has an above average dispersion coefficient of 0.044[64].

Thermal conductivity

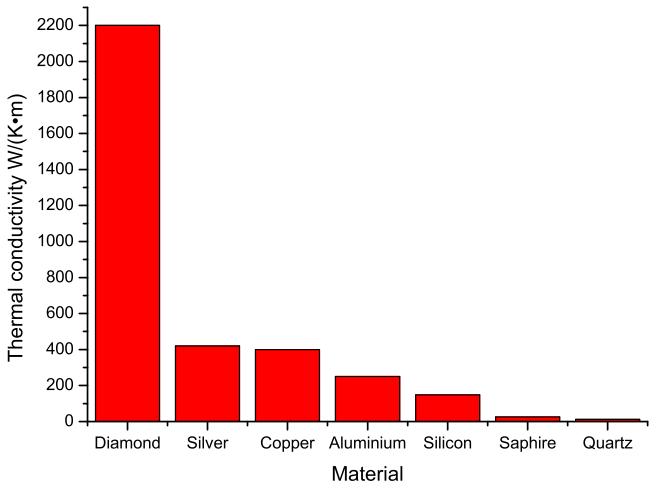

Figure 4.6: Thermal conductivity of diamond in comparison.

The complete sp^3-hybridization does not only result in an extreme hardness, but also in a very high thermal conductivity of diamond. Amounting to $2200\,\mathrm{W\,m^{-1}\,K^{-1}}$ [2,54], the thermal conductivity of diamond exceeds the one of copper or silver by about a factor of five (see Fig. 4.6). Isotopical enrichment (the substitution of C_{13} by C_{12}) can increase the thermal conductivity even further by orders of magnitude [65]. The fact that diamond is such an excellent heat conductor makes it a material of choice whenever large amounts of heat have to be fed to or drained from a device. For example, diamond is often used as a heat sink for high-power laser diodes [2].

Chemical properties

Because of the high binding energy of the sp^3-hybridized C—C bond, diamond is chemically inert at room temperature, withstanding chemical etching of even the most aggressive acids. Its inert nature makes diamond a very biocompatible material since

the interaction with surrounding organic tissue is minimized. Compared to stainless steel and titanium, the materials most implants are made of, diamond features less cellular adhesion, a higher resistance to corrosion and better mechanical stability[66]. At elevated temperatures, however, diamond does react with certain chemicals. Most prominent is the reaction of diamond carbon with oxygen to carbon dioxide. In an pure oxygen environment, temperatures of $T > 1000\,\mathrm{K}$[67] are necessary to activate the combustion reaction. Under UHV conditions, where no significant amount of oxygen is present, the diamond is stable up to $T = 2000\,\mathrm{K}$[67]. At temperatures higher than 2000 K, the carbon undergoes a phase transition from the diamond to the graphite modification. In addition, diamond does react with some metals to form carbides and with molten salts like potassium nitrate, but only at elevated temperatures[68].

Some of the key parameters of intrinsic diamond are listed in Tab. 4.1.

Property	Value
Mass density	$3.52\,\mathrm{g/cm^3}$ [54]
Atomic density	$1.76 \times 10^{23}\,\mathrm{cm^{-3}}$ [54]
Mohs hardness	10 [54]
Young's modulus	1200 GPa [69]
Band gap	5.5 eV [59]
Thermal conductivity	$2200\,\mathrm{W\,m^{-1}\,K^{-1}}$ [54]
Specific heat (300 K)	$0.51\,\mathrm{J\,g^{-1}\,K^{-1}}$ [70]
Debye temperature	2230 K [71]
Poisson's ratio	0.08 [69]
Refractive Index	2.3 – 2.4 [64]
Dispersion coefficient	0.044 [64]
Dielectric constant	5.7 [2]

Table 4.1: Properties of diamond.

Diamond synthesis

The vast majority of diamonds used in industrial and scientific applications today are not mined from natural sources but are synthesized instead. This includes all samples used in this work. In order to synthesize diamonds of lateral dimensions on the scale of a few millimeters, there are two well-controlled methods: high-pressure-high-temperature (HPHT) synthesis and growth by chemical vapor deposition (CVD).

HPHT technique

In the HPHT method, graphite is compressed with a pressure of several gigapascal at temperatures above 1000 K. Since diamond is the more stable polymorph under those conditions, the carbon transforms from graphite to diamond. With the HPHT method, high-quality diamonds can be produced at relatively low cost, making it interesting for the large-scale production of industrial diamonds. In the production process, however, impurities are implanted from the surrounding environment, most notably nitrogen. For this reason, HPHT diamonds are always nitrogen doped to some degree, which is why they usually have a characteristic yellow color. Since the focus of this thesis is on the study of intrinsic high-purity diamonds, HPHT diamonds could not be used.

CVD technique

CVD diamonds, on the other hand, are grown in a reactor from a mixture of hydrocarbon gases, usually containing methane to provide the carbon and hydrogen to remove non-diamond carbon from the growing surface. In case of single crystal diamonds with well-defined main surface planes (e.g. (100) or (111)), a small single crystal of the desired orientation is used as a substrate. By adjusting deposition parameters like gas flow, gas constituents, pressure and substrate temperature, a well-controlled and even growth of diamond on the substrate is achieved without unin-

tended doping. This allows for the production of diamonds with impurity concentrations below 1 ppm, as used in this thesis.

Classification

There are several ways to classify diamond. The most well-known approach is probably the evaluation based on weight (in carat), clarity, color and cut (**CCCC** criteria) of the diamond. Those CCCC criteria, however, are used almost exclusively in the gemstone industry. For scientific purposes, these four diamond characteristics are often of little or no importance at all. Hence, a different classification is prevalent in the scientific community, sorting the diamonds into four categories called Type Ia, Ib, IIa and IIb. This classification is based on the level of impurities incorporated in the diamond[54] and is explained in detail in the following.

Type Ia

In type Ia diamond, nitrogen is the main impurity and amounts for up to 0.3 % of the diamond mass. The nitrogen aggregates in small groups of two, three or four atoms and thereby forms specific nitrogen centers within the diamond. Those centers exhibit a different adsorption spectrum than diamond. As a result, the nitrogen impurities can cause the diamond to appear colored, if their proportion is big enough. The vast majority of natural diamond is of type Ia.

Type Ib

In type Ib, nitrogen is the main impurity as well, but amounts only for up to 0.05 % of the diamond mass. In contrast to type Ia, the nitrogen atoms are located in isolated sites spread throughout the diamond and do not cluster. Because of those single impurities, type Ib diamonds usually have a characteristic yellow-brown color. While type Ib diamond does not make up for a

significant proportion of natural diamonds, almost all diamonds synthesized by the HPHT method are of this type.

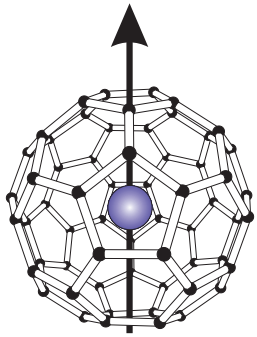

Figure 4.7: Model of a paramagnetic endohedral fullerene. A single nitrogen atom (blue) is encapsulated in a C_{60} molecule. The arrow visualizes the electron spin provided to the molecule by the nitrogen atom.

Type IIa

Type IIa diamond is high-purity diamond, meaning that the impurity concentration is below the detection limit of standard IR- or UV-spectroscopy methods (usually <1 ppm).
While those diamonds are rare in nature, they can nowadays be synthesized with high efficiency using the CVD method. Due to the absence of impurities, type IIa diamonds are insulating and colorless, making them the diamonds of choice for window applications or when intrinsic diamond is required as in this thesis.

Type IIb

As mentioned before, diamond can become a p-type semiconductor upon boron doping. Since there is a huge scientific interest in this kind of diamond, a separation from the nitrogen-doped diamond types is necessary, which is ensured by the introduction of the category IIb. Type IIb diamonds are similar to type IIa diamonds in the sense that type IIb as well implies the diamond to have no measurable concentration of nitrogen incorporated. However, type IIb diamonds do contain significant amounts of boron impurities. This type of diamond is scarcely found in nature, but can be synthesized by implementing well-controlled proportions of boron during the CVD growth process.

Diamond in quantum computing

As already mentioned, nitrogen vacancies in diamond can be exploited in order to construct a quantum computing device. A variety of different approaches to implement such a device have been studied so far, see for example[3–8,72–76]. In this thesis, however, the focus is on a design in which the NV-centers are not

addressed directly, but with the help of functionalized molecules adsorbed on top of the diamond surface [77–79].

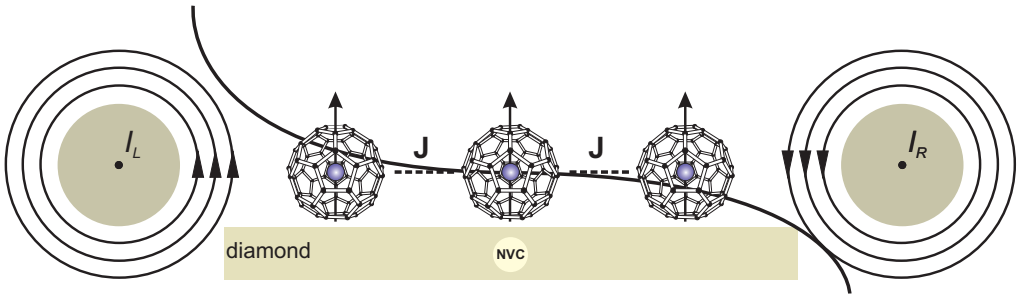

Figure 4.8: Model of the quantum computer setup, showing a string of three PEFs on a diamond surface in vicinity of a NV center and in between two wires that are aligned perpendicular to the string. *J* indicates the possibility of dipole-dipole coupling of the PEFs, the solid black curve visualizes the magnetic field gradient generated by the two wires.

In this particular approach, paramagnetic endohedral fullerenes (PEFs) work as the qubits of the quantum register. A PEF consists of a nitrogen atom sheltered inside a C_{60} molecule (see Fig. 4.7). The nitrogen atom provides an electron spin of 3/2. As used by default for example in electron spin resonance (ESR) experiments, electron spins can be manipulated externally. Therefore, the spin state of a PEF can in principle be used to store one bit of information. In addition, spin-spin coupling of nearby PEFs results in quantum entanglement, thus allowing for the PEFs to be used as qubits. The C_{60} shielding does not only ensure long spin lifetimes and sharp resonance frequencies, but in principle also allows for a stable positioning of the nitrogen atoms on elected positions on the diamond surface. This could be done, for example, by means of molecular self-assembly or by direct manipulation using an AFM tip.

As can be seen in Fig. 4.8, the quantum computer setup consists of an array of PEFs positioned on the diamond surface atop shallow NV-centers. The qubits are prepared by means of optical pumping with 532 nm laser light, exciting the NV-center from m_s=0 and m_s=1 ground states to the corresponding excited states via the vibronic band. In the case of m_s=0, the system directly returns to the ground state by emission of fluorescent red light of λ =645 nm [80].

From the m_s=1 state, however, a transition to a dark state with long lifetime (several microseconds) takes place instead of direct relaxation to the m_s=1 ground state. Hence, the irradiating

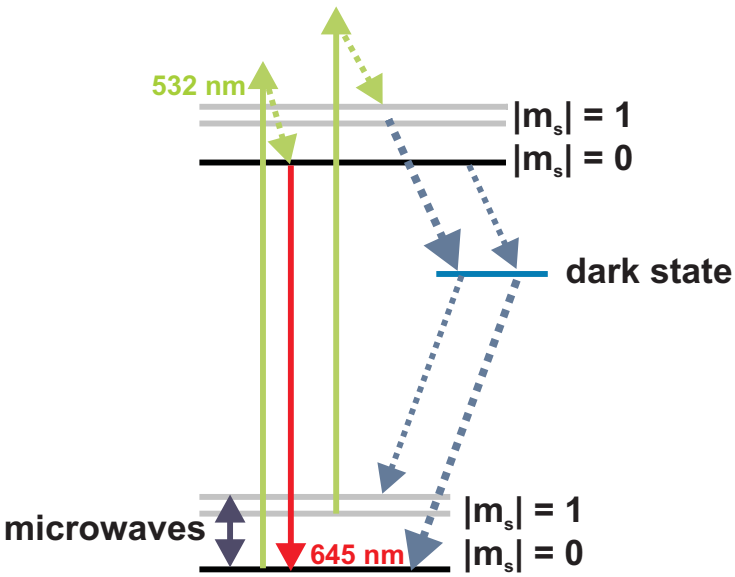

Figure 4.9: Level scheme of the NV-center showing the transitions following optical excitation by green light of $\lambda = 535nm$

light tunes the NV-center to the m_s=0 state, which is made use of as a as well-defined starting configuration (see Fig. 4.9). In addition, pulsed ESR microwaves of adequate frequency induce a transition from the initial m_s=0 state to the m_s=1 state. As explained above, the m_s=1 state relaxes via a dark state, unlike the m_s=0 state, which causes the emission of red light upon relaxation. Hence the microwave excitation is visible in the fluorescence spectrum of the NV-center as local minima at the transition frequency. This is utilized by using pulsed optically detected magnetic resonance (ODMR) as read-out technique. In the ODMR spectrum, the intensity of the fluorescence is measured as a function of the frequency of the microwaves used to address the qubits. Hence a characteristic pattern can be found in the ODMR spectrum as a consequence of addressing a single qubit by a single ESR pulse or a complete pulse sequence (see Fig. 4.10). It should therefore be possible to simultaneously manipulate and read-out the state of single qubits by using NV centers.

By positioning PEFs atop NV centers, spin coupling between the caged nitrogen atoms and the centers is enabled. Hence, the

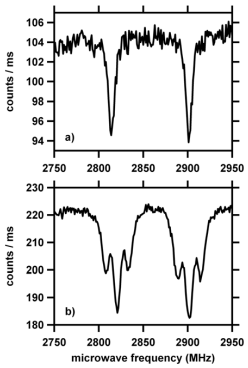

Figure 4.10: ODMR spectra of light emitted by a NV-center. a) no electron spin-coupling, b) electron spin coupling.[80]

NV-centers do not have to be addressed directly, but instead can be manipulated using the spin states of the PEFs. This shall be done experimentally by positioning two nanoscale wires at opposing ends of the PEF array. By applying a small current through the wires, a magnetic field gradient B_z is extended over the molecules, slightly changing the electron spin resonance frequency of each qubit to a specific value. By irradiation of ESR microwaves of suitable frequency, each of the qubits can be addressed individually. Pulsed ESR is used as well for the computing step by regulating the dipolar spin-spin coupling of neighboring molecules.

This setup thus combines direct optical accessibility of the NV-centers with the advantage of having localized, positionable and long living electron spins in PEFs that entangle by spin-spin coupling.

4.2 Diamond C(100) surfaces

The diamond surface in focus of this thesis is the C(100)-(2 × 1) surface. Two modifications of the surface have been studied, the bare surface as well as the hydrogen-terminated surface. Both types are described in the following.

The bare C(100)-(2 × 1) surface

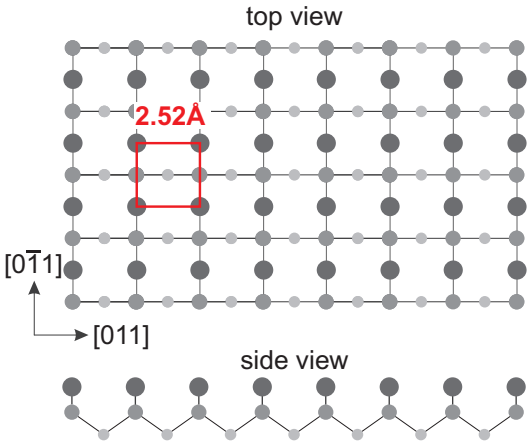

Figure 4.11: Model of the unreconstructed diamond C(100) structure. The red box represents a surface unit cell.

As can be seen in Fig. 4.2, a (virtual) bulk truncation across the (100) plane removes two of the four binding partners of each surface carbon atom, leaving it with two unsaturated dangling bonds.
The resulting C(100) surface, which is identical with the C(010) and the C(001) surface, is depicted in Fig. 4.11. It features a square unit cell with a side length of 2.52 Å in both surface directions ([0$\bar{1}$1] and [011])[81]. This unreconstructed surface is very unstable due to the high reactivity of the dangling bonds, leading to a high surface energy of E_s =3.89 eV/atom[82].
Upon formation of the C(100) surface, the dangling bonds are therefore immediately saturated with foreign atoms from the environment or, when prepared in UHV, with neighboring carbon atoms. The latter results in a double bond between two carbon atoms by the overlap of sp^2 hybridized orbitals. This means

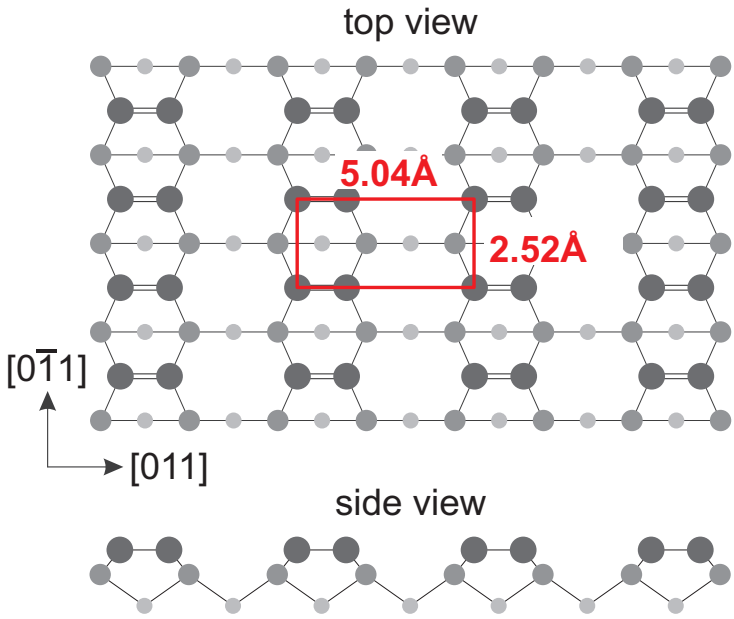

Figure 4.12: Model of the reconstructed diamond C(100)-(2 × 1) structure. The red box represents a surface unit cell.

a dimerization of the topmost carbon atoms, ending in a completely (2 × 1) reconstructed surface as shown in Fig. 4.12.

The carbon dimers are aligned in rows alongside the [0$\bar{1}$1] direction, the C═C distance within one dimer being 1.37 Å[81]. The dimer-dimer distance within a dimer row is 2.52 Å, the rows itself are separated by exactly twice that distance (5.04 Å) in [011] direction[83]. Together, those distances define the unit cell of the surface. Due to the crystal structure of diamond, surface directions are rotated by 90° between successive layers. This is apparent in the three dimensional unit cell, as depicted in Fig. 4.2. Here, each side of the cell features a C(100) surface, but the surface directions are rotated by 90° between opposing sides.

Although energetically a lot more stable (surface energy: E_s =2.12 eV/atom[82]) than the unreconstructed type, the unsaturated nature of the dimer π-bonds makes for a very reactive surface because the formation of two single bonds is energetically favored over the existing double bond. Hence, adsorbates easily chemisorb to the C(100)-(2 × 1) surface upon exposure to air, re-

sulting in a rich and largely undefined surface chemistry. Especially molecules that posses large conjugated π-systems readily bind to the surface. A UHV environment is therefore essential for the study of the bare diamond C(100)-(2 × 1) surface.

Because of the huge economic interest in diamond, a lot of research on diamond and its surfaces has been done in the past. Especially the development of the CVD technique, which can be considered a breakthrough with respect to the synthesis of well-defined diamond surfaces, allowed for the study of aforementioned surfaces in great detail.
In case of the bare C(100) surface, a (2 × 1) reconstruction was suspected before experimental observance because of the structural similarity of diamond to silicon and germanium, on which such a reconstruction was already discovered. In 1977 then, the (2 × 1) reconstruction of the C(100) surface was first observed experimentally by Lurie and Wilson, using low-energy electron diffraction (LEED)[84]. In the aftermath, the structural and electronic properties of the surface were explored step-by-step, making use of a wide range of spectroscopy techniques as well as theoretical calculations[29,85].

The invention of the scanning tunneling microscope (STM) in 1981 even allowed for real-space imaging of the bare surface, albeit only when the diamond is heavily boron-doped and thereby semiconducting. The first high-resolution images of the bare C(100)-(2 × 1) surface of such a boron-doped crystal was published in 1996 by Nutzenadel *et al.*[86] (see Fig. 4.13). Later, Bobrov *et al.* were even able to obtain images revealing individual dimer rows of an undoped and therefore insulating diamond[87]. However, that paper remains the only STM study on the C(100)-(2 × 1) surface of insulating diamond up to now. Despite the high resolution, no single dimers are visible in the STM images. Thus, no true atomic resolution was achieved.

The hydrogenated C(100)-(2 × 1):H surface

When hydrogen is present during the growth of the diamond C(100) surface, which is always the case in the CVD process,

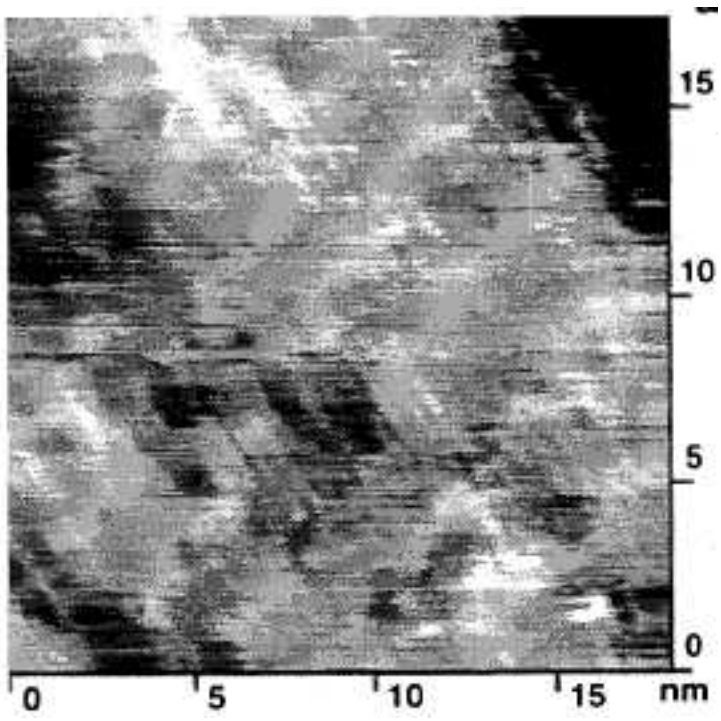

Figure 4.13: First high-resolution STM image of the C(100)-(2 × 1) surface[86].

the emerging surface is immediately saturated with atomic hydrogen. This also holds true for a subsequent exposure of the C(100)-(2 × 1) surface to hydrogen plasma. In the most stable configuration, one hydrogen atom is attached to each of the topmost carbon atoms, thereby reducing the C═C double bond of a dimer to a single bond (see Fig. 4.14). Because of the lesser strength of the single bond, the distance between the two carbon atoms increases to 1.63 Å upon hydrogenation.

Another conceivable surface configuration derives from the attachment of two hydrogen atoms to one carbon atom, completely annihilating the dimeric structure. As a consequence, the surface is (1 × 1):2H reconstructed in this case, as was observed before for example on silicon. Due to the stronger electronegativity of carbon compared to silicon, though, the hydrogen is carrying a comparatively larger partial charge. This leads to a strong repulsion between two adjacent hydrogen atoms, making

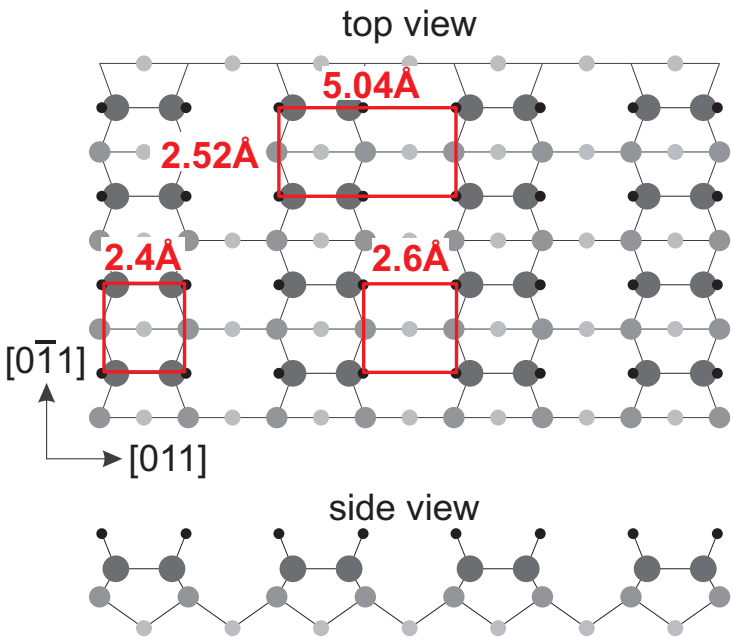

Figure 4.14: Model of the diamond C(100)-(2 × 1):H structure. Hydrogen atoms are depicted black, carbon atoms in different shades of gray according to their position (the darker the closer to the surface).

a (1 × 1):2H configuration unfavorable compared to the (2 × 1):H structure[29].

The electrostatic repulsion of the partially positively charged hydrogen atoms, however, has an influence on the (2 × 1):H reconstruction as well. It leads to a tilting of the C—H binding, resulting in an angle of 113.3° with respect to the dimer bond. Hence the distance of two hydrogen atoms (2.4 Å) of one dimer is significantly larger than those of the corresponding carbon atoms[88]. As depicted in Fig. 4.14, this also means that the distance between two hydrogen atoms of adjacent dimer rows is almost the same than the aforementioned distance between two hydrogen atoms of the same dimer (2.6 Å compared to 2.4 Å). The surface thus features an almost square hydrogen arrangement. The unit cell nonetheless has the same dimensions as the unit cell of the bare diamond C(100)-(2 × 1) surface (5.04 Å × 2.52 Å).

Compared to the bare diamond surface, the hydrogen-terminated surface is chemically much less reactive. A hydrogenation of the

surface can therefore be used to chemically passivate the surface and prevent the unwanted adsorption of molecules from the environment. Hence the C(100)-(2 × 1):H surface can be exposed to ambient conditions for several month without major signs of degradation, as will be shown in Chap. 7.

In addition to its chemical stability, the C(100)-(2 × 1):H surface offers another interesting characteristic: a negative electron affinity (NEA). The electron affinity χ is defined as the *"'energy required to detach an electron from the singly charged negative ion"'*[17]. An equivalent definition is: *"'(electron affinity is) the energy released when an additional electron is attached to a neutral atom or molecule"'*[17]. Using the band model, one can as well define the electron affinity as the energy difference between the vacuum level E_{Vac} and the conduction band minimum E_{CBM}:

$$\chi = E_{Vac} - E_{CBM} \tag{4.1}$$

A surface with a *negative* electron affinity therefore readily donates electrons to adsorbates with a strongly positive electron affinity.

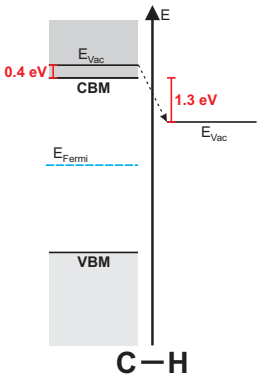

Figure 4.15: Effect of hydrogen chemisorption on the vacuum energy level and the electron affinity of diamond.

In case of the diamond C(100)-(2×1):H surface, the NEA is caused by the higher electron affinity of carbon compared to hydrogen. This results in a charge separation with the positive partial charge located at the hydrogen atom and the partially negative counterpart located at the carbon atom. This polarization of the surface leads to a lowering of the vacuum level to below the CBM (see Fig. 4.15). The resulting NEA amounts to $\chi_H = -1.3 \pm 0.1\,\mathrm{eV}$[89,90]. If on the contrary the hydrogen is substituted by a atomic species with a higher electron affinity than carbon, for example oxygen, E_{Vac} is increased by the surface polarization with the result that the electron affinity becomes highly positive ($\chi_O = +1.7 \pm 0.1\,\mathrm{eV}$[90]). The electron affinity of bare diamond is slightly positive as well, amounting to ($\chi_C = +0.4 \pm 0.1\,\mathrm{eV}$[89]), as can also be taken from Fig. 4.15.

Because of the NEA, even intrinsic diamond can exhibit a surface conductivity when the surface is hydrogen-terminated and covered with electron-attracting molecules. These kinds of adsorbates can, for example, be found dissolved in a wetting layer, explaining the emergence of surface hole conductivity upon exposure to air, as was first observed by Ravi and Landstrass[91].

The underlying mechanism was finally revealed by Maier *et al* in 2001 and is known as the **diamond transfer doping** model[92].

In this model, the p-type behavior of the C(100)-(2 × 1):H surface is explained by electron transfer from the surface into a strongly electron-affine molecular layer adsorbed on the surface, for example in form of an ambient wetting layer. The existence of a wetting layer, however, is not a prerequisite for transfer doping. What is needed is simply a molecular species with very high electron affinity, for example C_{60} fullerenes (see Chap. 3).

Whatever the nature of the electron acceptor, the transferred electron leaves behind a subsurface hole-layer causing a surface conductivity in the order of 10^{-6} S to 10^{-5} S at room temperature[44]. The semiconductive behavior of the hydrogen-terminated surface allows for STM imaging, which has therefore been the method of choice in a number of studies focusing on the electronic structure of the C(100)-(2 × 1):H surface[28,86,93–95]. Consequently, the first high-resolution real-space image of this surface has been obtained using STM. It was published in 1994 by Tsuno *et al.*[96] (Fig. 4.16).

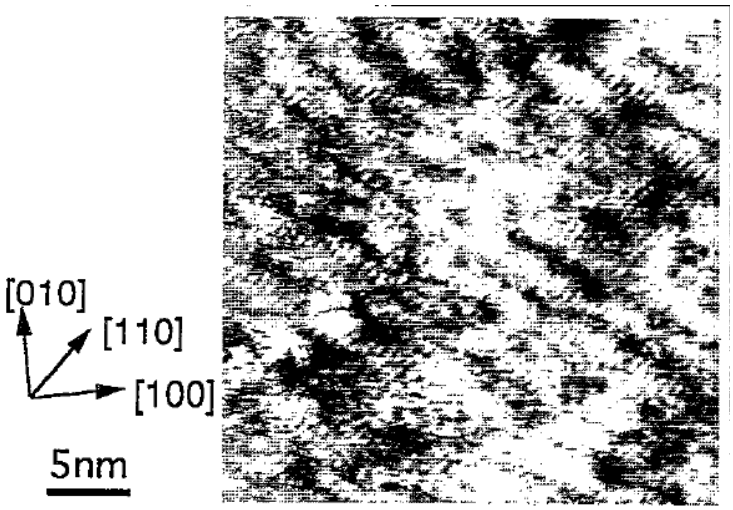

Figure 4.16: First high-resolution STM image of the C(100)-(2 × 1):H surface[96].

5 Molecule deposition chamber

Contents

In order to enable the study of different molecular deposition techniques, a suitable UHV chamber was needed and had to be designed. General setup and components of this chamber are presented in this chapter. This includes the chamber corpus, the pumping system and various measuring instruments. In the following, the chamber will be referred to as "MBE chamber", which is short for "**M**olecular **B**eam **E**pitaxy Chamber".

5.1 Requirement profile

In order to study the interaction and assembly of molecules on substrates with NC-AFM, the ability to deposit said molecules in a well-controlled manner with sub-monolayer precision is a prerequisite. Therefore, the sublimation temperature under UHV conditions of the chemical to be studied has to be determined first. To do so is one of the primary objectives for which the MBE chamber is designed. For the sublimation temperature determined in the MBE chamber to be comparable with the sublimation temperature in the VT-AFM chamber, the distance of the sublimator orifice and the target as well as the background pressure have to be roughly the same in both UHV systems. The pumping system of the MBE chamber therefore has to be able to maintain a vacuum in the order of 10^{-10} mbar.

Chemicals that decompose before the sublimation temperature under UHV conditions is reached can of course not be deposited by sublimation. Here, a different deposition method is needed. The most straightforward approach is deposition from solution using a solenoid pulse valve. To provide a facility to implement and calibrate such a pulse injection device was also part of the specification profile of the MBE chamber.

Furthermore, the MBE chamber should provide the possibility to operate an STM and to study temperature programmed desorption (TPD). The chamber must therefore be able to host a scanning probe microscope, a highly sensitive mass spectrometer and a probe manipulator. In addition, the chamber must offer flanges that are appropriate for instruments that are necessary for sample preparation, such as a crystal cleaver or a sputter gun. Also, the possibility to mount a load-lock must be provided.

5.2 MBE chamber corpus

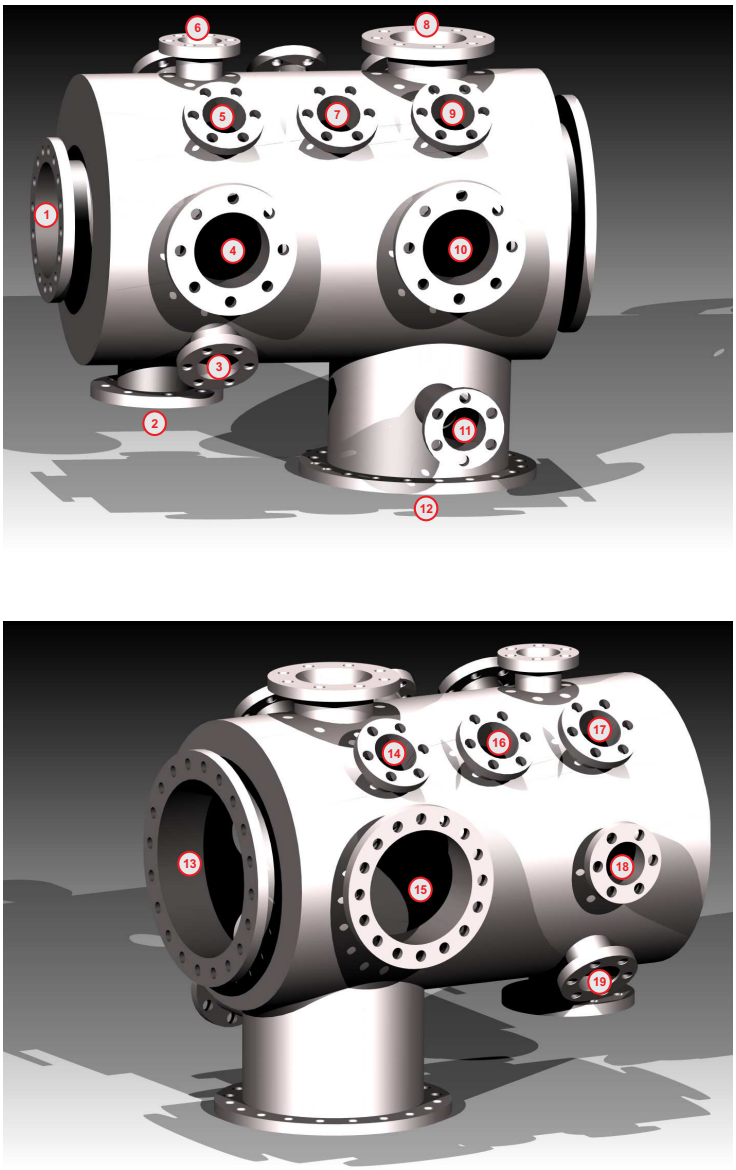

Figure 5.1: Rendered image of the MBE chamber corpus showing the position of every flange. The flanges are numbered in accordance with Tab. 5.1.

The main body of the MBE chamber has a cylindrical shape (see

Fig. 5.1 and Fig. 5.2). This offers the benefit that components flanged to the cylinder barrel surface always face towards the cylinder axis. The main body is made of austenitic stainless steal (type 304) and has dimensions of 40.0 cm in length along the cylinder axis (50.0 cm including flanges) and 25.4 cm in diameter (36.0 cm including flanges). It was build by Vacom (Jena, Germany) according to a technical drawing provided by us.

To facilitate a broad application spectrum, a maximum number of ConFlat™ (CF) flanges (19 overall) was attached to the main body. Of these 19 CF-flanges, 11 are of size DN40, 4 of size DN63, 2 of size DN100 and 2 of size DN150. The purpose of the flanges will be explained in the following. For the sake of explanation, the flanges are numbered according to Fig. 5.1.

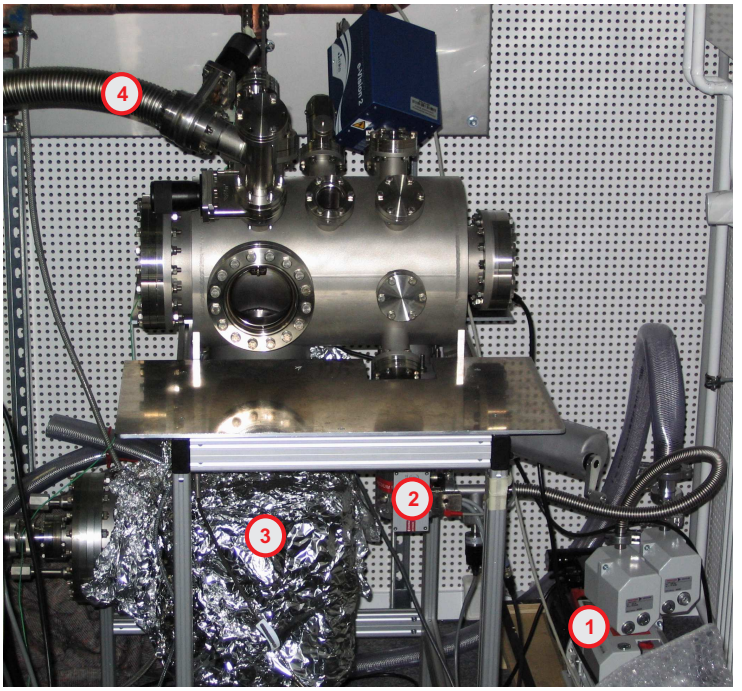

Figure 5.2: Photo of the running MBE chamber including the pumping system. (1) rotary vane pump, (2) turbomolecular pump, (3) ion getter pump, (4) connection to additional pumping station for sublimator evacuation.

The cylindrical main corpus is terminated by a DN100 flange at one end (flange 1) and by a DN150 flange (flange 13) at the other end. These flanges provide the option to mount a probe manipulator (flange 1) and an STM (flange 13) to the chamber.

The second DN150 flange (flange 12) is connecting an ion getter pump (IGP) to the main chamber and so defines the bottom side. This flange is extended by 11.0 cm in order to allow for a pressure gauge to be mounted to the chamber (flange 11) without consuming space in the main chamber. The only other bottom flange (flange 2) is arranged in line with the IGP flange and is used to connect a turbomolecular pump to the chamber. This flange is connected to the chamber via a gate valve. Flanges 3 - 6 and 17 - 19 are arranged in one radial plane on the barrel surface, the angle between adjacent flanges is 45°. Due to the in-plane alignment, all flanges point to the same spot on the cylinder axis, which allows for a straightforward use of this flanges in deposition experiments. The size of those flanges is DN40 and DN63, respectively. Flanges 8 - 10, 14 and 15 form a second ring of flanges (DN40, DN63 and DN100) perpendicular to the cylinder axis, thereby creating a second plane of operation. In between the two rings, two more flanges (flanges 10 and 11) are attached, again pointing towards the cylinder axis. An overview of the flanges and their designated purpose is given in Tab. 5.1.

Number in Fig. 5.1	Size	Purpose	Remarks
1	DN100	-	For manipulator
2	DN63	Turbopump	-
3	DN40	-	-
4	DN63	Window	-
5	DN40	QMS	-
6	DN40	Window	-
7	DN40	Leak valve	-
8	DN40	Pulse valve	-
9	DN40	QCM	-
10	DN40	-	-
11	DN40	Pressure gauge	-
12	DN150	IGP	-
13	DN63	-	For STM
14	DN40	Sublimator	-
15	DN63	Window	-
16	DN40	-	For TPD
17	DN100	Window	-
18	DN150	-	-
19	DN40	-	-

Table 5.1: Overview of the flanges of the MBE chamber. The numbers refer to Fig. 5.1, the underlying color labels flanges that are aligned in the same plane.

5.3 Instruments

Pressure measurement

In order to control the chamber background pressure, a pressure gauge that is operating down to the 10^{-11} mbar regime is needed. Since cold-cathode Penning gauges are suitable only down to about 10^{-8} mbar, either an Inverted Magnetron gauge (also known as Redhead gauge) or a Bayard-Alpert manometer has to be used. The Inverted Magnetron gauge is less vulnerable to a corrosive environment than a Bayard-Alpert manometer and can also be operated at a higher background pressure (up to approx. 10^{-2} mbar). As a drawback, though, it is in general less sensitive. The Bayard-Alpert manometer offers the highest sensitivity of all UHV pressure gauges, but has the disadvantage of operating with a fragile hot filament. Since a good comparability of results obtained with the MBE chamber to the VT-AFM UHV system is of the highest priority, an accurate pressure measurement is most important. The ability to operate with corrosive gases, on the other hand, is usually not relevant to the designated purpose of the chamber. Therefore, a Bayard-Alpert manometer of type UHV-24p (Agilent Technologies, Santa Clara, California), operated with tungsten filaments, was chosen as UHV pressure gauge. To control the foreline pressure, a convection gauge of type ConvecTorr (Agilent Technologies, Santa Clara, California) is used. Both pressure gauges are simultaneously operated by a controller of type XGS-600 (Agilent Technologies, Santa Clara, California).

For residual gas analysis, a quadrupole mass spectrometer (QMS) of type e-Vision 2 (MKS Instruments Deutschland GmbH, Munich, Germany) is used. This QMS was chosen to allow for a direct comparison with the NC-AFM UHV system, where the same instrument is used.

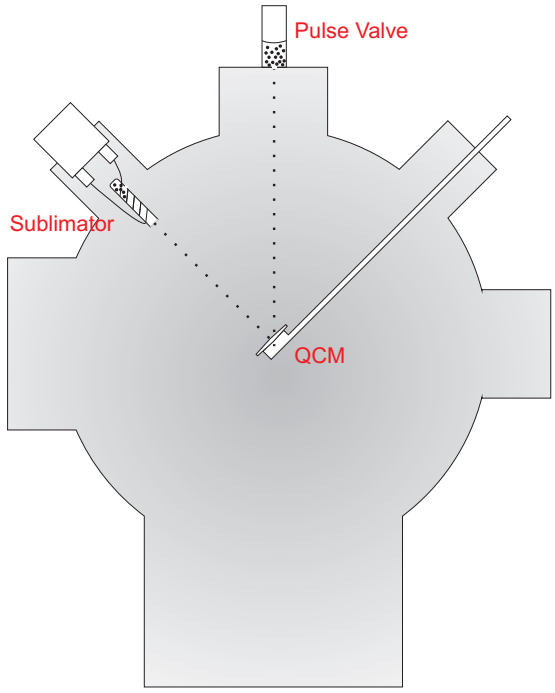

Figure 5.3: Cross section model of the MBE chamber showing the position of the QCM sensor crystal in relation to sublimator cell and pulse valve.

Molecule deposition

A quartz crystal microbalance (QCM) is used to measure molecular deposition. Here, a gold-coated 6 MHz quartz crystal (Inficon, Bad Ragaz, Switzerland) is mounted to a sensor (Frontload Bakeable Sensor, Inficon, Bad Ragaz, Switzerland), which is flanged to the main chamber (flange 14) so that the crystal is positioned directly in the center of the chamber (see Fig. 5.3). The active crystal plate is therefore located precisely in the course of the molecule beam of the sublimator at flange 14. In this setup, the QCM can also be used to control the deposition of molecules by pulse injection. In this case, however, the crystal plate is tilted by 45° with respect to the injection direction. This reduces the active crystal area by a factor of $\sqrt{2}$, which of course has to be taken into account when determining the deposited thickness. The thickness of the adlayer is recorded by a IC6 thin film deposition controller (Inficon, Bad Ragaz, Switzerland), which allows

for a resolution down to 0.1 Å.

Pumping units

Figure 5.4: Internal layout of the Agilent VacIon 300 Plus IGP. The red arrow points out the star-shaped slats of the Starcell Cathode[97].

A cascade connection of a rotary vane pump, a turbomolecular pump and a combination pump containing an ion getter pump (IGP) as well as a titanium sublimation pump (TSP) is used in order to evacuate the chamber to ultra-high vacuum.

The overall volume of the chamber amounts to approximately 57 l. This limited volume allows for the use of a rather small-sized turbomolecular pump. The pump that was selected for this purpose is a HiPace80 (Pfeiffer Vacuum, Asslar, Germany) mounted to a CF DN63 flange. This pump has a pumping speed in the region of $50\,l\,s^{-1}$ to $80\,l\,s^{-1}$ under UHV conditions. The gas throughput is therefore sufficient to maintain the UHV even during the sublimation of molecules. When depositing molecules from the liquid phase using a pulse valve, the chamber pressure

inevitably rises beyond UHV upon opening of the valve, but is decreased to the UHV regime by the turbo pump in the course of a few seconds (see Sec. 5.4).

The foreline pressure of 10^{-4} mbar to 10^{-3} mbar is maintained by a rotary vane pump of type DUO 5 M (Pfeiffer Vacuum, Asslar, Germany), which has a pumping speed of $8\,\mathrm{l\,s^{-1}}$.

In order to reach a background pressure below 10^{-9} mbar, rotary vane and turbomolecular pump alone are not sufficient but have to be supported by an IGP. To maintain a vacuum that is comparable to the background pressure in the VT-AFM chamber, a high-capacity IGP of type VacIon Plus 300 (Agilent Technologies, Santa Clara, California) was used. The pumping speed naturally depends on the getter material chosen, its grade of saturation and the composition of the residual gas, but in general amounts to $100\,\mathrm{l\,s^{-1}}$ to $300\,\mathrm{l\,s^{-1}}$. Regarding the internal setup of the pump, the Starcell™ version was chosen. This IGP version features a triode configuration, meaning that the anode blocks are sandwiched between two cathode plates made of different getter materials. Here, one cathode is made of tantalum, the other of titanium. The cathode plates feature star-shaped slats (Fig. 5.4), which enable the IGP to pump high amount of noble gases as well as common residual gases. While the ability to handle a high partial pressure of noble gases is not necessary in the molecule deposition experiments, it provides the possibility of sample preparation by noble gas sputtering, which is important with regard to an expanded use of the chamber for STM.

Inside the IGP, a TSP is mounted (Agilent Technologies, Santa Clara, California). It consist of three titanium filaments through which a current can be passed in order to heat the titanium beyond its sublimation temperature. The sublimated titanium then coats the surrounding area and works as a getter material due to its high sticking coefficient. The getter efficiency can be drastically increased by active cooling of the deposition area with water or liquid gases. For this purpose, the TSP is equipped with a cooling shield.

By time the titanium coating becomes saturated with particles from the residual gas and the getter yield decreases, requiring

a fresh layer of titanium to be sublimated. Hence, a TSP is, unlike the other pumps of this system, not used continuously, but only occasionally in order to temporarily improve the background pressure. Typical operation parameters are a TSP filament current of 48 A and a sublimation time of 60 s.

5.4 Practical application

Since implementation, the MBE chamber described above is used by default to determine sublimation temperature and enthalpy under UHV conditions of molecules that are to be studied with NC-AFM. This is done by using the combination of a molecule sublimator and QCM as depicted in Fig. 5.3. In addition, the QMS enables residual gas analysis during sublimation, which offers the possibility to check for impurities or decomposition products in the chemical to be sublimated. This allows for a well-defined deposition of target molecules on a substrate in coverages of less than one monolayer, as required to study the adsorption behavior of single molecules on the atomic scale. With regard to this thesis, for example, the sublimation parameters of C_{60} and $C_{60}F_{48}$ have been determined using the MBE chamber.

As a drawback, however, the deposition by sublimation has the profound disadvantage that it can only be applied to chemicals that are thermally stable and therefore do not decompose before the sublimation temperature under UHV conditions is reached. This excludes a large variety of molecular species, including proteins, polymers and the paramagnetic endohedral fullerenes introduced in Chap. 4. Since the main aspect of this thesis is to lay the groundwork for the realization of a quantum computer concept of which PEFS are an integral part (refer to Chap. 4 for details), the deposition from solution using a pulse valve as an alternative for the deposition of such molecules was implemented in the MBE chamber.

The basic pulse injection setup can be seen in Fig. 5.3. The solenoid pulse valve used (Parker Series 9, Parker-Hannifin, Cleveland, Ohio) has an orifice of 50 µm and is operated with a IOTA ONE valve driver (Parker-Hannifin, Cleveland, Ohio). The deposition is controlled by QCM and QMS.

Pulse injection calibration

Technique

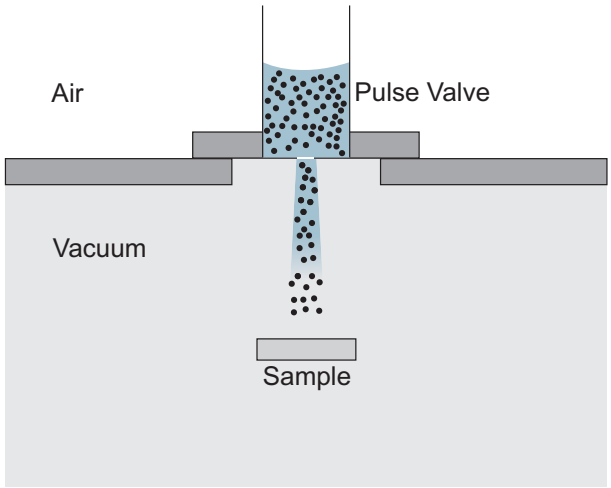

Figure 5.5: Schematic view of the pulse valve setup.

In the pulse injection setup, a small, non-vacuum bin containing a concentrated solution of the molecules to be deposited is connected to the deposition chamber via a high-performance solenoid pulse valve. The very small orifice (usually 50 µm to 100 µm) of the pulse valve is facing the substrate surface (see Fig. 5.5) and is opened for a short period of time (usually some milliseconds). As a result, a small amount of the solution is released into the UHV chamber towards the surface. This usually results in a deposition of both, target molecules and solvent, on the surface. In order to remove the solvent, the surface may subsequently be annealed at a temperature sufficient to remove the solvent without desorbing or decomposing the target molecules. This obviously requires a well-chosen combination of target molecules, substrate and solvent. Not only does the solvent need to possess a high solubility for the target molecule, a weak interaction with the sample is also required. To combine all this is often problematic and hampers the applicability of the pulse injection technique significantly. In addition, the deposition process itself is not as straightforward as described above, because the sudden

drop in pressure when the valve is opened can cause the solvent to freeze up the orifice in an instant.

Experiments

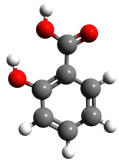

Figure 5.6: Model of a salicylic acid molecule.

In order to study in detail whether a reproducible amount of solved molecules can be deposited on a substrate by pulse injection in the current setup, a measurement series focusing on the deposition of salicylic acid from solution was performed in the MBE chamber. Here, salicylic acid was solved to saturation in three different solvents, namely ethanol, ethyl acetate and acetonitrile and injected into the MBE chamber described in Chap. 5. Instead of a substrate, a QCM sensor was chosen as the deposition target in this experiment, allowing for a direct quantification of the deposition layer thickness in the sub-angstrom regime. Simultaneously, the constitution of the residual gas in the chamber was observed with a quadrupole mass spectrometer (QMS) in order to check for salicylic acid.

Salicylic acid has a very high solubility in the solvents mentioned above. This of course leads to a high ratio of salicylic acid to solvent molecules and therefore to an enhanced amount of target molecules injected with each pulse. Also, the relatively small molar mass of salicylic acid ($M = 138.12\,\mathrm{g\,mol^{-1}}$) allows for the detection of single-ionized molecules with the QMS. Hence, a potential peak at 138 u in the mass spectrum after opening the pulse valve is direct evidence of the injection of intact salicylic acid molecules.

Salicylic acid was soluted to saturation in ethanol (325 g/l) and injected into the MBE chamber using the same pulse valve as described before (50 µm orifice). The sensor crystal of the QCM was mounted in the center of the chamber facing the orifice of the pulse valve. The orifice-crystal distance amounts to 18 cm in this setup.

In the first measurement, the opening time of the pulse valve was varied from 10 ms to 100 ms while the time between two injections was kept constant at 100 ms. The overall deposition time was 150 s for each pulse interval. Therefore, the number of in-

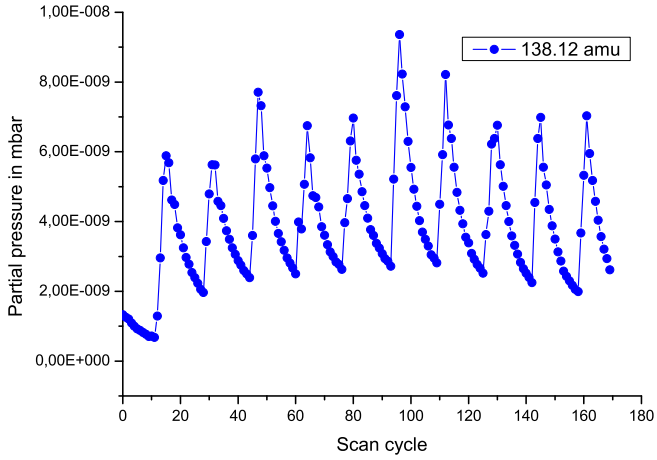

Figure 5.7: Mass spectrum taken during the repeated (10 times overall) injection of salicylic acid soluted in ethanol into the UHV chamber.

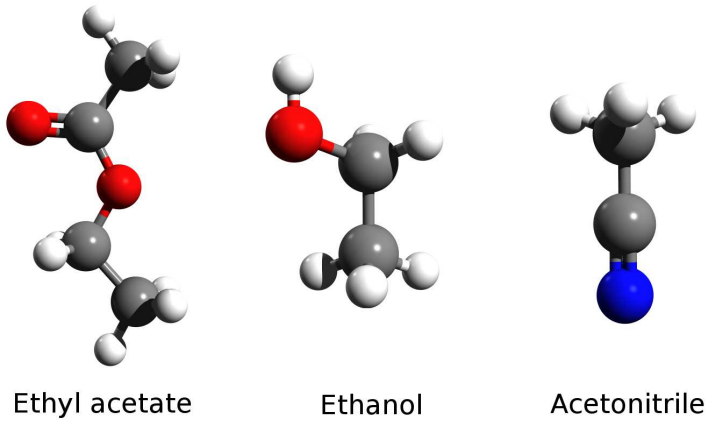

Figure 5.8: Molecular models of the three solvents used.

jections varied between 45 in case of 10 ms opening time and 25 in case of 100 ms opening time. The total deposition indicated by the QCM after the 150 s in two measurement series can be seen in Fig. 5.9. As can be seen, the overall deposition usually is in the order of a few angstrom independent of the pulse duration. The outlier at 80 ms pulse duration can be attributed to an external disturbance.

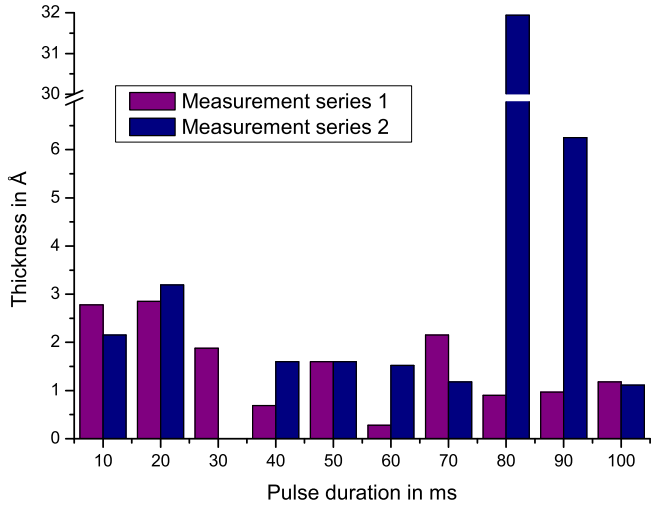

Figure 5.9: Deposition of salicylic acid from ethanol solution as a function of pulse duration. The overall deposition time amounts to 150 s in every case.

On a positive note, there is a measurable increase in thickness in every but one (series 2, 30 ms) attempt. Since the natural fluctuation of the quartz crystal and the corresponding ostensible thickness variation is random in both, positive and negative, direction, the observed increase in thickness can be directly attributed to pulse injection. Interestingly, however, the amount deposited does not seem to be significantly influenced by the pulse duration. This is also supported by QMS data. The QMS was locked to 138 u during the measurement series and the spectrum taken clearly reveals an increase in the partial pressure of salicylic acid upon opening the pulse valve (see Fig. 5.7). The height of the peaks and therefore the amount of salicylic acid injected into the chamber does not scale with the pulse duration, but appears to be roughly the same for each opening time. In general, the partial pressure that arises due to the injection of salicylic acid is always in the range of a few picobar. Thus, there is a good agreement of QCM and QMS data, allowing for the conclusion that the opening time does not significantly influence the deposition, at least on a time scale of 10 ms) and more.

In order to check for the influence of the solvent, salicylic acid

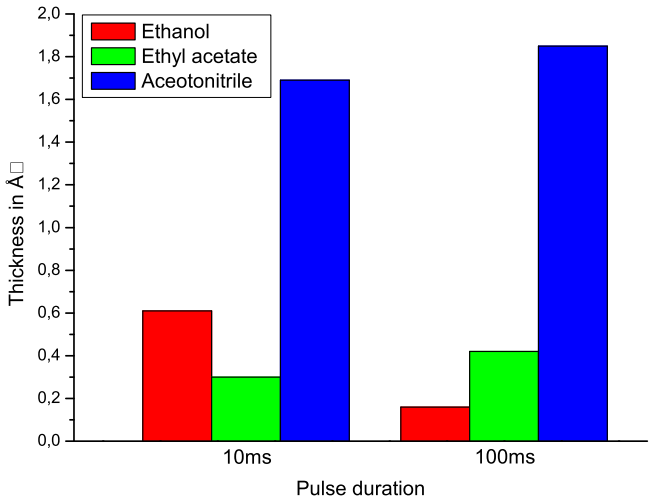

Figure 5.10: Deposition after 150 s for all three solvents used with two differing pule durations.

solved in ethyl acetate and acetonitrile, respectively, was studied as well. As with ethanol, the characteristic peak attributed to single-ionized salicylic acid is always visible in the mass spectra immediately after injection of the solution. A comparison of the results obtained with all three solvents at two different pulse durations is given in Fig. 5.10. Here, the thickness values were obtained by averaging over several (7 to 19) measurements. As can be seen, the average deposited thickness is largely independent of the pulse duration and usually amounts to about 1 Å, which translates to less than one molecular layer. Remarkably, this is also the case when the overall operation time of the pulse valve is increased to several minutes. Due to this very small signal, a highly effective isolation of the QCM crystal from environmental disturbances, for example by the use of temperature stabilized cooling water and vibration-damped mounting of the chamber, is necessary in order to further quantify the deposition by pulse injection. Based on the results at hand, however, one can draw the conclusion that acetonitrile as a solvent seems to be best suited for the salicylic acid deposition by pulse injection.

In conclusion, first experiments with the pulse injection setup as

described above show promise in the sense that molecules (salicylic acid) were successfully injected into the MBE chamber from three different solutions. A satisfactory quantitative control of the amount deposited by pulse injection, however, has not been achieved yet and demands further activity.

In addition, deposition by pulse injection was also tested with the help of STM in the VT AFM system described in Chap. 2. First results are presented in the appendix.

6 Focused ion beam implantation

Contents

As pointed out in the introduction, a main motivation of this thesis is to lay the foundation for the implementation of a quantum computer concept. This concept, which is described in detail in Chap. 4, is based on the positioning of PEFs atop nitrogen vacancies close to the surface in diamond. The density of these subsurface NV centers, however, is of course limited by the nitrogen dopant concentration and is therefore very low (<1 ppm) for high-purity diamond. In addition, the spatial distribution and depth of the vacancies is random. It would therefore be greatly beneficial to be able to artificially create nitrogen vacancies of well-defined depth at distinct surface positions. This could be done by means of focused ion beam (FIB) implantation. In this technique, ions are accelerated towards the surface with an energy that is sharply defined by the applied acceleration voltage. Hence the kinetic energy of the ions can be chosen based on the desired penetration depth. The lateral location of the implantation can as well be precisely confined, for example by using a hollow AFM tip.

In the following, early results of a cooperation with the group of Prof. *name removed for privacy* (AG Quantum, Physics Department, Johannes Gutenberg-Universität Mainz) aiming at targeted ion implantation are presented. As first objectives, it was studied to what degree the implantation spots can be identified and imaged with AFM. For this purpose, argon cations were implanted by the AG Quantum into $CaF_2(111)$ orientated single crystals prepared by us. Subsequently, the effect of the implantation on the surface was studied with NC-AFM in UHV and tapping AFM in air.

Argon was chosen because the technical realization of implanting argon ions was already well under control at the time of the experiments, in contrast to the implantation of nitrogen, which is technically much more challenging. Calcium fluorite as a test substrate has, compared to diamond, the advantage that atomically flat and clean terraces extending over several micrometers can easily be prepared (see Chap. 3). This allows for the detection of very small changes in surface morphology by means of AFM. The diamond surface on the other hand is strongly fissured on the nanoscale, the typical terrace size is in the order of a few nanometers (see Chap. 4). In addition, even the clean surface features a number of protrusions, which can be ascribed to nanodiamonds. These surface characteristics can complicate the identification of changes in surface morphology caused by ion implantation. For these reasons, the $CaF_2(111)$ surface was chosen for the basic implantation experiments.

In this thesis, the focus is mainly on AFM imaging. Consequently, the implantation itself is not part of this thesis, but was described in detail in the framework of a diploma thesis written by *name removed for privacy* of the AG Quantum. Please refer to his diploma thesis[98] for technical details regarding the FIB implantation as done in this project. For additional information, reviews written by John Melngailis[99] and Jacques Gierak[100] can be recommended as informative compendia of the FIB technique.

6.1 Sample preparation

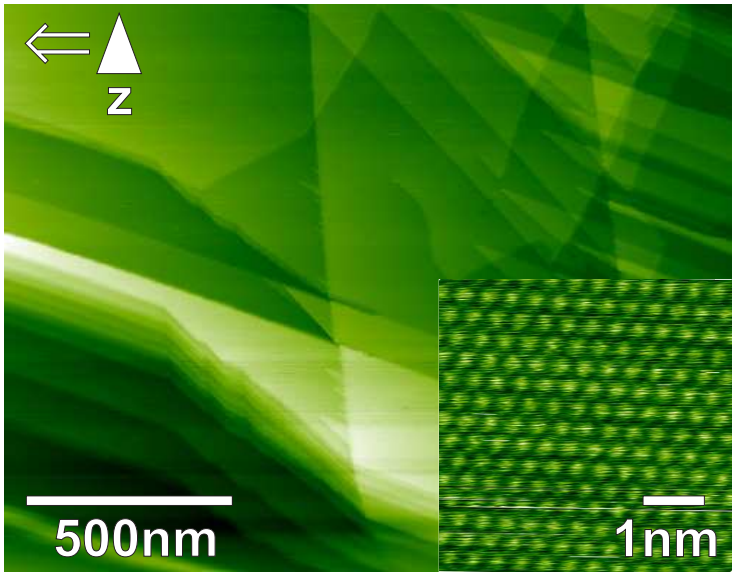

Figure 6.1: NC-AFM topography image of a CaF_2 (111) surface prior to C_{60} sublimation. The inset displays the atomically resolved surface structure.

Prior to ion implantation, the CaF_2 samples were annealed and cleaved under UHV conditions as described in Chap. 4. The (111) surfaces freshly created this way were imaged with NC-AFM to check for terrace size and possible impurities. If the surface appeared to be reasonable clean, as depicted in Fig. 6.1 for illustration, C_{60} fullerenes (MER Corporation, Tuscon, Arizona; purity of 99.95%) were deposited onto the surface under UHV conditions. This was done by thermal sublimation from a Knudsen cell held at temperatures in the range of 650 K to 680 K, aiming at a coverage of 10 nm to 20 nm. The purpose of this C_{60} coating is to build a protective layer on top of the bare CaF_2 surface in order to insulate the surface from adsorbates that would inevitably contaminate the surface upon exposure to air. This coating, however, must be removable by *in-situ* annealing and also still allow for the ions to penetrate it.

As can be seen in Fig. 6.2, C_{60} island growth was observed upon deposition by sublimation. The surface is covered with multilayer C_{60} islands up to a height of 14 nm, which corresponds to at least 14 - 18 layers of C_{60}. CaF_2 step edges act as preferred

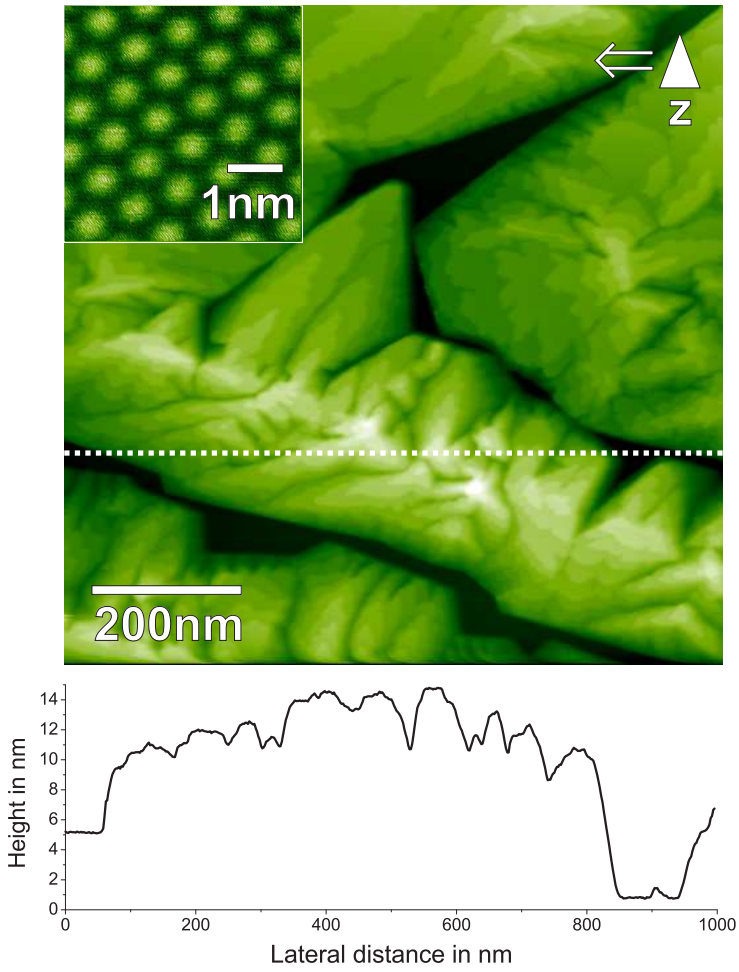

Figure 6.2: NC-AFM topography image of a CaF_2 (111) surface coated with C_{60}. The inset displays the hexagonal molecular structure of C_{60} on the lowest layer. A line profile was taken along the dashed white line and is depicted below the NC-AFM image.

nucleation sides and are therefore easily recognizable even at high coverages. The islands, which are stable at room temperature, narrow with height, which results in a rather heterogeneous C_{60} coverage. In between the islands, small gaps with no visible protrusions are apparent. To make sure that those areas are as well covered with at least one layer of C_{60} and do not show the bare substrate, small-scale images focused on such surface regions were taken (see inset in Fig. 6.2). The high-resolution images reveal a hexagonal surface structure with a

nearest neighbor distance of 1 nm. This structure is in strong contrast to the bare CaF_2 surface, where a distance of 0.39 nm would be expected (see surface model in Chap. 3).
Instead, the dimensions are in very good agreement with the fcc

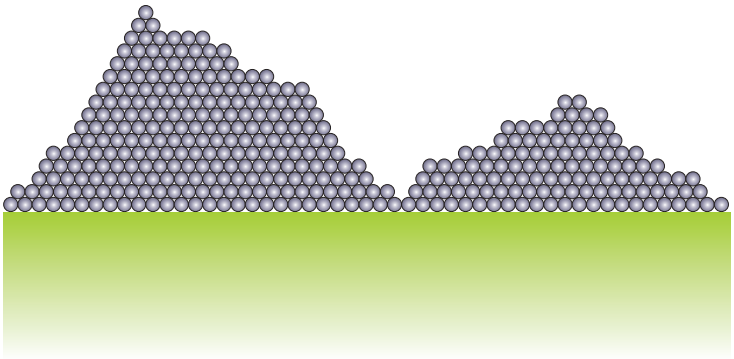

Figure 6.3: Model of the C_{60} growth on the CaF_2 (111) surface. Every part of the surface is covered with at least one layer of C_{60}, which stacks up to multilayer islands.

structure of C_{60}. Therefore it can be concluded that every surface region is indeed covered with at least one layer of C_{60} as depicted in Fig. 6.3. Interestingly, this finding is somewhat contrary to previously obtained NC-AFM results, where complete dewetting of C_{60} on the CaF_2 surface was observed[101]. The main difference here is the amount of C_{60} deposited, since the previous studies focused on sub-monolayer coverages. Apparently there is a threshold coverage above which a complete dewetting is no longer achieved. This can be explained by taking into account a recently published study by Rahe *et al.* [102], where the wetting behavior of C_{60} upon deposition on a great variety of ionic surfaces was compared. As a result, Rahe *et al.* were able to show that an accurate prediction of whether C_{60} wets or dewets a surface can be made based on the macroscopic surface energy of the substrate. With a surface energy of 480 mJ m^{-2}, CaF_2 is at the very end of surfaces that are still regarded as dewetted by C_{60}. Hence, at very high coverages as deposited in this thesis, the multiple energy barriers to be overcome for a C_{60} molecule to make the transition from the first to the highest layer (14$^{\text{th}}$ or more) may result in a significant proportion of fullerenes remaining in the energetically only slightly disfavored first layer.

Upon annealing at 430 K for 1 h, neither a significant growth in island height nor a widening of the troughs in between the is-

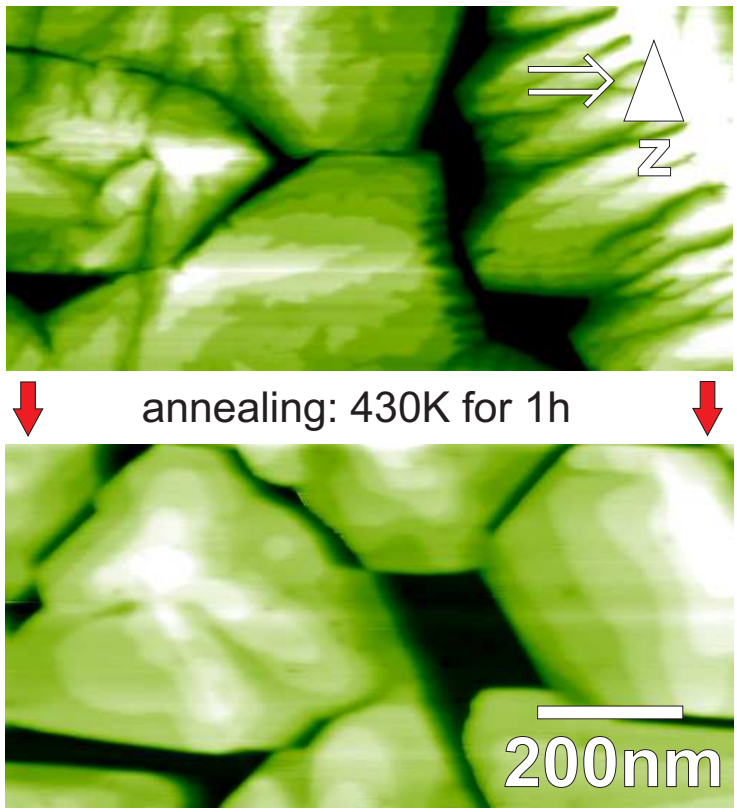

Figure 6.4: Effect of annealing on the C_{60} adlayer.

lands was observed. However, the single C_{60} terraces of the islands appear more uniform, indicating diffusion of the C_{60} on the islands to have happened in order to form closed layers. Regarding the suitability of the C_{60} adlayer for protecting the $CaF_2(111)$ surface, subsequent moderate annealing thus has neither beneficial nor detrimental effects.

6.2 Effect of sample exposure to air

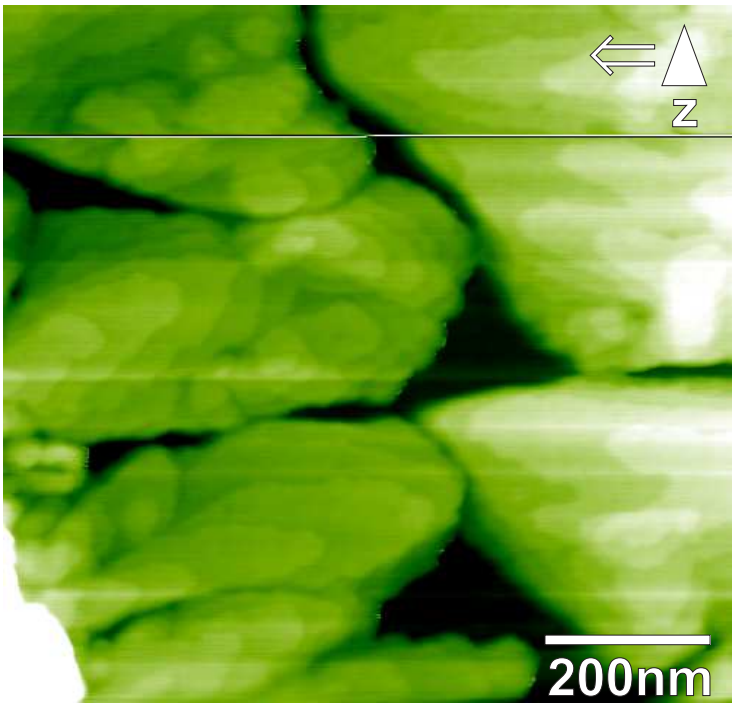

Figure 6.5: NC-AFM topography image of a $CaF_2(111)$ coated with C_{60} after exposure to air.

In order to check for the stability of the C_{60} adsorption layer, the samples were locked out after preparation and exposed to air for several hours. Subsequent imaging with NC-AFM was not possible at first, the surface appeared to feature adsorbates too high to allow for stable scanning. In order to remove those adsorbates from the surface, the sample was annealed at 485 K for 1 h. This treatment proved to be successful and the surface then revealed a largely unchanged surface compared to the UHV situation immediately after preparation (see Fig. 6.5). Even the troughs in between the islands, where the protecting C_{60} adlayer is the thinnest, appeared largely clean. Hence it can be concluded that the C_{60} adlayer is not severely affected by exposure to air. This allows for a transfer of the samples from the UHV NC-AFM to the ion implantation chamber and back. Further annealing at 527 K results in a gradual desorption of the C_{60} adlayer (see Fig.

6.6). Hence, annealing under UHV conditions at this temperature or slightly above is sufficient to remove the C_{60} adlayer.

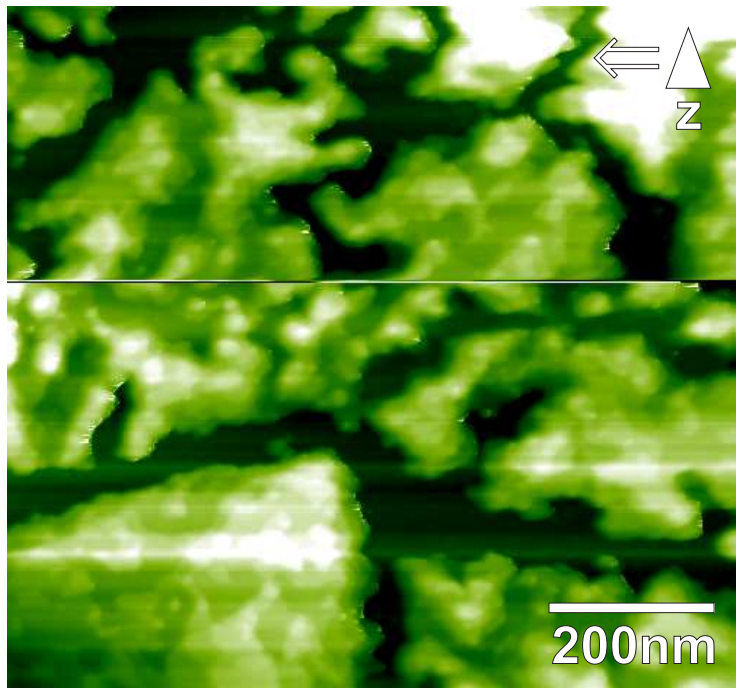

Figure 6.6: NC-AFM topography image of a $CaF_2(111)$ surface coated with C_{60} after annealing for 1 h at 527 K

6.3 Ion implantation

Three types of argon cations were implemented by means of FIB in a sample prepared as stated above:

- Ar^+ at 5 keV, intended spot diameter 20 µm
- Ar^+ at 3 keV, intended spot diameter 20 µm
- Ar^{2+} at 5 keV, intended spot diameter 20 µm

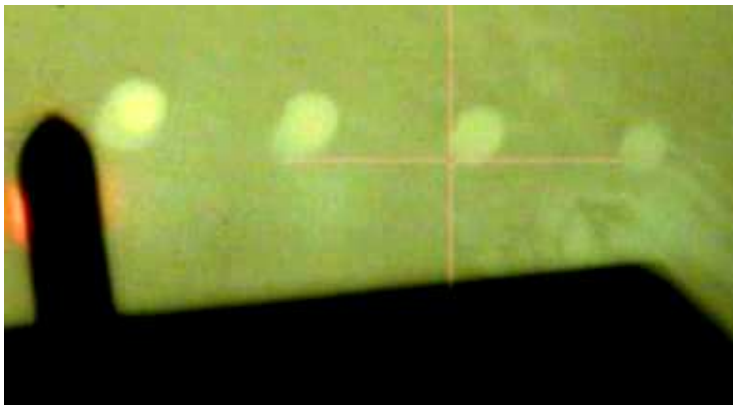

Figure 6.7: Optical microscope image of argon ion implantation centers on the $CaF_2(111)$ surface. The implantation duration was decreased from left (56 s) to right (1.8 s). The cantilever used for imaging the spots can be seen in the left hand corner.

In addition, the implantation time was varied between 56 s and 1.8 s, regulating the number of ions implanted. The spots are aligned in line in a distance of 100 µm. They are partly visible with an optical microscope, which in principle enables pinpoint positioning of the cantilever directly atop such an implantation spot (see Fig. 6.7). However, due to the setup of the UHV system hosting the NC-AFM, this is so far only possible when doing tapping or contact mode AFM in air.

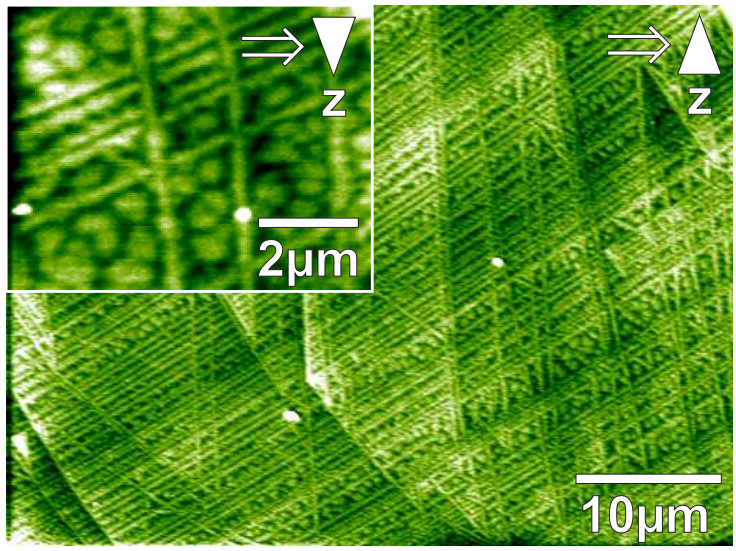

Figure 6.8: Tapping-AFM topography image of a $CaF_2(111)$ surface coated with C_{60} after ion implantation.

6.4 AFM measurements after implementation

In order to observe the impact of ion implantation on the surface structure, the samples were imaged with a customized MultiMode V AFM (Bruker AXS, Madison, Wisconsin) in tapping mode. As can be seen in Fig. 6.8, the surface is still well covered with C_{60} and does not differ in appearance from the freshly prepared surface.

Interestingly, the implantation spots visible with the optical microscope are only visible in the AFM images when the implantation time is long enough (minimum of 1.8 s for Ar^+ at 5 keV, 5 s for Ar^+ at 3 keV and 5.6 s for Ar^{2+} at 5 keV). Fig. 6.9 gives an overview over the implantation spots, ordered by implantation energy, ion charge (single or double) and implantation time. As can be seen on first glance, the ion bombardment did result in the formation of circular protrusions with a diameter of about 20 µm.

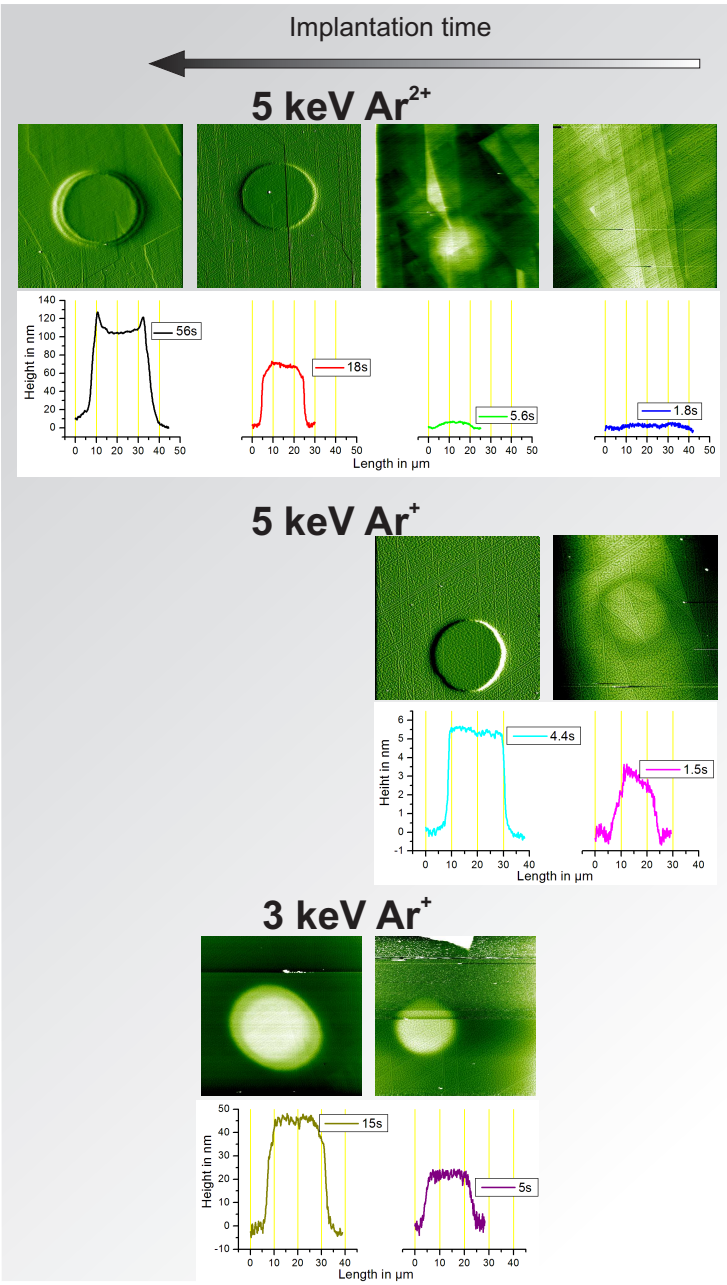

Figure 6.9: Overview of the implantation spots as imaged with tapping AFM. All AFM images are 50 µm in size and either topography or amplitude images, depending on contrast formation. The implantation time decreases from left to right, ion charge and energy decrease from top to bottom. In the first row, 5 keV/Ar^{2+} spots are depicted, the second row features 5 keV/Ar^{+} protrusions and in the third row, protrusions caused by 3 keV/Ar^{+} bombardment are displayed. Below the AFM images of one series, line profiles across the middle of the according spots are depicted.

As expected, the height and therefore the number of ions implanted does in general increase with implantation time. This is true for every combination of ion energy and charge tried, but most remarkable in case of the 5 keV/Ar^{2+} implantation spots. While the 56 s spot has a height close to 100 nm and a base width of 33 µm, the 5.6 s spot is barely visible due to its strongly reduced height 6 nm and width 18 µm. The spot corresponding to 1.8 s is even less pronounced, from the AFM images alone its existence can only be suspected.

An overview over the measured spot heights with respect to implantation time and charge state is given in Fig. 6.10. When comparing the impact of simply charged and doubly charged ions of same energy (5 keV), a very good agreement of the observed heights is evident. The valency of the implanted ion thus seems to have no significant impact on the implantation depth. Interestingly, though, the protrusions caused by slower ions (3 keV) are more pronounced than those caused by faster ions (5 keV) at the same implantation time. A possible explanation is a larger penetration depth of the high energy ions. Definite conclusions, however, cannot be drawn due to the limited data size.

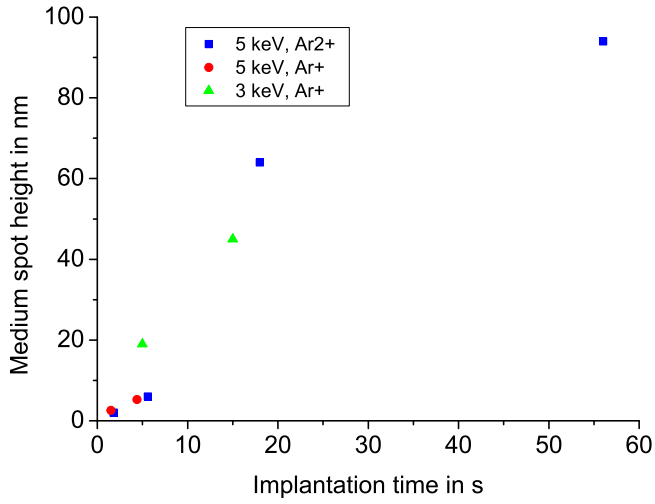

Figure 6.10: Spot height as a function of implantation time.

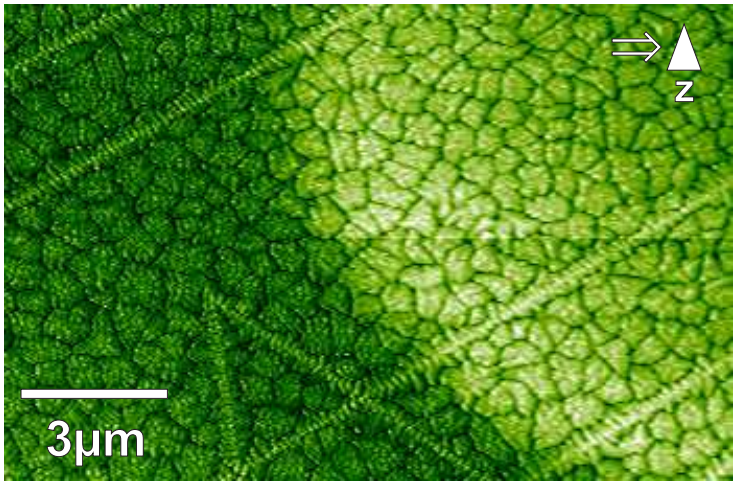

Figure 6.11: Tapping AFM topography image of the edge of an implantation spot.

In any case, the C_{60} adlayer appears undamaged by the bombardment. As can be seen in Fig. 6.11, the layer transition from surface to implantation spot is very smooth. No change of the surface texture is visible, step edges and C_{60} islands both extend across the spots seamlessly. This allows for two fundamentally different explanations: Either the argon ions pass through the film without enduring effect on the fullerenes, or the C_{60} film reassembles after ion implantation. The latter is unlikely since C_{60} is mobile on the $CaF_2(111)$ surface at room temperature only as long it has not assembled to stable islands[101]. The islands itself are immobile and single C_{60} fullerenes enclosed in an island are locally fixed (aside from rotation around their axis). Even assuming a local annealing of the surface by the ion beam does not bear a convincing explanation, since this would likely result in a visible change in island morphology on the spots compared to the surrounding surface or, when the temperature is high enough, even in C_{60} desorption. Hence it is likely that the argon ions pass the C_{60} adlayer in a ballistic manner.

Another remarkable feature of the implantation spots is the fact that they can only be imaged with AFM when the tip is in a suitable configuration. Otherwise, the surface appears flat in the topography image and only a small corona is visible in the phase image. This can be nicely seen in Fig. 6.12. Here, the tip changed

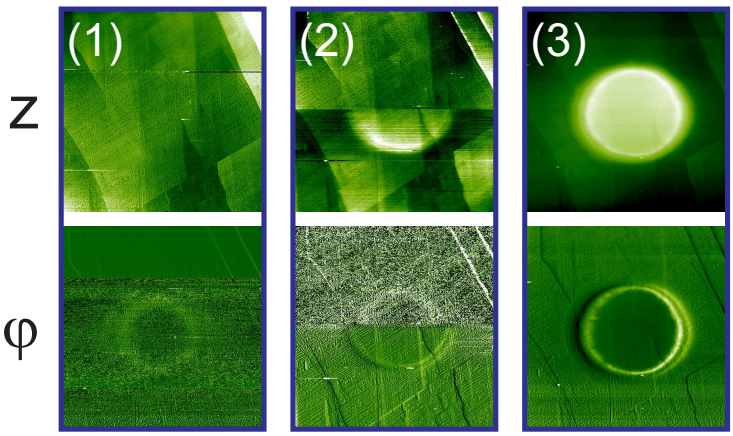

Figure 6.12: Tapping AFM images illustrating the effect of the tip coordination on imaging an implantation spot ($5\,\mathrm{keV/Ar^{2+}}$, 56 s). In the upper row, topography images are displayed, the lower row shows the according phase images. All images feature the same surface region and were taken with the same tip in immediate succession as displayed here. At first (1), the implantation spot is not imaged in the topography channel but only in the phase image as a faint corona. As a result of a tip change (2), the spot becomes clearly visible (3), exhibiting a "height" of around 100 µm.

while scanning the implantation spot and with the tip change, the protrusion suddenly appeared in the image. This suggests that what is imaged as a protrusion is in fact a charged patch on the surface. This comes as no surprise when considering that the surface has been bombarded with cations, which cause a local net increase in charge when incorporated into the crystal. Since CaF_2 is a very good insulator (band gap: 12.1 eV[31]), those charges cannot simply dissipate and therefore accumulate in a spatially well-defined, positively charged patch. When the tip is also positively charged, a repulsive electrostatic tip-sample interaction arises, which naturally results in the patch being imaged as a protrusion. Due to the excess charge at this position, a tip change while scanning the implantation spot can eventually be caused by charge transfer to the tip, changing its polarization and therewith the appearance of the spot in the AFM image. Attributing the spots to charge effects would also nicely explain the seamless crossing of the spot boundary by the C_{60} adlayer despite the apparently huge step between surface and implantation spot. If the observed protrusion is not real but can be fully attributed to electrostatic interaction, there is no reason why the non-polar C_{60} islands should not simply extend across the spot boundary.

This tip dependence naturally decreases the credibility of height measurements on the spots. However, images taken with tips in the same state are still comparable since what is displayed as

height in the topography images translates directly to the charge implanted within the spot. Both height and charge can likewise be treated as indicators for the amount of ions implanted and do therefore in general yield the same information.

6.5 Outlook

To image the effect of the ion implantation in more detail and especially without the protective C_{60} layer, NC-AFM measurements under UHV conditions are necessary. This, however, turned out to be very challenging for a number of reasons. First of all, locating the spots is hardly possible in the customary setup of the NC-AFM. The implantation spots are not visible in the positioning camera of the NC-AFM and the piezo tube actuator holding the cantilever does not allow for positioning of the tip at absolute coordinates with respect to its normal position. Hence, only a course positioning of the tip in the vicinity of some hundred micrometer around the actual implantation spot is feasible. In combination with a rather small maximum scan frame of 8 µm and the necessity to scan over the boundary of a spot in order to be able to identify it as such, this makes finding the spot nearly impossibly. In addition, the apparent height difference of several tens of nanometers as observed for long implantation times far too big to enable stable imaging with NC-AFM.

To overcome these problems, improvements over the current setup are in progress. A long distance microscope (K2/SC, Infinity, Bulder, Colorado) equipped with a suitable objective as well as supplemental tube amplifiers was purchased. This microscope will allow for *in-situ* close-up imaging of the sample in order to visualize the implantation spots and to enable positioning of the cantilever tip of the UHV NC-AFM.

Regarding the ion implantation, a guiding raster of implantation spots will be carved into the sample to allow for a more targeted tip approach. In addition, a hollow AFM tip will be used as a mask during implantation. Thereby, ions are implanted into a small circular region of only 10 nm to 30 nm in diameter that is sharply separated from the surrounding pristine surface (see Fig. 6.13).

Figure 6.13: Model of the so-called "Pacman" implantation profile.

These measures will allow for high-resolution NC-AFM studies of the implantation spots, ideally resolving the impact of single ions on the surface. As further steps, the targeted implantation of nitrogen ions instead of argon ions into CaF_2 crystals and, finally, into (100) oriented CVD diamonds are envisaged.

7 NC-AFM study of the diamond C(100) surface

Contents

In this chapter, the results of NC-AFM studies on diamond C(100) surfaces are presented. The first part deals with the hydrogen-terminated diamond C(100)-(2 × 1):H surface, while the second part gives attention to the pure diamond C(100)-(2 × 1) surface. In both cases, the focus is on obtaining high-resolution images resolving individual surface atoms. Surface characteristics including terrace size, different types of step edges, atomic defects and anti-phase boundaries were imaged and are explained in the following.

7.1 Motivation

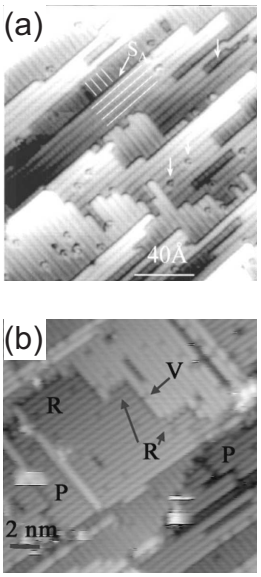

Figure 7.1: STM images of (a) the hydrogen-terminated C(100)-(2 × 1):H surface[94] and (b) the pure C(100)-(2 × 1) surface of boron doped diamond[103].

Due to the fact that diamond exhibits a surface conductivity upon hydrogen termination, the electronic structure of the C(100)-(2 × 1):H surface can be imaged with STM in high resolution. Consequently, the huge scientific and economic appeal of diamond caused by its outstanding material properties (see Chap. 4) in combination with the widespread use of STM led to a variety of STM studies on hydrogenated diamond surfaces[28,86,93–95]. Those studies gave real-space evidence for a perpetuation of the (2 × 1) reconstruction of the C(100) surface after hydrogenation and allowed for temperature optimization of the CVD growth of well defined diamond surfaces.

Despite the deeper knowledge and better understanding of the surface that was obtained with the help of STM, there are limitations to this technique that necessitate the use of alternative measurement methods such as NC-AFM. Because of the fact that STM is always based on the measurement of the tunneling current that occurs in every data point, the surface information won by STM is influenced the most by the electronic structure of the surface. Hence, not the true surface topography is imaged, but the (somewhat related) electronic structure of the surface. Because of this, some surface characteristics can not be imaged with STM. While individual surface dimers can be revealed, the single atoms forming the dimers as well as the hydrogen atoms attached to them in case of the hydrogen-terminated surface have never been imaged with STM. Therefore, the hydrogenated diamond C(100)-(2 × 1):H surface can not be distinguished from the bare diamond C(100)-(2 × 1) surface by STM images alone (see Fig. 7.1).

As another drawback, high-purity, hydrogen-free diamond C(100)-(2 × 1) is nonconducting and therefore not readily accessible to STM imaging. To circumvent problems in surface analysis that are related to the insulating nature of the material, samples are often doped with boron. Such doping allows for STM imaging even in the absence of adsorbed hydrogen[28,103]. A particularly interesting example has been STM imaging using resonant electron injection at 5.9V[87]. Using this high sample bias voltage, imaging has been explained by resonant injection of electrons

into a standing-wave resonance located above the surface vacuum level. However, both conventional STM imaging as well as resonant injection requires the existence of conductance channels within the applied voltage window, which is ensured by the conduction bands, surface states or by the presence of dopants. Most of the diamond samples, both natural diamond and artificial CVD diamond, have a low impurity concentration and are insulating. For example, high-purity, type IIa diamond exhibits an impurity concentration of less than 1 ppm and does, in contrast to boron-doped samples, not show any conductance channels within the voltage regime ranging from −10 V to 10 V and therefore excludes STM imaging even of the hydrogenated surface unless a water layer is present[95].

Consequently, it is expedient to resort to another high-resolution surface imaging technique, namely NC-AFM. Despite many attempts, though, atomic-scale AFM imaging of diamond surfaces has not been successful so far for several reasons (refer to Sec. 7.5 for details). Nonetheless, for this particular surface, AFM offers the potential of even higher resolution imaging than what had previously been obtained using STM, as AFM images the interaction forces rather than the electronic structure. In the past, NC-AFM measurements have yielded high-resolution images of both bare dielectric substrates[104–107] and molecules on insulators[108–111]. Recently, even sub-molecular resolution has been achieved upon imaging a pentacene molecule at low temperature (5 K)[16].

7.2 Experimental setup

An extended description of the NC-AFM experimental setup is given in Chap. 2. In short, experiments were performed at room temperature (RT) in an UHV system with a base pressure lower than 10^{-10} mbar. The system is equipped with a VT AFM 25 atomic force microscope (Omicron Nanotechnology, Taunusstein, Germany) and an easyPLL Plus phase-locked loop detector and amplitude controller (Nanosurf, Liestal, Switzerland) for oscillation excitation and signal demodulation. N-doped silicon cantilevers (NanoWorld, Neuchâtel, Switzerland) with resonance frequencies of about 300 kHz (type PPP-NCH) were used, excited to oscillation with an amplitude of about 10 nm.

The type IIa CVD diamond samples used in this study are 3.0 mm × 3.0 mm × 0.5 mm in size and are described in detail in Chap. 3. The samples are undoped and therefore non-conducting. According to the supplier, the impurity concentration is below 1 ppm, with nitrogen being the largest portion. The investigated diamond (100) surfaces of the samples were etched and hydrogenated *ex-situ* in a hydrogen plasma, as described in detail in Chap. 4. The hydrogenated diamond samples were transferred into the UHV system and annealed to approximately 900 K for 1h to remove adsorbed contaminants from exposure to air, using a pyrolytic boron nitride radiation heater. This procedure is known to provide clean C(100)-(2 × 1):H surfaces[94]. The hydrogen can later be removed by further annealing of the sample at a temperature of above 1200 K[112], which was in this case performed by heating the sample indirectly through a tantalum stripe mounted directly underneath the sample. The sample temperature was measured using an IR pyrometer (Sensortherm, Sulzbach, Germany) with the emissivity set to $\epsilon = 0.2$. Similar as done by Maier *et al.*[90], the absolute surface temperature is estimated to be 100 K to 200 K lower than the displayed temperature, since annealing the surface to a nominal temperature of 1330 K (as measured with our pyrometer) did not result in the removal of the hydrogen layer. During annealing, the pressure in the UHV chamber rises temporarily by about one order of magnitude.

7.3 NC-AFM on hydrogen-terminated diamond C(100)-(2 × 1):H

Surface structure on the atomic scale

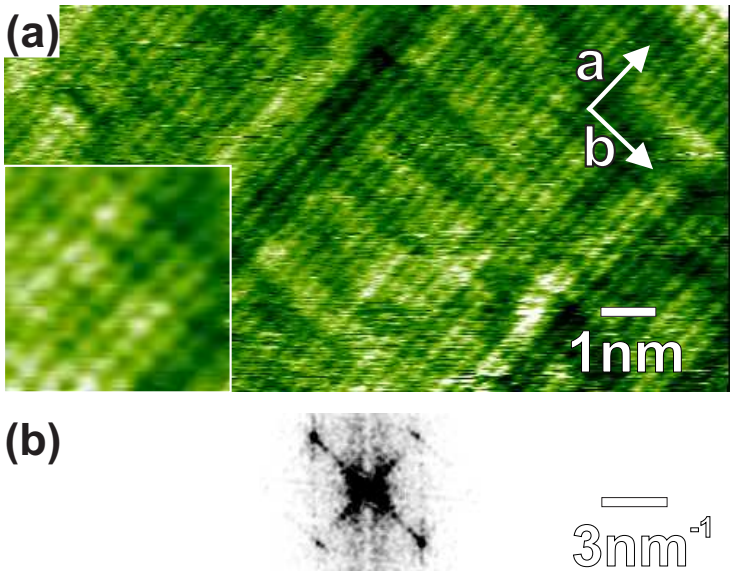

Figure 7.2: (a) NC-AFM frequency shift image of the hydrogen-terminated diamond C(100)-(2 × 1):H surface (drift corrected raw data). To the lower left, a three-point mean filtered zoom (25 Å × 25 Å) is added in order to show more clearly the atomic resolution. White arrows indicate the the unit cell directions. (b) 2D-FFT of the image shown in (a), revealing the unit cell dimensions of a = 2.62±0.05 Å and b = 2.53±0.04 Å.

Using the setup described above, it was possible to image the C(100)-(2 × 1):H surface with atomic resolution, as can be seen in Fig. 7.2. The image represents raw data except for a drift correction that is applied as described elsewhere[113]. Fig. 7.2(a) shows individual bright features, which are clearly visible in the enlarged view of a smaller area (25 Å× 25 Å), forming the surface layer in an almost square arrangement. A two-dimensional fast Fourier transformation (2D-FFT) of the image was performed in order to determine the distance between the protrusions (Fig. 7.2(b)). As can be seen, the spacing between the topmost atoms, having dimensions of a = 2.62±0.05 Å and b = 2.53±0.04 Å, is nearly square. These inter-atomic distances are in good agreement with previously published calculations of the diamond C(100)-(2 × 1):H surface structure, suggesting a hydrogen distance in the range of 2.58 Å[114,115] to 2.62 Å[83] in [011] direction

and 2.52 Å[83,116] in [0$\bar{1}$1] direction, respectively. These dimensions clearly indicate that both hydrogen atoms within the unit cell are resolved individually, providing additional details to former STM measurements, which reveal electronic orbitals in between adjacent hydrogen atoms as bright dimers[94]. The present observation therefore allows for two conclusions:

1. Confirmation of the monohydride model.

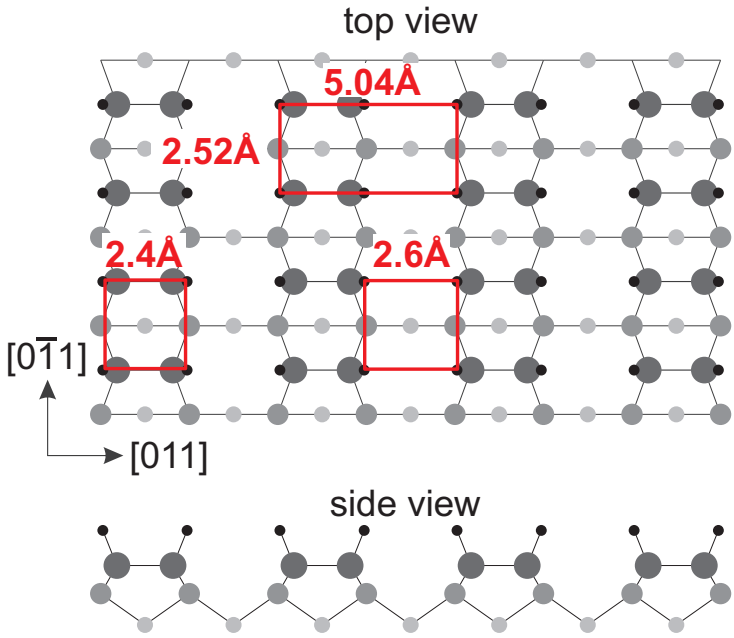

Figure 7.3: Model of the diamond C(100)-(2 × 1):H structure. Hydrogen atoms are depicted black, carbon atoms in different shades of gray according to their position (the darker, the closer to the surface).

The observed structure is not consistent with any hydrogen termination other than the monohydride model, which results in a C(100)-(2 × 1):H surface structure as depicted in Fig. 7.3. Here, one hydrogen atom is attached to each of the topmost carbon atoms. The observed structure comes as no surprise because the monohydride surface termination is known to be the most stable confirmation when the surface is completely covered with hydrogen[117].
Nonetheless, a dihydride surface structure (C(100)-(1 × 1):2H) was observed in LEED measurements performed by Lurie and Wilson[84] and (3 × 1) reconstructed surface areas were observed

with STM before[28,118]. In our measurements, however, neither (1 × 1) nor (3 × 1) reconstructed surface areas are present, the (2 × 1) reconstructed surface was imaged exclusively.

2. Indication of symmetric C—C dimer alignment.

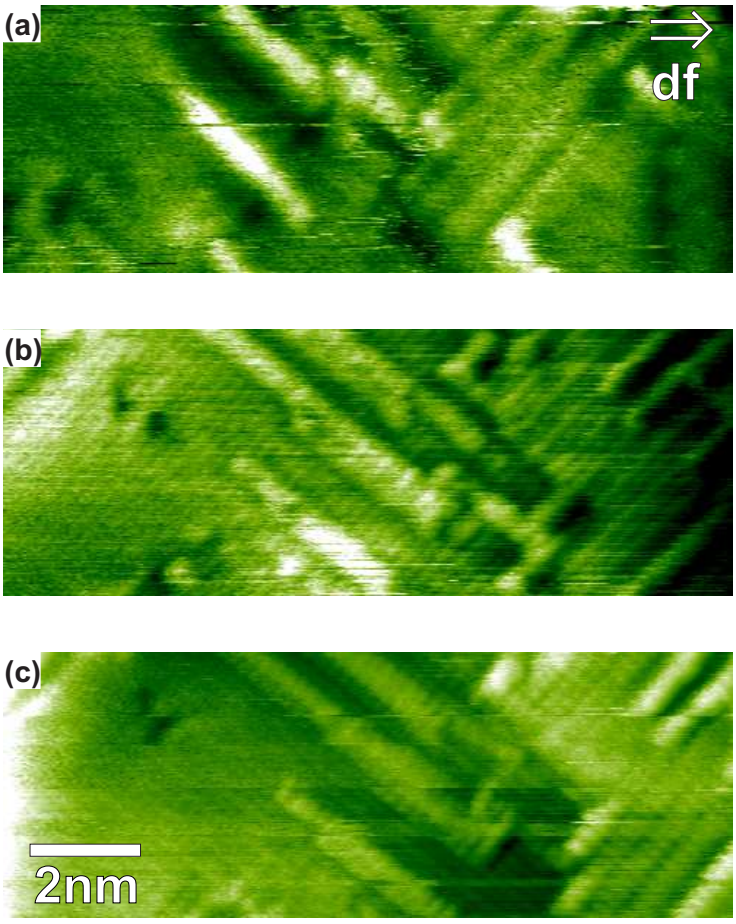

Figure 7.4: NC-AFM frequency shift images showing contrast formation on the hydrogen-terminated C(100)-(2 × 1):H surface. All three images contain roughly the same surface area. In (a), terraces and dimer rows are already visible, but no atomic contrast in any surface direction is achieved. (b) Already yields atomic contrast in one surface direction, but only (c) displays true atomic resolution: Here, dimer rows as well as single hydrogen atoms are visible. This "full-contrast mode" is naturally very unstable for reasons described in Sec. 7.5.

The fact that both hydrogen atoms of one dimer are imaged with roughly the same height and do not feature a regular asymmetry allows for the conclusion that no dimer buckling is observed. While this observation can not be regarded as prove for the non-existence of dimer buckling on the C(100)-(2 × 1):H surface, it nonetheless provides a clear indication of a symmetric

dimer alignment, which is in agreement with theoretical calculations[119].

While NC-AFM images showing the individual dimers of the C(100)-(2 × 1):H surface can only be acquired under perfect circumstances, images yielding dimer row resolution are achieved more frequently. Rarely, even the transition from row resolution to true atomic resolution can be witnessed within the same surface area. (Fig. 7.4).

Surface characteristics

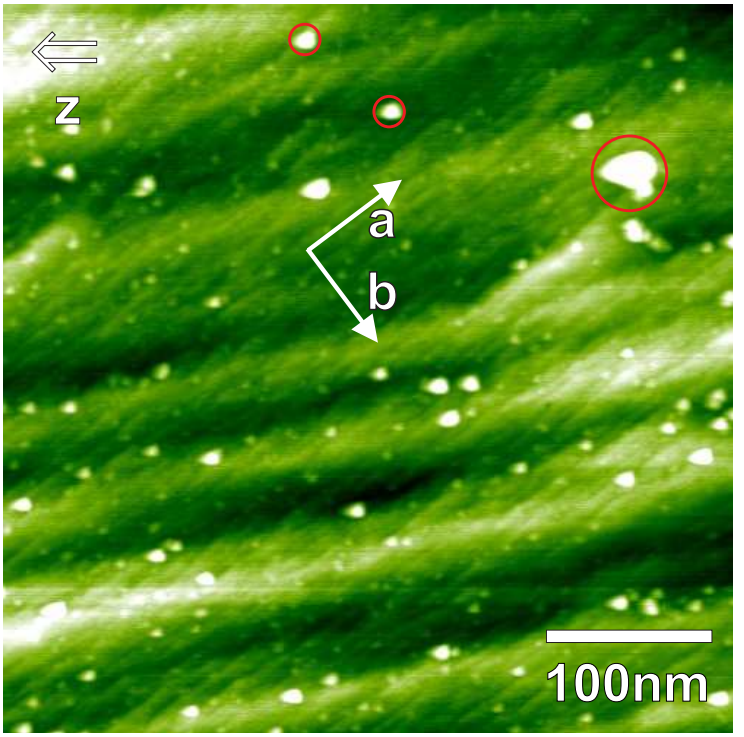

Figure 7.5: Large-scale NC-AFM topography image of the hydrogen-terminated C(100)-(2 × 1):H surface. The surface is characterized by wide polishing stripes overlayed with small rectangular terraces as indicated by white arrows pointing in [0$\bar{1}$1] and [011] direction, respectively. The surface also features a number of protrusions that are assigned to nanodiamonds and partially marked with red circles.

As can already be seen in Fig. 7.4 and in a larger frame in Fig. 7.5, the diamond surface is highly fissured on the nanoscale. Terraces usually extend only over a few nanometer. While the

surface is largely free of adsorbates on the atomic scale, it features irregularly distributed, but sharply defined protrusions with heights up to a few nanometer, as can be seen in Fig. 7.5. It is suspected that those protrusions are nanodiamonds that arise during the CVD growths of the surface. This assumption is supported by the fact that the tip apex is usually destroyed when contact is made between the tip and such a protrusion during scanning. The protrusions, on the other hand, appear unchanged after the contact. Thus, they cannot be manipulated with the AFM tip.

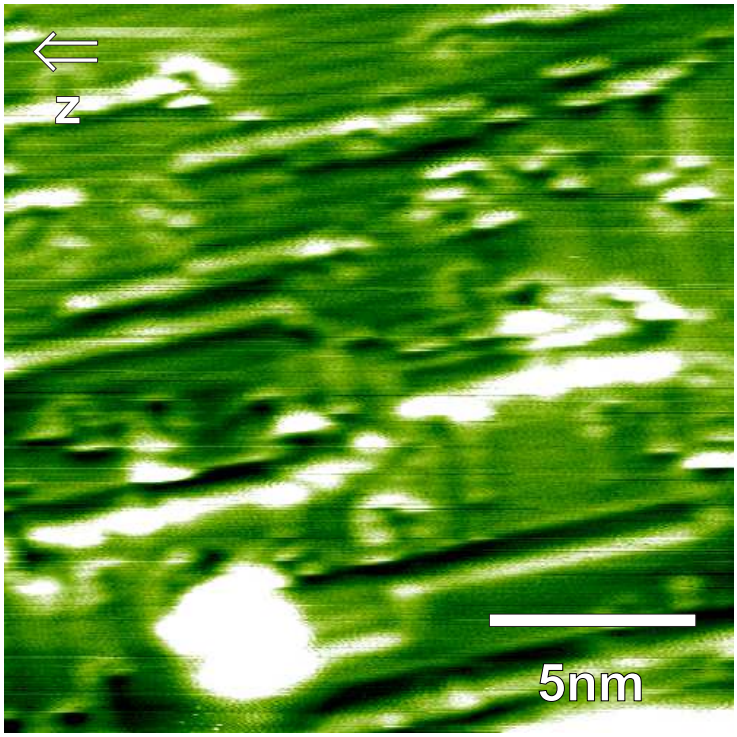

Figure 7.6: NC-AFM topography image of the hydrogen-terminated C(100)-(2 × 1):H surface after exposure to air for 9 month. The overall surface structure remains unchanged, but the defect density has increased over time.

The low density of adsorbates on the surface is due to the highly inert nature of the hydrogen-terminated surface. Consequently, the density of adsorbates increases as the hydrogen layer degenerates, for example by exposition of the surface to ambient conditions, as can be seen in Fig. 7.6. The figure displays the C(100)-(2 × 1):H surface of a sample that was kept under dark,

but exposed to air for 9 month. Besides the larger protrusions ascribed to nanodiamonds, a large number of small, localized depressions surrounded by adsorbates are visible on the surface. Those depressions have a depth of 0.8 Å to 1.0 Å, which is in good agreement of the theoretically calculated value of 1.0 Å for the difference in lateral distance between hydrogen atom and carbon dimer[115]. The depressions can therefore be attributed to defects in the hydrogen layer, which lead to a strongly localized, drastic increase of surface reactivity. The much increased sticking coefficient at those exposed surface sides results in a chemisorption of adsorbates from air, explaining the clustering of molecules around the dark spots. Apart from those irregular distributed defect sides, however, the overall surface structure appears largely unchanged, despite having been been covered with the inevitable water layer arising from exposure to air for 9 month. This underlines the great stability and inertness of the surface hydrogen layer. The very low reactivity of the hydrogen atoms bound to the surface carbon dimers do simply not allow for a chemisorption of adsorbates from the environment. Once the protective hydrogen layer is removed, however, the reactivity of the surface increases dramatically.

7.4 NC-AFM on pure diamond C(100)-(2 × 1)

In-situ annealing of hydrogen-terminated diamond samples beyond the hydrogen desorption temperature results in a complete transition from the C(100)-(2 × 1):H surface to the bare C(100)-(2 × 1) surface. The absence of any tunneling states within a reasonable voltage regime was confirmed by attempts to record current-voltage curves in a voltage range from −10 V to 10 V. No such curve could be obtained. Instead, the tip crashed into the sample, indicating that STM measurements are impossible within this voltage regime. Thus, in contrast to previous STM measurements on boron-doped diamond samples, the samples studied here represent a truly insulating diamond substrate.

Surface structure on the atomic scale

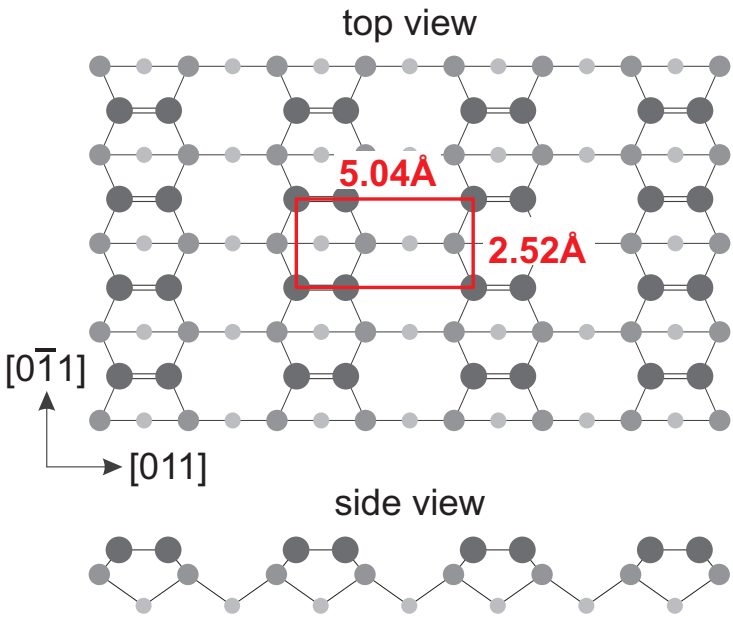

Figure 7.7: Model of the reconstructed diamond C(100)-(2 × 1) structure. The red box represents a surface unit cell.

As a result of hydrogen desorption, the topmost carbon atoms are

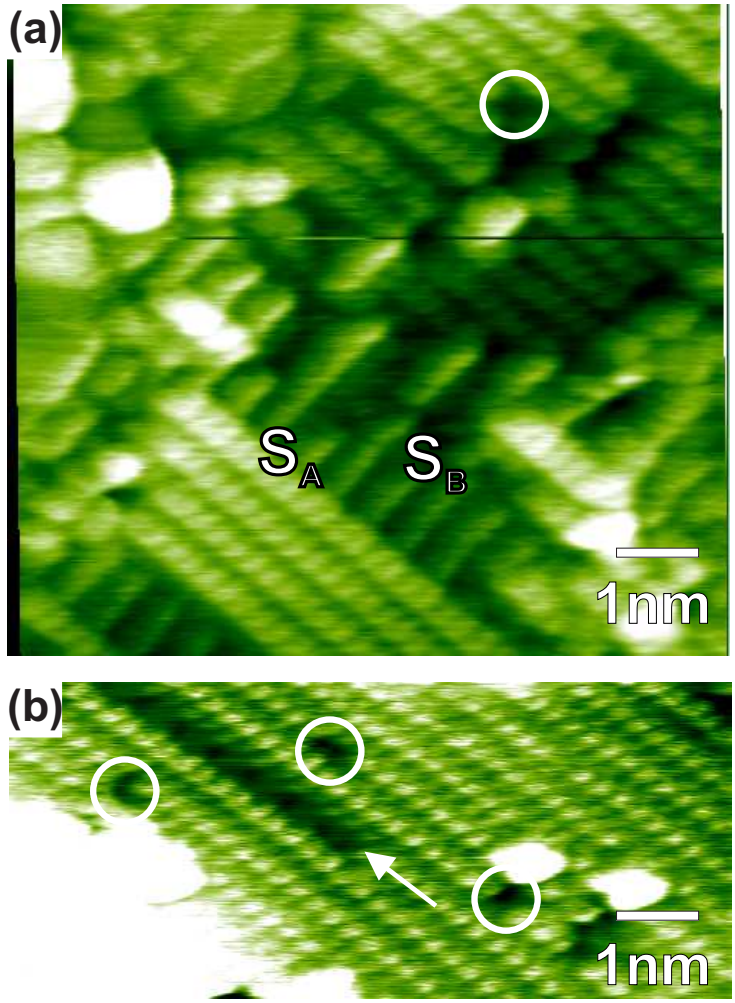

Figure 7.8: NC-AFM topography images of the clean diamond C(100)-(2 × 1) surface (drift corrected raw data). (a) and (b) have been obtained at different measurement sessions, using different tips.

left with one dangling bond each. For stability reasons, the surface reconstructs to double-bonded carbon dimers, as is depicted in Fig. 7.7. NC-AFM topography images of the hydrogen-free surface are shown in Fig. 7.8(a) and (b). Besides drift correction, no further data processing was applied. Fig. 7.8(a) displays terraces consisting of dimer rows. The dimers show a change in orientation of 90° between successive layers due to the crystal structure of diamond (see Chap. 4). The dimer-dimer distance

within a row was measured to be $a' = 2.50 \pm 0.05$ Å, the row distance to be $b' = 5.10 \pm 0.08$ Å. These distances are in good agreement with the unit cell dimensions ($a' = 2.52$ Å, $b' = 5.04$ Å) of a (2 × 1) reconstruction, considering experimentally obtained bulk lattice dimensions [116].

As can be seen at first glance, C(100)-(2 × 1) surface differs significantly from the C(100)-(2 × 1):H surface when imaged with NC-AFM. In contrast to the hydrogen-terminated surface, single surface atoms can only be seen faintly due to a comparably strong interaction of the dimer double bonds with the tip, which superimposes the force exerted to the tip by individual dimer atoms.

Interestingly, this high-resolution NC-AFM contrast obtained on truly insulating diamond is very similar to the one achieved by STM on boron-doped and therefore conducting diamond. It can therefore be concluded that boron-doping, at least to the degree that allows for diamond to become semiconducting, does not significantly alter the diamonds surface structure. In contrast to the STM study from Bobrov *et al.* [87], however, which is the only STM study on insulating diamond to date, the resolution achieved with NC-AFM is superior in the sense that single dimers are resolved, while the STM can only offer resolution down to single rows of dimers.

Surface characteristics

High-resolution NC-AFM images allow for the identification and analysis of surface features such as atomic defects, step edges or anti-phase boundaries. This is done in the following.

Terrace size and structure

As can be seen in Fig. 7.9, the majority of terraces consists of only a few dimer rows, the resulting terrace areas are therefore usually less than 100 nm^2 in size. The rectangular surface unit cell is reflected in the square-cut terrace shape. Terraces are not

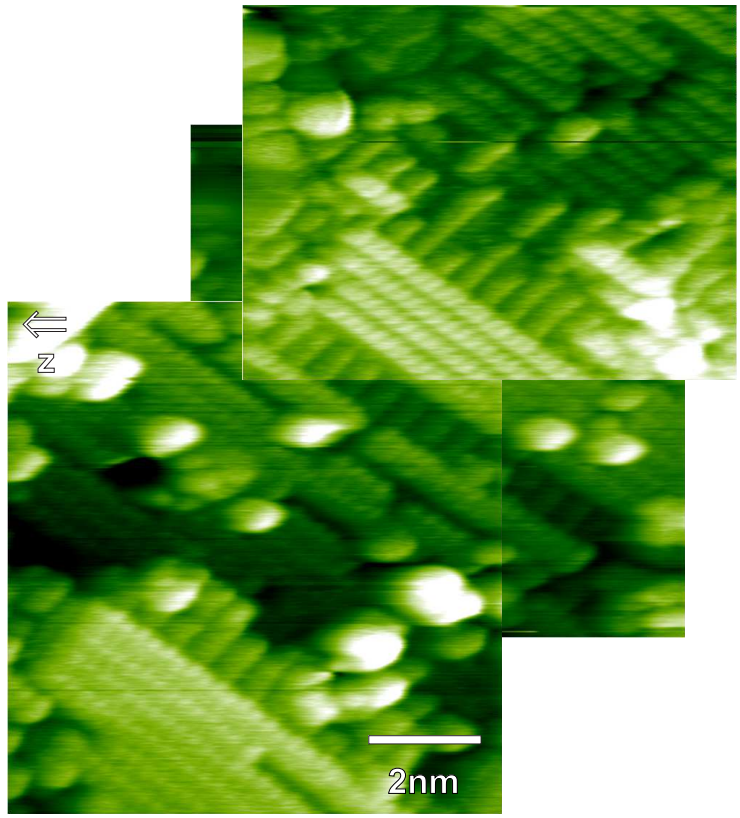

Figure 7.9: Stitched NC-AFM topography image of the clean diamond (100)-(2 × 1) surface.

always closed, but often intersected and incomplete, as can also be taken fromFig. 7.9. The hydrogen-free diamond C(100)-(2 × 1) surface is highly reactive because of the exposed double bonds linking the topmost carbon atoms to dimers. Consequently, adsorbates from the residual gas begin to attach to the surface immediately after removal of the hydrogen layer. These impurities obviously appear in in the NC-AFM images as well (see for example Fig. 7.8 and Fig. 7.9) and significantly hamper close distance raster scanning. Annealing, even close to the temperature of phase transition into graphite (1700K), proved not to be sufficient to clean the surface, which is a clear sign for the adsorbates being chemisorbed to the surface. Due to the extraordinary high Debye temperature of diamond (2200 K)[120], sample annealing is also not suitable to rearrange step edges or to increase the aver-

age terrace width.

Two different kinds of step edges are observed, namely those aligned parallel to the direction of the dimer rows on the upper terrace (S_A [121]) and those aligned perpendicular to the dimer rows (S_B), respectively. An example for each of the step types is marked in Fig. 7.8. In addition to those simple step riser, double steps were also reported in literature for the diamond surface, consequently labeled D_A and D_B [103]. In our measurements, however, single steps were observed exclusively.

Figure 7.10: NC-AFM topography image of an anti-phase boundary perpendicular to the dimer rows.

Occasionally, anti-phase boundaries can be found, stretching across a terrace perpendicular to the dimer rows (see Fig. 7.10). The row dislocation between the two phases always amounts to about 2.5 Å, which is exactly half the row distance.

Vacancies and defects

The types of defects most commonly found on all (100) oriented surfaces of IUPAC group 14 elements (such as Si, Ge, etc.) are either missing dimers or adsorbed species. In the case of diamond, this would most likely be H, O, or CH_x [94]. Due to the atomic resolution provided by the NC-AFM images, single dimer vacancies could be observed (see Fig. 7.8). The defect density is comparable to the one observed on boron-doped diamond via STM, it is therefore reasonable to assume that boron doping in the order to achieve semiconductivity does not significantly influence the number of defects on the diamond surface.

In addition to defects where a single dimer is missing, multiple

dimer vacancies (Fig. 7.8) as well as complete missing rows (Fig. 7.9) are also observed. Those line defects are typical for the diamond surface because of the increased surface anisotropy driven by the differing stability of the two types of step risers [94,122].

7.5 Obstacles

NC-AFM measurements on diamond surfaces are afflicted with various difficulties that pose an experimental challenge.

In case of the hydrogen-terminated diamond C(100)-(2 × 1):H surface, its inert nature may offer the benefit of a low adsorbate density and allows for *ex-situ* sample handling. But on the other hand, this also means that there is only weak interaction between individual surface atoms and the scanning probe tip. Hence, scanning very close to the surface (high frequency shift setpoint in combination with little height feedback regulation) is mandatory to achieve atomic resolution. Since the surface itself is strongly fissured and characterized by a small average terrace size, however, scanning in the aforementioned manner often results in accidental physical contact of the tip with the surface. On most ionic surfaces, these kind of tip-surface crashes do often not afflict significant damage to the tip because the tip material (Si) is harder and less brittle than the surface. On comparably soft substrates, such as $CaCO_3$ or NaCl, the tip may pick up fragments of the surface as a result of the crash, but often stays largely intact itself. In some cases, tips terminated by picked-up surface fragments even offer enhanced resolution compared to the freshly prepared tip. Regarding diamond surfaces, on the other hand, the extraordinary hardness of the substrate usually results in immediate and irreversible blunting of the tip upon contact. Since true atomic resolution can only be achieved in NC-AFM when the tip apex is at least as small as the interatomic distances, very sharp tips are required. Hence, even a single physical contact of tip and sample may prove fatal to the atomic resolution capabilities of a tip. Moreover, the hydrogen atoms attached to the topmost carbon are subject to negligible steric repulsion[117]. They can therefore give way to some degree when a repulsive force is acting on them, for example by an NC-AFM tip. This is reflected in the NC-AFM images as blurring on the atomic scale.

On the pure diamond C(100)-(2 × 1) surface, the interaction between tip and surface is in general much stronger due to the absence of the inert hydrogen layer. Consequently, it is easier to

obtain atomic resolution NC-AFM images of the bare diamond surface compared to the hydrogen-terminated surface. The basic problems described above, however, still persist. Terrace size and structure remain unchanged compared to the hydrogen-terminated surface and tip-surface crashes also have the same severe effect on tip quality. In addition, even the freshly prepared bare diamond C(100)-(2 × 1) surface features a comparatively high impurity density due to its high sticking coefficient, which further impedes close distance raster scanning. Because of the surface reactivity, there is also only a small time frame after removal of the hydrogen layer in which the C(100)-(2 × 1) surface is clean enough to allow for high-resolution raster scanning even when kept under UHV conditions.

7.6 Conclusions

In conclusion, high-resolution NC-AFM images of both, hydrogenated and clean, high-purity diamond (100) surfaces were presented. In contrast to previously obtained STM images, both hydrogen atoms in the unit cell of the C(100)-(2 × 1):H surface were resolved individually. The NC-AFM images also reveal, for the first time, atomic-resolution contrast on the clean, insulating diamond surface and provide real-space experimental evidence for a (2 × 1) surface reconstruction. This opens interesting new perspectives for atomic-scale studies of molecular grafting and self-assembly, as is endeavored in the following chapter. The much improved atomic-scale resolution of the NC-AFM, compared to the STM, confirms that NC-AFM is a unique probe of atomic-scale adsorbate and surface structures.

8 NC-AFM study of C_{60} adsorption on the diamond C(100) surface

Contents

As was shown in the previous chapter, NC-AFM allows for high resolution imaging of both the hydrogen-terminated diamond C(100)-(2 × 1):H and the pure C(100)-(2 × 1) surface. This offers the possibility to also study in detail the adsorption and self-assembly potential of different molecular species on those sur-

faces. Regarding diamond surfaces, the interaction with fullerenes is of particular interest from a scientific as well as from an application-oriented point of view. Consequently, the adsorption of two types of fullerenes, namely C_{60} and $C_{60}F_{48}$, was studied in the framework of this thesis and the results are presented in the following.

8.1 Motivation

The study of the adsorption behavior of C_{60} fullerenes on diamond surfaces is of major interest with regards to the implementation of a molecular quantum computer as introduced in Chap. 4. The concept demands linear chains consisting of single fullerenes aligned in well-defined distances on the diamond surface.

From the experimental point of view, there are basically two different bottom-up approaches to build those molecular chains. The most elegant method is to make use of molecular self-assembly and, if necessary, manipulate the surface in such a way that the fullerenes align in the desired formation by themselves. An alternative approach is the external manipulation of single fullerenes into the desired position, for example using an NC-AFM tip. In both cases, however, detailed knowledge of the molecular adsorption characteristics is a basic prerequisite. In order for the molecules to self-assemble in the desired form, for example, molecular diffusion must be possible, which is not the case when the molecules strongly chemisorb to the surface. When the molecule-surface interaction is too weak, on the other hand, the molecules may simply desorb or diffuse across the surface without building stable structures. As will be shown in the following, the fundamental chemical differences between the pure and the hydrogen-terminated diamond surface results in a complete different adsorption behavior of C_{60} fullerenes, which might be exploited with regards to the objectives described above.

8.2 Experimental setup

Both, diamond sample preparation and NC-AFM setup, are as already described in Chap. 7. Prior to C_{60} deposition, the diamond samples were imaged with NC-AFM to analyze the structure on the atomic scale and the purity of the diamond surface. As observed before, some protrusions cannot be removed by means of thermal desorption. Those surface features are likely to be nanodiamonds or adsorbates covalently bound to hydrogen-free surface areas.

The C_{60} fullerenes (MER Corporation, Tuscon, Arizona; purity of 99.95%) were deposited onto the surface under UHV conditions by sublimation from a Knudsen cell held at a temperature of about 650 K. This cell temperature corresponds to a flux of approximately $0.01\,\mathrm{ML\,s^{-1}}$ as measured with a QCM (Inficon IC5 controller). During the deposition process, the substrate was kept at RT. The samples were transferred into the AFM situated in the same UHV system immediately after deposition. Any subsequent annealing of the samples was done in the same UHV system. The annealing temperature was measured using a thermocouple mounted at the sample stage about 2.5 cm away from the sample. The temperature specifications given in this work correspond to temperatures expected at the diamond sample based on an individual calibration curve supplied by the manufacturer (Omicron, Taunusstein, Germany).

8.3 C_{60} on hydrogen-terminated diamond C(100)-(2 × 1):H

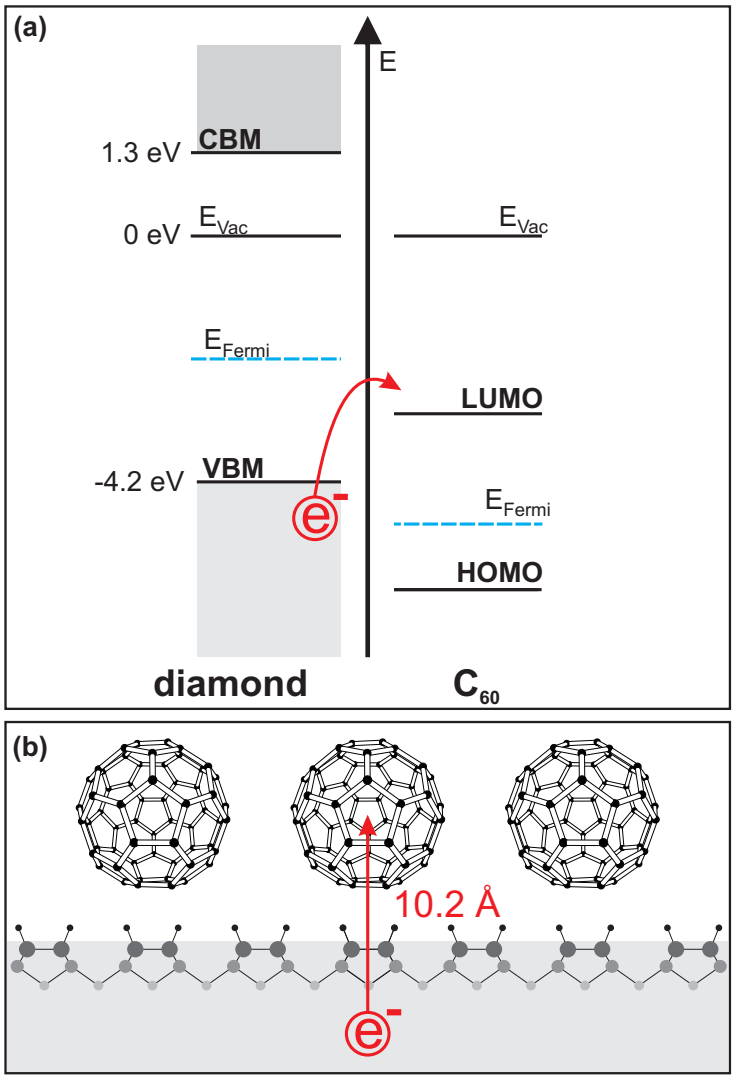

Figure 8.1: (a) Electronic levels of diamond (left) and C_{60} (right), illustrating the electron transfer from the diamond VBM to the LUMO in C_{60}. (b) Spacial charge separation after electron transfer from diamond to C_{60} results in a distance of 10.2Å as calculated by Sque *et al.* [43].

As already explained in Chap. 4, the interaction of molecules that have a large electron affinity, for example C_{60} fullerenes,

with the hydrogenated diamond surface is influenced by an effect known as **transfer doping**. According to this model, electrons from the diamond valence band can transfer into molecules adsorbed on the surface, leaving a hole behind within the surface layer (see Fig. 8.1) Inspired by this finding, efforts have been made to study the adsorption of fullerenes on hydrogenated diamond surfaces in more detail [123,124]. However, no study exists so far addressing the consequences of charge transfer doping on the C_{60} island morphologies on hydrogenated diamond. The NC-AFM study presented in the following contains the first real-space images of the C_{60} assembly on this surface and therefore allows to evaluate the influence of transfer doping on structure formation.

As-deposited island structure

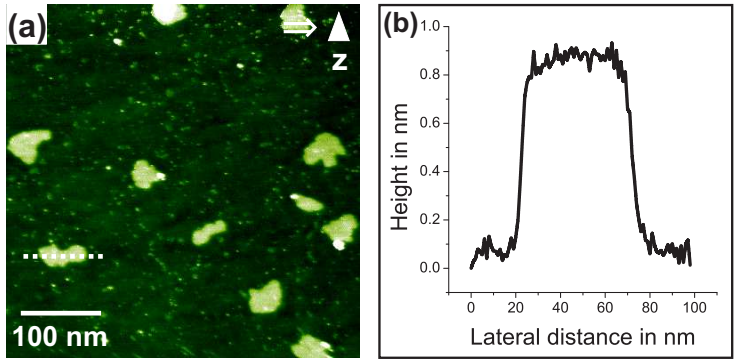

Figure 8.2: Topography NC-AFM image showing C_{60} fullerene islands on C(100)-(2 × 1):H. (a) Overview of the as-deposited structure at RT after depositing 0.07 ML of C_{60}. (b) Height profile as indicated by the dashed line in (a), revealing a height of approximately 0.9 nm corresponding to a single layer of C_{60}.

Upon deposition of approximately 0.07 ML C_{60} onto a sample held at RT, islands are formed having a typical size of several tens of nanometers in diameter. Fig. 8.2(a) shows a representative NC-AFM image of the as-deposited situation at RT. The average area of these islands corresponds to approximately 700 nm^2. The formation of these islands demonstrates that the diffusion barrier is overcome at RT. As can be seen from the height profile shown in Fig. 8.2(b), the prevalent height of the islands is 0.9±0.1 nm, corresponding to single-layer C_{60} islands.

The molecular islands do not exhibit a clear hexagonal or trig-

onal shape as observed on other dielectric substrates [110,125,126]. Instead, a statistical analysis of island edges reveals two preferred directions. These two directions coincide with the [011] and [0$\bar{1}$1] directions of the C(100)-(2 × 1):H surface. This finding demonstrates the structural influence of the underlying C(100)-(2 × 1):H substrate on the preferred orientations of the C_{60} islands.

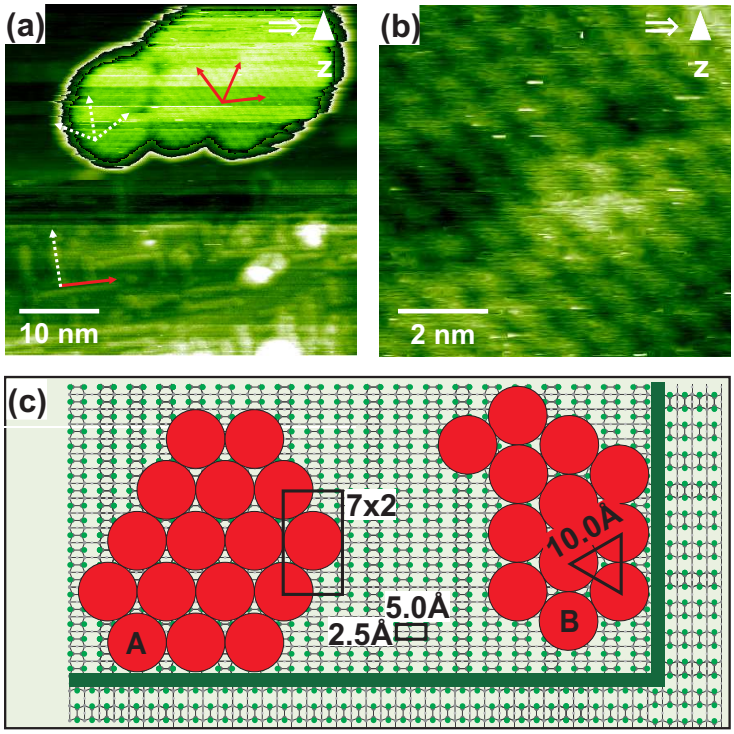

Figure 8.3: Topography NC-AFM image showing the C_{60} orientation in relation to the C(100)-(2 × 1):H surface directions, which are pointed out by the red/white pair of arrows in the lower left corner. The island consists of two domains rotated by 30°, as indicated by the red and the white arrows. (b) Drift-corrected topography NC-AFM image showing individual C_{60} fullerenes aligning in a nearly hexagonal close-packed arrangement. (c) Model of the two domains.

Repeated scanning over single-layer islands readily results in the formation of double-layer structures, indicating that the single-layer islands represent a thermodynamically unstable configuration. A detailed view of such a double-layer island is shown in Fig. 8.3(a). The internal structure of the islands is hexagonal close-packed, as can be seen in Fig. 8.3(b). Due to the geometrical difference of the hexagonal C_{60} bulk structure with the rectangular surface structure, two island domains emerge, rotated by 30°. Occasionally, these two domains are apparent

even within one single island, as shown in the island given in Fig. 8.3(a). Here, the structure of the underlying substrate is resolved together with the internal structure of the C_{60} island.

After correcting the image for thermal drift, the rotation of the two domains was determined to $30.4° \pm 2.9°$, which is in good agreement with the model shown in Fig. 8.3(c). This model is based on arranging a hexagonal lattice with lattice periodicity of 10.0 Å,onto the rectangular lattice of the C(100)-(2×1):H surface with dimensions of a =2.52 Å and b =5.04 Å. A nearly hexagonal arrangement of the C_{60} molecules can be achieved by forming a c(7×2) superstructure (domain A). However, as already pointed out in Chap. 7, the terraces on the substrate are usually smaller than the typical island size. Thus, the C_{60} islands extend on adjacent terraces, where the substrate directions are rotated by 90°. This results in a second domain (domain B) and readily explains the existence of two domains rotated by 30° as observed in the experiment. Interestingly, the geometrical match of domain B with the underlying substrate is not as good as it is for domain A, indicating that the intermolecular interactions are decisive for the resulting molecular arrangement.

Island structure after annealing

A prominent change is observed upon annealing the C_{60} covered sample to a temperature of approximately 505 K. As can be seen in Fig. 8.4(a), the islands have grown in size, now extending over more than 12 000 nm^2 in area. At the same time, the number of islands is drastically decreased. As before, the observed internal structure is hexagonal (Fig. 8.4(b)). Moreover, the islands exhibit a height of approximately 1.9 nm, as can be seen from the height profile given in Fig. 8.4(c), corresponding to two layers of C_{60}. Thus, a clear transition is observed from small single-layer islands to an extended wetting film with a height of two layers.

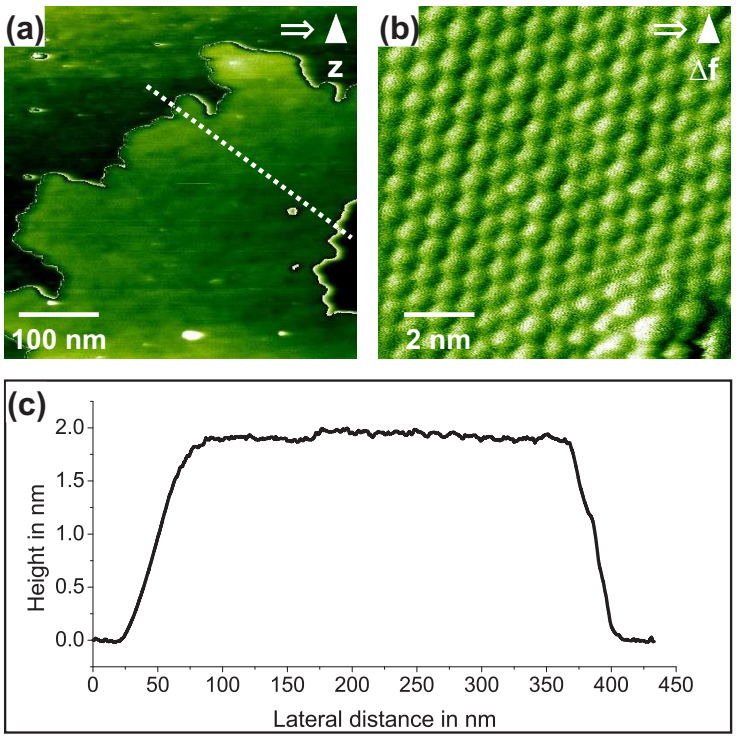

Figure 8.4: Topography NC-AFM images showing a C_{60} fullerene island on C(100)-(2 × 1):H after annealing. (a) Island formed after annealing a sample covered with 0.07 ML C_{60} to approximately 505 K. (b) High-resolution image revealing the hexagonally packed inner structure. (c) Line profile as indicated in (a) revealing an island height of approximately 1.9 nm, corresponding to two layers of C_{60}.

Complete desorption

To further characterize the interaction between the molecular film and the underlying substrate, the temperature above which complete desorption occurred was determined. Complete desorption is achieved by annealing the substrate to a temperature in the range of 573 K to 653 K. This finding corresponds well with previous high-resolution electron energy loss spectroscopy (HREELS) results, reporting multilayer desorption at temperatures of 473 K, while complete desorption has been achieved at 573 K[124]. A rough estimate can be obtained for the desorption enthalpy using Redhead's formula for the desorption en-

thalpy[127]

$$E_{\mathrm{des}} = T_{\mathrm{des}} \cdot k_B \left\{ \ln\left(\frac{\nu \cdot T_{\mathrm{des}}}{\beta} \right) - 3.64 \right\} \tag{8.1}$$

where E_{des}, T_{des}, k_B, ν and β are the desorption enthalpy, the corresponding desorption temperature, the Boltzmann constant, the attempt frequency and the heating rate. A value of E_{des} = 1.7±0.1 eV is obtained for an average desorption temperature of 613 K, when using an attempt frequency of $\nu = 10^{13}\,\mathrm{s}^{-1}$ and a heating rate of $\beta = 2\,\mathrm{K\,s}^{-1}$.

Interestingly, the desorption enthalpy is slightly larger than the sublimation enthalpy of crystalline C_{60}, around 1.65 eV[40], which explains why multilayer desorption occurs at temperatures below complete desorption[124]. In other words, the binding energy of C_{60} to the hydrogenated diamond surface is larger than the binding of C_{60} molecules among each other in a solid crystal. This finding is in agreement with the fact that an extended wetting layer is found after moderate annealing. However, when considering the chemically inert nature of the hydrogenated diamond surface, the comparatively high interaction energy appears surprising.

Effect of transfer doping

In order to explain the unexpected high binding energy of the double-layer films, the influence of charge transfer doping on the binding energy of the double-layer film needs to be discussed.

As single-layer islands are found to dewet at approximately 505 K, a rough estimate of the binding energy of single-layer C_{60} molecules to the hydrogenated diamond surface can be given, being in the order of 1.4 eV. This value can be compared to the desorption temperature of C_{60} from the hydrogenated silicon surface, Si(100)-(2 × 1):H. While this surface is chemically very similar to hydrogenated diamond, there is one important difference:

the absence of charge transfer doping. Sanvitto *et al.* have measured a desorption temperature of C_{60} fullerenes from the Si(100)-(2 × 1):H surface of approximately 503 K,[128] corresponding to a desorption enthalpy of 1.3 eV. This desorption enthalpy agrees with Van-der-Waals bound physisorbed C_{60} molecules. However, this value is considerably smaller than that measured for the desorption enthalpy of the double-layer films on hydrogenated diamond, namely 1.7 eV. Thus, an additional effect in the order of 0.3 eV to 0.4 eV is expected to arise from the fact that charge transfer doping is possible on hydrogenated diamond.

Transfer doping has been demonstrated to be considerably smaller for single-layer films than for higher coverages[44]. This finding has been explained by the fact that electrostatic repulsion is more pronounced in single-layer films, hindering an efficient electron transfer. For double-layer films, in contrast, many-body effects reduce electron-electron repulsion and facilitate electron transfer. This is expressed in an effective increase in the electron affinity when comparing single-layer films with bulk C_{60}, as has been shown in Ref.[44]. Thus, a significant contribution of transfer doping is expected for the double-layer films, but not for the single layer films, nicely explaining why the single-layer film dewets, while the double-layer film wets the surface.

As a simple estimate for the contribution of charge transfer doping to the binding energy of the double layer to the substrate, the electrostatic interaction arising from the spatial separation of electrons and holes can be used. Based on calculations by Sque *et al.*,[43] the spatial separation of electron and hole amounts to 10.2 Å upon adsorption of a C_{60} fullerene onto the C(100)(2x1):H surface. Taking this value literally, the Coulomb attraction can be estimated, amounting to 1.4 eV per transferred electron. To arrive at a meaningful estimate for the contribution of transfer doping to the binding energy, the doping efficiency (surface hole density in diamond divided by C_{60} coverage) has to be considered. The doping efficiency can be estimated to be as low as 10^{-2} to 10^{-3} [44]. This estimate has, however, been calculated based solely on the measured surface conductance of the samples. Consequently, the obtained value is valid only when no immobile charge carriers exist that contribute to the doping process but not to the conductivity. As a large number of immobile charge

carriers are likely to be present, the true doping efficiency might be considerably higher. Based on the very simple estimate made above, we obtain a doping efficiency in the order of 0.2 to 0.3. Given the simplicity of the picture drawn here for estimating the contribution of the charge transfer doping to the binding energy of a double-layer C_{60} film, the agreement of the energy ranges is surprisingly good. It has to be kept in mind, however, that this calculation can only provide an estimate, but no definite *quantitative* description of the contribution of charge transfer doping to the overall binding energy. The *qualitative* description of this contribution, on the other hand, manifests itself in a peculiar transition from a dewetting to a wetting molecular layer and is therefore evident in the NC-AFM images.

Island manipulation

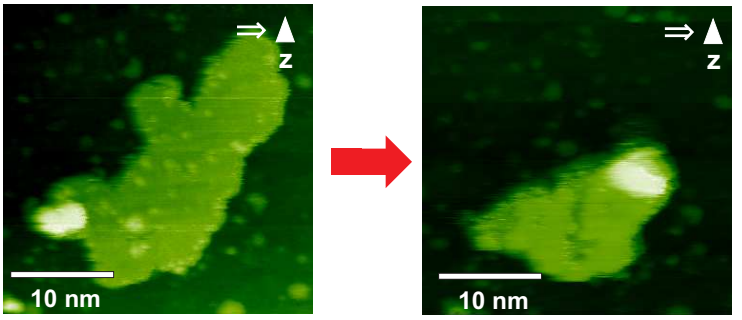

Figure 8.5: NC-AFM topography image showing an example of tip-induced island growth of a kind of "layer-by-layer" type. On the left hand side, the original single-layer island is displayed, with the second layer beginning to grow in the bottom-left corner. On the right hand side, the same island is displayed after extensive manipulation, now featuring a closed double-layer and a beginning third layer in the upper-right corner.

As already mentioned, not only annealing of the sample, but also repeated scanning over single-layer islands at RT constitutes a possibility to manipulate the C_{60} formation on the surface and thereby change the morphology of fullerene islands. In particular, the NC-AFM tip can be used to facilitate local dewetting, as will be shown in the following. Two examples for this way of island manipulation are displayed in Fig. 8.5 and Fig. 8.6. As can be seen from the two figures, two different types of tip-induced island growth have been observed. In both cases, the energy necessary to overcome the dewetting barrier is provided by the dissipated energy of the tip oscillation.

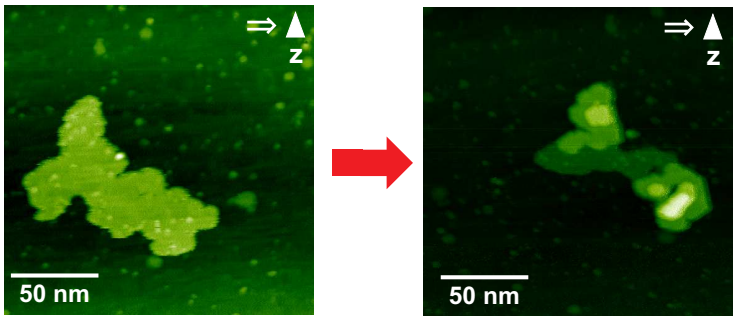

Figure 8.6: NC-AFM topography image showing an example of tip-induced island growth of a kind of "layer-plus-islands" type. On the left hand side, the original single-layer island is displayed. On the right hand side, the same island is displayed after extensive manipulation, now featuring two stacks of C_{60} fullerenes up to the 4^{th} layer.

In the first mode, which is depicted in every iteration in Fig. 8.7, a third layer does not begin to emerge before the second layer is complete. Therefore, the tip induced island growth mode of a kind of "layer-by-layer" in this case. The second layer has only one starting point, namely in the lower left hand corner of the island. The double layer then develops from this location. Remarkably, the overall island structure is much less branched after the transformation from single-layer to double-layer. This can be explained by the structural mismatch between the hexagonal C_{60} bulk structure and the underlying C(100)-(2 × 1):H surface, which naturally is less influential on structure formation the higher the layer. Consequently, a more bulk-like arrangement of C_{60} molecules emerges in the second layer, which is apparent in the more closed appearance of the double-layer islands.

Another characteristic of the tip-induced island growth is the fact that the second layer does not necessarily grow from the position were the first layer dissolves, as can be nicely seen in Fig. 8.7. Therefore, C_{60} diffusion must be possible on the second layer (C_{60}-C_{60} diffusion barrier: $E_{diff}^{C_{60}} = 0.214\,eV$ [101]), resulting in a molecular flow from the spot where the transition of a fullerene to the second layer happens towards the edge of the second layer, which offers an energetically favorable position for the fullerene molecule to settle due to the stabilizing influence of neighboring molecules.

The area growth of the second layer on expense of the first layer is depicted in Fig. 8.8. As can be seen, the growth appears to be

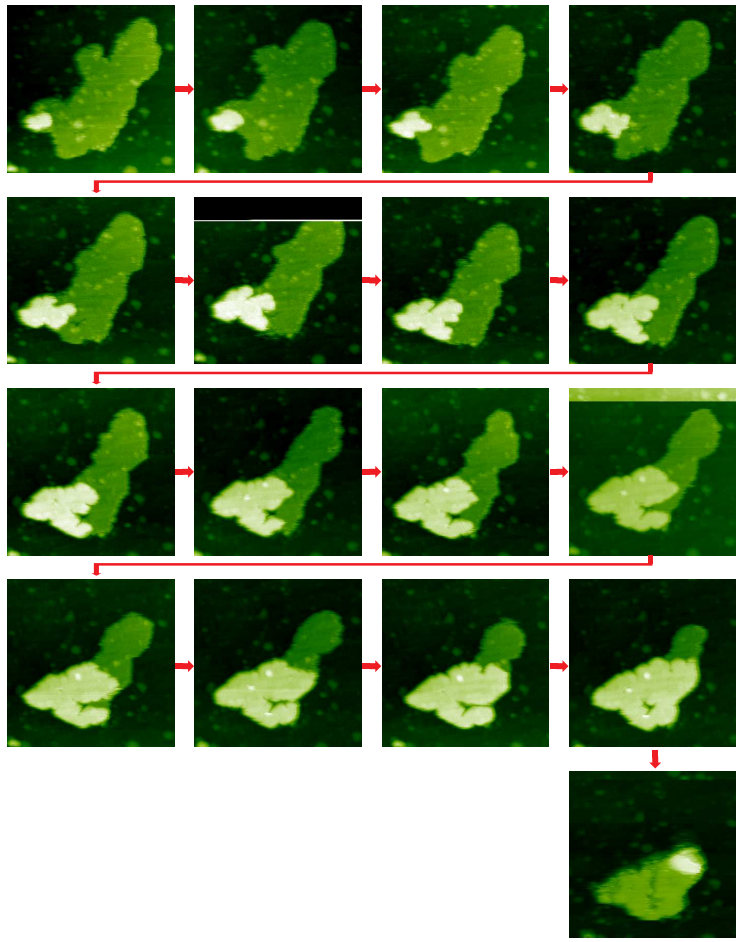

Figure 8.7: NC-AFM topography images (30 nm×30 nm) showing tip-induced island growth of a kind of "layer-by-layer" type.

a linear process. Taking into account scan speed and image size (1 ms/point, 500×500 image points), the growth velocity of the second layer can be calculated to $0.28\pm0.01\,\mathrm{nm^2\,s^{-1}}$, which corresponds to the transition of one C_{60} molecule about every three seconds. Since the growth is induced by energy dissipation from the tip, it should be possible to steer the growth by changing scanning parameters such as detuning setpoint, distance feedback loop and scan speed. Indeed, scanning of another island with the same tip as in Fig. 8.5 but with smaller frequency shift due to a larger tip-surface distance and with more faster dis-

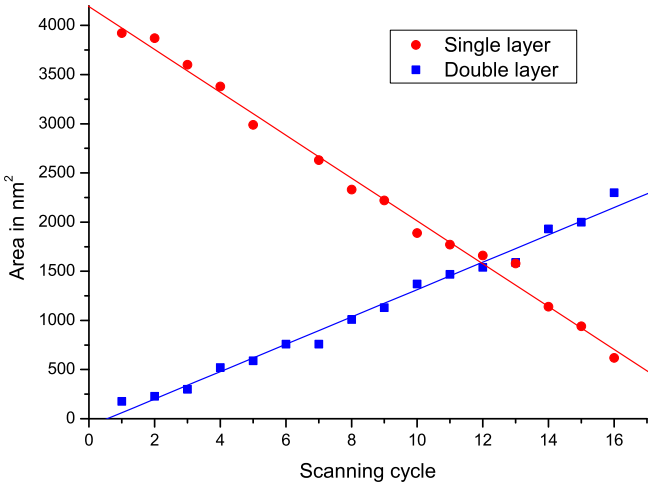

Figure 8.8: Increase of the double-layer area on expense of the single-layer area of the island depicted in Fig. 8.7 as a result of scanning the island.

tance feedback regulation results in a kind of "layer-plus-island" type of growth as depicted in Fig. 8.6. Here, higher layers are formed before lower layers are closed. While the second layer growth begins at the edge of the island (albeit in two separate locations), higher layers always start to emerge roughly in the center of the next lower layer and never at island edges.

Again, the effect of transfer doping offers an explanation for the observed growth in height of the C_{60} islands. As was mentioned before, the contribution of transfer doping to the overall binding energy increases with the height of the C_{60} adlayer[44]. Thus, vertical stacking of fullerenes on the C(100)-(2 × 1):H surface is generally favored by this effect. However, in order to overcome the dewetting barrier, which can be treated as the activation energy necessary for a molecule to make the transition to the next higher layer, an (external) energy input is necessary. This energy input can be provided either by thermal annealing or by making use of dissipating energy from the AFM tip oscillation.

Conclusions

C_{60} fullerenes deposited onto the hydrogenated diamond C(100)-(2×1):H surface reveal a peculiar transition from dewetting single-layer to wetting double-layer films. After deposition at RT, islands are observed with an average area of about 700 nm^2. Upon annealing the substrate to 505 K, the dewetting barrier is overcome, indicating a rather weak interaction of C_{60} molecules from the single layer with the underlying substrate, which can be roughly estimated to 1.4 eV. In contrast to this finding, the resulting two-layer high islands form a wetting film, extending over more than 12000 nm^2 in area. These extended films indicate a rather strong interaction with the substrate, which is estimated to 1.7 eV. This considerable increase in interaction energy can be understood by considering the influence of charge transfer doping on the binding energy. Charge transfer doping is greatly reduced for single-layer films, but becomes significant in the case of double-layer films. A simple model considering electrostatic attraction accounts for approximately 1.4 eV of interaction energy in addition to simple van-der-Waals attraction. This model explains the unexpected high interaction energy in the case of double-layer films and provides an explanation for the transition from a dewetting single-layer to a wetting double-layer structure as well as the possibility to stack-up C_{60} islands using an NC-AFM tip.

8.4 C_{60} on pure diamond C(100)-(2 × 1)

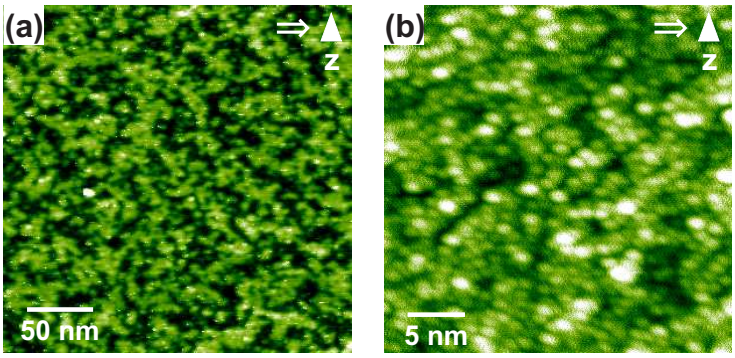

Figure 8.9: NC-AFM topography images showing the adsorption of C_{60} on the pure C(100)-(2 × 1) surface. (a) Large-scale overview displaying irregular clusters, (b) zoom into the structure revealing single molecules.

Bare diamond C(100)-(2 × 1) surfaces were prepared by annealing the hydrogenated surface beyond 505 K for 1 h as described in Chap. 7. Afterwards, C_{60} was sublimated onto the surface, aiming for a similar coverage as before on the hydrogenated samples. An NC-AFM image of the so prepared sample is shown in Fig. 8.9. As can be seen, the C_{60} does not form islands on the bare surface, but instead sticks to the surface in what appears to be random order. The coverage exceeds 1 ML and is therefore significantly higher than what was expected based on the adsorption on the hydrogenated surface. It can therefore be said that the sticking coefficient of the bare diamond surface is much higher than that of the hydrogenated surface. In-situ annealing up to 1700 K, close to the graphite transition temperature, did not result in a desorption of the fullerenes. Using Redhead's formula, we can state that therefore the desorption enthalpy must be higher than 4.4 eV. *Ex-situ* ultrasonic cleaning in toluene, which is known to be a fairly good C_{60} solvent[129], did not remove the C_{60} adlayer either. This finding strongly indicates that the C_{60} is bound covalently to the diamond surface. This is due to the fact that the diamond surface exhibits one unsaturated π-bond per dimer, which is very likely to react with the large conjugated system of the C_{60} fullerene, resulting in a strong covalent binding. A very similar reaction was observed before for the C_{60} adsorption on Si(100)-(2 × 1), which is structurally akin to the C(100)-(2 × 1) surface[130].

8.5 $C_{60}F_{48}$ on hydrogen-terminated diamond C(100)-(2 × 1):H

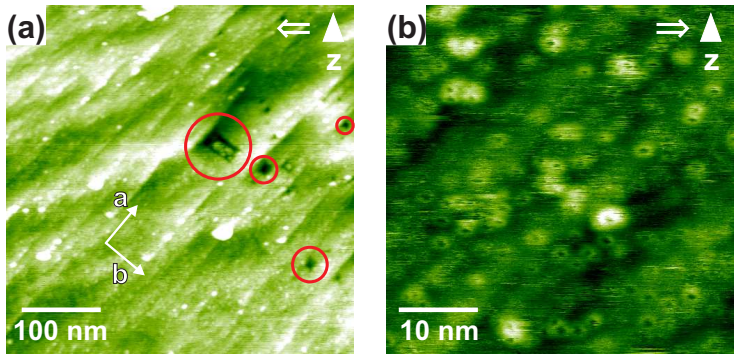

Figure 8.10: NC-AFM topography images showing the adsorption of $C_{60}F_{48}$ on the hydrogen-terminated C(100)-(2 × 1):H surface. (a) Large scale overview with rectangular bare patches encircled in red, (b) small-scale zoom into the structure.

In order to further evaluate the influence of transfer doping on fullerene self-assembly, $C_{60}F_{48}$ adsorption on the C(100)-(2×1):H surface was studied. $C_{60}F_{48}$ has an even larger electron affinity than C_{60} (4.06 eV[48] compared to 2.7 eV[42]) and is therefore expected to reach a doping efficiency close to one transfered electron per fullerene[49]. In addition, the intermolecular binding in the $C_{60}F_{48}$ solid is much weaker compared to solid C_{60}, which is reflected in a much lower sublimation enthalpy of the former (1.13 eV[47] compared to 1.65 eV[40]). Consequently, one would expect a significantly increased influence of the substrate on molecular self-assembly upon deposition on the hydrogenated diamond surface in case of $C_{60}F_{48}$ compared to C_{60}.

Due to the decreased sublimation enthalpy upon fluorination of C_{60}, the sublimation temperature necessary to deposit $C_{60}F_{48}$ onto the C(100)-(2 × 1):H surface from a Knudsen cell was found to be much lower as well, amounting to 393 K. This corresponds to a flux of approximately 2×10^{-4} ML s^{-1} as measured with a QCM. The smaller flux compared to the deposition of C_{60} was deliberately chosen because of the more fragile nature of $C_{60}F_{48}$, which is thermally much less stable than C_{60}.

NC-AFM images of the C(100)-(2 × 1):H surface after deposition of $C_{60}F_{48}$ (provided by Dr. *name removed for privacy* from the Jožef Stefan Institute in Ljubljana, Slovenia; purity of > 96 %)

can be seen in Fig. 8.10. Fig. 8.10(a) shows a large-scale overview image of the surface, while Fig. 8.10(b) displays a surface area small enough to identify single molecules. Although the amount deposited corresponds to less than half a monolayer as determined with the QCM, the surface is well covered with molecules. The sticking coefficient thus turned out to be significantly higher than expected from the QCM data. This already indicates a rather strong binding between molecules and substrate.

As can be seen on first glance, the fullerenes do not self-assemble to islands, but attach to the surface in little order. Hence, it can immediately be concluded that the diffusion barrier cannot be overcome at RT. In general, the adsorption pattern upon $C_{60}F_{48}$ deposition on the *hydrogenated* C(100)-(2 × 1):H surface is similar to the one observed for the adsorption of C_{60} on the *hydrogen-free* C(100)-(2 × 1) surface, with one interesting exception: The existence of small, rectangular surface areas that are apparently omitted by $C_{60}F_{48}$. The directions of those fullerene-free patches, which are marked by red circles in Fig. 8.10, are in agreement with the directions of the diamond unit cell ($[0\bar{1}1]$ and [011]). Their small size and the resemblance of diamond surface directions allows for the interpretation that complete diamond terraces are omitted by $C_{60}F_{48}$ fullerenes upon deposition. Hence, those terraces must be different in the sense that they, in contrast to the rest of the surface, do not allow for the binding of $C_{60}F_{48}$ fullerenes at RT.

Interestingly, the bare patches persist even after annealing of the sample up to 780 K (see Fig. 8.11). However, annealing has an effect on the $C_{60}F_{48}$ formation in the sense that the molecules apparently aggregate to larger cluster. Hence the diffusion barrier must be lower than 2.0 eV, as determined using Redhead's formula.

While the NC-AFM measurements at hand are not sufficient to explain the (chemical) nature of the bare patches, the finding that $C_{60}F_{48}$ shows a completely different adsorption behavior on the C(100)-(2 × 1):H surface than C_{60} is insightful in itself, since there are only two possible reasons for this difference: Either the fluorine atoms of $C_{60}F_{48}$ chemically react with the hydrogen atoms of the surface, or the difference is founded in enhanced

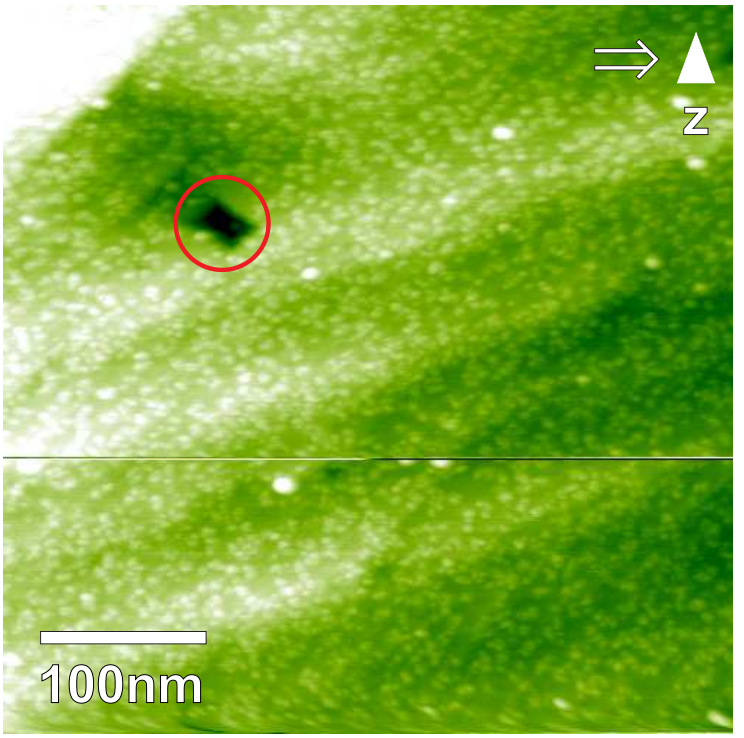

Figure 8.11: NC-AFM topography images showing the adsorption of $C_{60}F_{48}$ on the hydrogen-terminated C(100)-(2 × 1):H surface after annealing at 780 K. The red circle marks an bare patch.

transfer doping. The letter would certainly result in a stronger binding to the surface, explaining nicely why the influence of the diamond surface on structure formation dominates over intermolecular forces and no self-assembled islands are observed.

As a result, these findings already hint at the advanced possibilities offered by fluorinated C_{60} derivatives with regards to molecular electronics on hydrogenated diamond surfaces. In order to further evaluate the influence of fluorination on fullerene adsorption, the sublimation of C_{60} derivatives fluorinated to a lesser degree ($C_{60}F_{36}$, $C_{60}F_{18}$) onto the C(100)-(2 × 1):H surface would be highly interesting. If the observed pattern holds true, one would expect a gradual transition from the self-assembled islands emerging upon C_{60} deposition to the largely unordered $C_{60}F_{48}$ structure with increasing fluorination rate.

8.6 Consequences and outlook for the implementation of a molecular quantum computer

Since a major motivation to study fullerene adsorption on diamond surfaces is its utilization for the implementation of a molecular quantum computer as described in Chap. 4, the results obtained using NC-AFM are evaluated in this context in the following.

On the positive side, C_{60} was shown to readily diffuse even over step edges on the C(100)-(2×1):H surface and thereby self-assemble to stable single-layer structures at room temperature. Hence, no cooling of the surface is necessary in order to achieve C_{60} physisorption to the surface, but could be used to hamper diffusion if desired. Unfortunately, the self-assembled structures are two-dimensional islands and not one-dimensional molecular chains as desired in the quantum computer concept. Consequently, ways must be found to steer the fullerenes into a linear alignment. One way to achieve this is the targeted desorption of hydrogen from the surface, leaving behind the pure, very reactive diamond C(100)-(2 × 1) surface. As the NC-AFM results show, C_{60} readily forms covalent bonds to this surface due to a strong interaction with the unsaturated π-bonds of the surface carbon dimers. Consequently, the bare surface could be used to orchestrate anchor points for C_{60} fullerenes in selected positions, while the hydrogenated surface serves as a transport layer to enable C_{60} diffusion towards those designated surface spots. In order to produce strongly localized hydrogen-free spots on an otherwise fully hydrogen-terminated C(100)-(2 × 1):H surface, a strategy to remove the hydrogen is necessary. In this regard, Bobrov *et al.* were already able to achieve some success using STM[122]. In their study, voltage pulse were applied to the surface by an STM tip, resulting in the desorption of individual hydrogen atoms from the C(100)-(2×1):H surface. As a drawback, however, the hydrogen-free spots are randomly scattered in close vicinity (a few nanometers) to the STM tip, as can be seen in Fig. 8.12. Up to now, no successful attempt to further narrow down the dehydrogenated sites has been published. As was shown by different research groups[131,132], it is in principle also possible to use

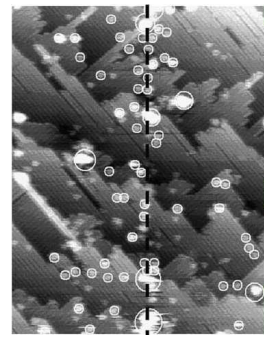

Figure 8.12: STM topography image taken from Bobrov et al. showing the desorption of hydrogen from the hydrogenated diamond C(100)-(2 × 1):H surface[122]. The bright features marked by white circles scattered around the dashed manipulation line represent the dangling bonds after desorption of individual hydrogen atoms.

AFM in order to desorb hydrogen from the C(100) surface by oxidation. In this method, a negative bias voltage is applied to the tip while scanning the surface in air at high humidity (> 60 %), resulting in the formation of an oxygen-terminated surface. The mechanism behind the tip-induced oxidation is not fully understood yet, but the water adlayer present while scanning in air is essential for the process [132]. Hence an application under UHV conditions is not readily possible.

A different approach would be to make use of the strongly fissured, rectangular surface structure of diamond C(100)-(2 × 1):H, which already provides a natural grating. If the C_{60} mobility is decreased to a degree that does not allow for molecular diffusion over step edges any more, for example by liquid nitrogen or helium cooling, the fullerenes might stick to the step edges and self-assemble into linear molecular alignments.

Apart from manipulating the surface or decreasing the C_{60} mobility, the use of C_{60} derivatives may offer enhanced possibilities. As described above, highly fluorinated $C_{60}F_{48}$ shows a much stronger binding to the C(100)-(2 × 1):H surface than C_{60} itself, resulting in strongly reduced self-assembly capabilities. In other words, C_{60} results in the formation of two-dimensional structures on the hydrogen-terminated diamond surface whereas $C_{60}F_{48}$ forms binds in no apparent (so to speak “zero-dimensional”) order to the surface. It is therefore reasonable to assume that the interaction of less fluorinated C_{60} derivatives, such as $C_{60}F_{36}$ or $C_{60}F_{18}$, with the hydrogen-terminated diamond surface will allow for tuning the molecule substrate interaction. Consequently, a suitable C_{60} derivative may result in the formation of the desired one-dimensional alignment.

Finally, it is also conceivable to encapsulate endohedral fullerenes inside carbon nanotubes, thereby creating a so called nanotube peapod [133,134]. Such a peapod offers the great benefit to already host a linear alignment of fullerenes in well-defined intermolecular distances and would therefore allow to elegantly circumvent the challenge to line up the fullerenes in a row.

9 Summary

In this thesis, elemental research towards the implantation of a diamond-based molecular quantum computer is presented. As can be seen in the outline of the quantum computer concept in Chap. 4, the approach followed requires linear alignment of endohedral fullerenes on the diamond C(100) surface in the vicinity of subsurface NV-centers. From this, four fundamental experimental challenges arise:

1. The well-controlled deposition of endohedral fullerenes on a diamond surface.

2. The creation of NV-centers in diamond close to the surface.

3. Preparation and characterization of atomically-flat diamond surfaces.

4. Assembly of linear chains of endohedral fullerenes.

First steps to overcome all these challenges were taken in the framework of this thesis.

In Chap. 5, the so-called “pulse injection” technique was implemented and tested in a UHV chamber that was custom-designed for this and further tasks. Pulse injection in principle allows for the deposition of molecules from solution onto a substrate and can therefore be used to deposit molecular species that are not stable to sublimation under UHV conditions, such as the endohedral fullerenes needed for a quantum register.

Regarding the targeted creation of NV-centers, FIB experiments were carried out in cooperation with the group of Prof. *name removed for privacy* (AG Quantum, Physics Department, Johannes Gutenberg-Universität Mainz). As an entry into this challenging task, argon cations were implanted into (111) surface-oriented CaF_2 crystals. The resulting implantation spots on the surface were imaged and characterized using AFM (Chap. 6). In this context, general relations between the impact of the ions on the surface and their valency or kinetic energy, respectively, could be established.

The main part of this thesis, however, is constituted by NC-AFM studies on both, bare and hydrogen-terminated diamond C(100) surfaces. In cooperation with the group of Prof. *name removed for privacy* (Molecular Nanoscience Group, ISMO, Université de Paris XI), clean and atomically-flat diamond surfaces were prepared by exposure of the substrate to a microwave hydrogen plasma. Subsequently, both surface modifications were imaged in high resolution with NC-AFM (Chap. 7). In the process, both hydrogen atoms in the unit cell of the hydrogenated surface were resolved individually, which was not achieved in previous STM studies of this surface. The NC-AFM images also reveal, for the first time, atomic-resolution contrast on the clean, insulating diamond surface and provide real-space experimental evidence for a (2×1) surface reconstruction.

With regard to the quantum computing concept, high-resolution NC-AFM imaging was also used to study the adsorption and self-assembly potential of two different kinds of fullerenes (C_{60} and $C_{60}F_{48}$) on aforementioned diamond surfaces (Chap. 8). In case of the hydrogenated surface, particular attention was paid to the influence of charge transfer doping on the fullerene-substrate interaction and the morphology emerging from self-assembly. Finally, self-assembled C_{60} islands on the hydrogen-terminated diamond surface were subject to active manipulation by an NC-AFM tip. Two different kinds of tip-induced island growth modes have been induced and are presented in Chap. 8.

In conclusion, the results obtained provide fundamental informations mandatory for the realization of a molecular quantum computer. In the process it was shown that NC-AFM is, under

proper circumstances, a very capable tool for imaging diamond surfaces with highest resolution, surpassing even what has been achieved with STM up to now. Particular attention was paid to the influence of transfer doping on the morphology of fullerenes on the hydrogenated diamond surface, revealing new possibilities for tailoring the self-assembly of molecules that have a high electron affinity.

10 Appendix

Contents

In the following, first results of an STM-assisted study of molecular deposition by pulse injection is presented. A running pulse injection setup is a prerequisite for the deposition of PEFs onto diamond surfaces under UHV conditions, which in turn is vital for a diamond quantum register as described in Chap. 4.

10.1 STM study of C_{60} deposited in solution by pulse valve injection

Figure 10.1: Saturated solution of C_{60} in toluene, featuring a characteristic violet color.

In this experiment, a saturated solution of C_{60} (purity: 99.95%) in toluene (purity: 99.5%) as depicted in Fig. 10.1 was deposited on the gold Au(111) surface. C_{60} was chosen because it is structurally almost identical with PEF. Therefore a analogues deposition behavior is to be expected.

Fullerenes are in general of low solubility, which hampers the deposition by pulse injection. An overview over a number of common C_{60} solvents is given in Tab. 10.1.

Solvent	C_{60} solubility in mmol/l
Acetone	0.001
Hexane	0.06
THF	0.08
Decane	0.10
Chloroform	0.22
Dichloromethane	0.35
Tetrachloromethane	0.44
Benzonitrile	0.57
Benzene	2.36
Toluene	3.89
Chlorobenzene	9.71
Carbon disulfide	11.0
1-Chloronaphthalene	70.8
Piperidin	74.0

Table 10.1: Solubility of C_{60} in common solvents at standard conditions [135].

As can be calculated, the solubility of C_{60} in toluene, for exam-

ple, amounts to only 2.8 g/l at standard conditions despite being one of the better C_{60} solvents. This equals a proportion of about 2400 solvent molecules per fullerene. There a only very few solvents exhibiting a notably higher solubility, for example carbon disulfide and 1-chloronaphthalene. Those solvents, however, are often either prone to strongly bind to the gold surface or are hardly available in the required purity.

Au(111) was chosen as a test substrate for two reasons mainly: On the one hand, a clean and atomically flat Au(111) surface can be easily prepared by means of sputtering and annealing. Hence, there is no need to lock a new sample into the UHV system for every deposition attempt. As a metallic surface, Au(111) can be imaged with STM, which requires significantly less time for the tip approach than NC-AFM, minimizing the time between deposition and imaging. STM in general also allows for faster and more stable scanning due to the tip being less susceptible for irreparable changes. In addition, the adsorption of thermally sublimated C_{60} on this surface was already studied before using STM, revealing preferential clustering of the fullerenes at step edges[136]. Hence there is a defined expected structure, which facilitates the distinction of C_{60} from impurities or solvent remnants on the surface.

In the experimental setup, the solenoid pulse valve (Parker Series 9, 50 µm orifice, operated with IOTA ONE valve driver) was mounted atop the load-lock of the VT AFM 25, resulting in a orifice-sample distance of approximately 12 cm.

The Au(111) surface was prepared by multiple cycles of argon sputtering (15 min at 2 keV Ar^+, 3×10^{-6} mbar) and subsequent annealing (800 K to 850 K for 60 m). The so prepared bare surface consists of terraces featuring the characteristic $(23 \times \sqrt{3})$ reconstruction known as “herringbone” structure.

When opening the pulse valve, the pressure in the load lock increases instantaneously by several orders of magnitude, from about 10^{-10} mbar to 10^{-6} mbar-10^{-5} mbar. This rise in pressure is short-timed, it peaks for a fraction of a second only and drops back to the 10^{-9} mbar regime within a few seconds due to continuous pumping of the load-lock. Interestingly, this pressure

signature is largely independent of the opening time, which was varied between 1 ms and 1 s. In the extreme case of 1 s opening time, the drop-back in pressure was observed even while the valve was still open, giving evidence for the aforementioned freezing of the orifice.

Before the actual deposition of the C_{60} solution, pure toluene was deposited onto the surface using the pulse valve. It was previously reported [137] that mobile solvent remnants may hamper the STM imaging of the surface. However, this was not observed in this case, no signs of the solvent were found on the surface. The images obtained after deposition did not differ from those previously obtained on a newly prepared surface.

Despite the freezing problem, some signs of a successful C_{60} deposition were observed on the gold surface. Clusters with an amorphous appearance and a height of 0.5 nm to 1.0 nm were imaged on the surface after deposition by five 5 ms injections in 60 s intervals (see Fig. 10.2). The height as as well as the clustering on a highly stepped surface region (step-bunches) are in agreement with what would be expected for C_{60} on the Au(111) surface. However, the internal structure of the clusters could not be further revealed.

A similar observation was made after opening the pulse valve seven times for 5 ms in 60 s intervals, again with the focus on a step.bunched surface region. As can be seen in Fig. 10.3, a number of adsorbates has clustered on the surface in this case as well. The height is again in good agreement with the height expected for C_{60} adsorbed to the Au(111) surface. However, it has to be kept in mind that the topography image is directly derived from the tip piezo motion, which in turn is regulated in order to maintain a constant tunneling current. Hence, the displayed height can only be directly compared when scanning surface regions with identical electronic structure. The interaction of the tip with C_{60} or other adsorbates can therefore differ from the interaction with the bare gold surface. An extreme example is apparent in Fig. 10.4, which displays the same surface region scanned with the same tip as in Fig. 10.3 and was obtained only minutes later with the same tunneling currant. Nonetheless, the adsorbates previously shown as protrusions are now imaged

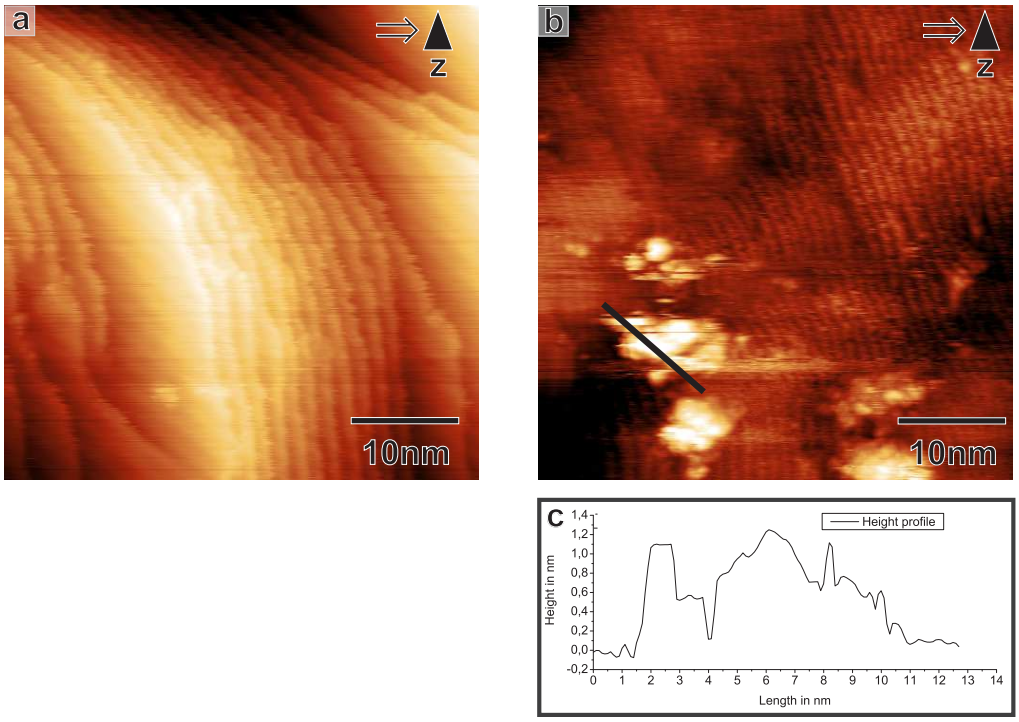

as holes.

In general, the adsorbates are predominately found in step-bunched surface regions, the terraces stay largely clean (see Fig. 10.4). This is coherent with previous STM observations of C_{60} decorating Au(111) step edges only.

Unfortunately, the results are only reproducible to some degree. Occasionally, no signs of deposition were observed at all or, in the opposite case, no stable scanning is possible because the surface appears to be covered in non-conducting material. This raises the suspicion that in this case the surface was coated with solvent molecules. Interestingly, though, even annealing up to 570 K was not sufficient to remove the adlayer and enable STM scanning on the surface.

Figure 10.2: a) STM topography image of the clean Au(111) surface region that features pronounced step bunching. b) STM topography image of the same sample after the pulsed deposition of C_{60}, featuring molecular cluster with a height of 8 - 12 Å.

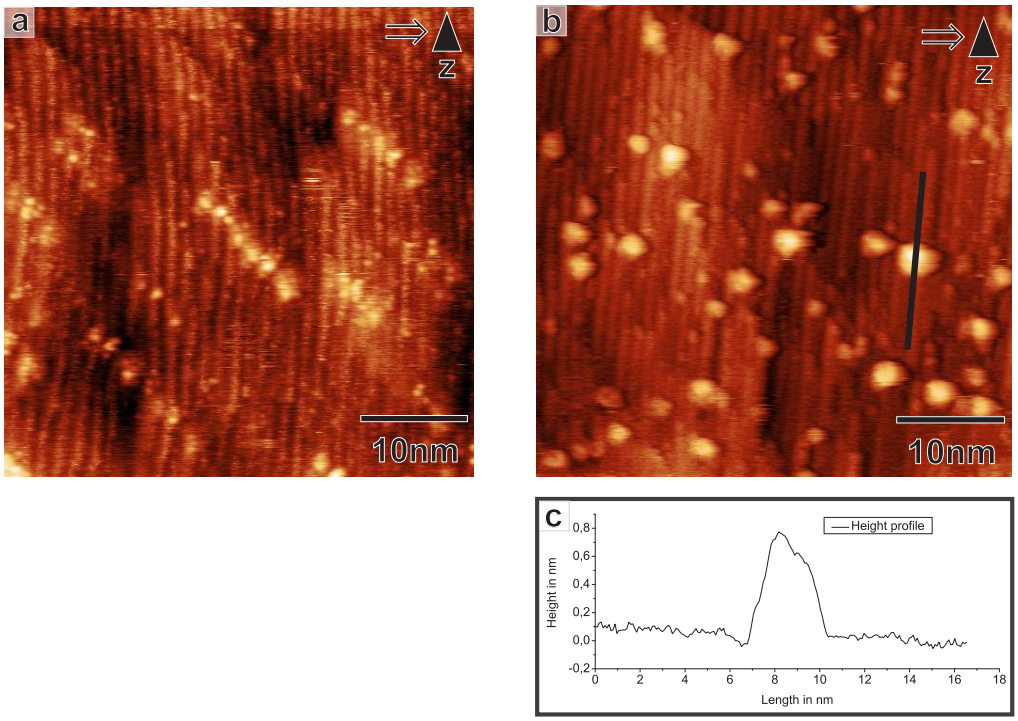

Figure 10.3: a) STM topography image of a highly step-bunched surface region of Au(111). Note that the image was taken with a manifold tip, imaging single protrusions multiple times. b) STM topography image of the same sample after the pulsed deposition of C_{60}, featuring molecular cluster with a height of about 8 Å.

10.2 Conclusion and possible improvements

The operation of a solenoid pulse valve for the deposition of molecules from solution was studied. Both STM and QCM measurements (see Chap. 5) in combination with mass spectroscopy were taken for this purpose. With both techniques, the injection and deposition of sample molecules could be detected. The amount deposited, however, does not directly correlate with the amount or duration of pulses. This is most likely due to a blockage of the orifice. The most likely explanation is a freezing of the solvent around the orifice upon opening the valve to the UHV system. Therefore, a well-controlled deposition of a specific amount of target molecules is not possible with the current setup.

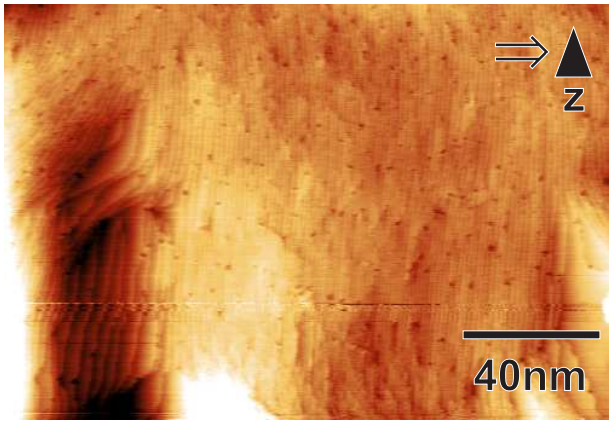

Figure 10.4: STM topography image of the Au(111) surface with supposed C_{60} adsorbed to it. The molecular cluster that appeared as bright protrusions in Fig. 10.2 are now imaged as dark holes.

In order to achieve a specific coverage of target molecules on a substrate by pulse injection, several modifications of the original setup could be envisioned. To prevent a possible freezing of the orifice upon injection of the solution, a heating device annealing the pulse valve is required. In addition, a pulse valve with a larger orifice will likely result in a higher yield. Another method to increase the yield would be to drastically shorten the distance between orifice and substrate. Although no striking differences were found in the deposition characteristics of the four solvents used in this study, further testing may help identifying solvents more suitable for the purpose of pules injection.

Bibliography

1. Y. Dickinson: The Book of Diamonds. Courier Dover Publications, 2001

2. S. Koizumi, C. Nebel, M. Nesladek: Physics and Applications of CVD Diamond. Wiley-VCH, 2008

3. M. V. Gurudev Dutt, L. Childress, L. Jiang, E. Togan, J. Maze, F. Jelezko, A. S. Zibrov, P. R. Hemmer, M. D. Lukin: Quantum register based on individual electronic and nuclear spin qubits in diamond.
Science **316**, 1312 (2007)

4. P. Neumann, N. Mizuochi, F. Rempp, P. Hemmer, H. Watanabe, S. Yamasaki, V. Jacques, T. Gaebel, F. Jelezko, J. Wrachtrup: Multipartite Entanglement Among Single Spins in Diamond.
Science **320**, 1326 (2008)

5. P. Neumann, R. Kolesov, B. Naydenov, J. Beck, F. Rempp, M. Steiner, V. Jacques, G. Balasubramanian, M. L. Markham, D. J. Twitchen, S. Pezzagna, J. Meijer, J. Twamley, F. Jelezko, J. Wrachtrup: Quantum register based on coupled electron spins in a room-temperature solid.
Nature Physics **6**, 249 (2010)

6. U. Troppmann: Studien zur Realisierbarkeit von Molekularem Quantencomputing, PhD Thesis, 2006

7. T. Gaebel, M. Domhan, I. Popa, C. Wittmann, P. Neumann, F. Jelezko, J. R. Rabeau, N. Stavrias, A. D. Greentree, S. Prawer, J. Meijer, J. Twamley,

P. R. HEMMER, J. WRACHTRUP: Room-temperature coherent coupling of single spins in diamond.
Nature Physics **2**, 408 (2006)

8. G. D. FUCHS, G. BURKARD, P. V. KLIMOV, D. D. AWSCHALOM: A quantum memory intrinsic to single nitrogen-vacancy centres in diamond.
Nature Physics **7**, 789 (2011)

9. H. TANAKA, T. KAWAI: Scanning tunneling microscopy imaging and manipulation of DNA oligomer adsorbed on Cu(111) surfaces by a pulse injection method.
Journal of Vacuum Science and Technology B **15**, 602 (1997)

10. G. BINNIG, C. QUATE, C. GERBER: Atomic Force Microscope.
Physical Review Letters **56**, 930 (1986)

11. G. BINNIG, H. ROHRER: Scanning Tunneling Microscopy - From Birth to Adolescence.
Reviews of Modern Physics **59**, 615 (1987)

12. F. OHNESORGE, G. BINNIG: True atomic resolution by atomic force microscopy through repulsive and attractive forces.
Science **260**, 1451 (1993)

13. P. RAHE, R. BECHSTEIN, J. SCHÃIJTTE, F. OSTENDORF, A. KÃIJHNLE: Repulsive interaction and contrast inversion in noncontact atomic force microscopy imaging of adsorbates.
Physical Review B **77**, 195410 (2008)

14. F. J. GIESSIBL: Advances in atomic force microscopy.
Reviews of Modern Physics **75**, 949 (2003)

15. F. J. GIESSIBL: Atomic Resolution of the Silicon (111)-(7x7) Surface by Atomic Force Microscopy.
Science **267**, 68 (1995)

16. L. Gross, F. Mohn, N. Moll, P. Liljeroth, G. Meyer: The Chemical Structure of a Molecule Resolved by Atomic Force Microscopy.
Science **325**, 1110 (2009)

17. IUPAC: Quantities, Units and Symbols in Physical Chemistry. Blackwell Science, 1993

18. T. Fukuma, K. Kobayashi, K. Matsushige, H. Yamada: True atomic resolution in liquid by frequency-modulation atomic force microscopy.
Applied Physics Letters **87**, 034101 (2005)

19. S. Rode, R. Stark, J. Lübbe, L. Tröger, J. Schütte, K. Umeda, K. Kobayashi, H. Yamada, A. Kühnle: Modification of a commercial atomic force microscopy for low-noise, high-resolution frequency-modulation imaging in liquid environment.
Review of Scientific Instruments **82** (2011)

20. H.-J. Butt, K. Graf, M. Kappl: Physics and Chemistry of Interfaces. WILEY-VCH, 2006

21. F. London: Zur Theorie und Systematik der Molekularkr äfte.
Zeitschrift für Physik **63**, 245 (1930)

22. J. N. Israelachvili: Intermolecular and Surface Forces. 1985

23. F. J. Giessibl: Forces and frequency shifts in atomic-resolution dynamic-force microscopy.
Physical Review B **56**, 16010 (1997)

24. H. C. Hamaker: The London-van der Waals attraction between spherical particles.
Physica **4**, 1058 (1937)

25. M. Nonnenmacher, M. P. O'Boyle, H. K. Wickramasinghe: Kelvin probe force microscopy.
Applied Physics Letters **58**, 2921 (1991)

26. Y. SUGIMOTO, P. POU, M. ABE, P. JELINEK, R. PÈREZ, S. MORITA, O. CUSTANCE: Chemical identification of individual surface atoms by atomic force microscopy.
Nature **446**, 64 (2007)

27. S. J. O'SHEA, N. N. GOSVAMI, L. T. W. LIM, W. HOFBAUER: Liquid Atomic Force Microscopy: Solvation Forces, Molecular Order, and Squeeze-Out.
Japanese Journal of Applied Physics **49**, 08LA01 (2010)

28. I. STALLCUP, R. E., J. M. PEREZ: Scanning Tunneling Microscopy Studies of Temperature-Dependent Etching of Diamond (100) by Atomic Hydrogen.
Physical Review Letters **86**, 3368 (2001)

29. H. KAWARADA: Hydrogen-terminated diamond surfaces and interfaces.
Surface Science Reports **26**, 205 (1996)

30. D. N. BATCHELDER, R. O. SIMMONS: Lattice constants and thermal expansivities of silicon and of calcium fluoride between 6 and 322 K.
Journal of Chemical Physics **41**, 2324 (1964)

31. G. W. RUBLOFF: Far Ultraviolet Reflectance Spectra and Electronic Structure of Ionic Crystals.

32. OHARA CORPORATION: Optical Crystals - Calcium Fluoride Datasheet

33. M. BATZILL, K. J. SNOWDON: Shape transition of calcium islands formed by electron-stimulated desorption of fluorine from a CaF_2(111) surface.
Applied Physics Letters **77**, 1955 (2000)

34. M. REICHLING, C. BARTH: Scanning force imaging of atomic size defects on the CaF_2 (111) surface.
Physical Review Letters **83**, 768 (1999)

35. H. W. KROTO, J. R. HEATH, S. C. O'BRIEN, R. F. CURL,

R. E. SMALLEY: C_{60}: Buckminsterfullerene.
Nature **318**, 162 (1985)

36. R. C. HADDON: Electronic structure, conductivity and superconductivity of alkali metal doped (C_{60}).
Acc. Chem. Res. **25**, 127 (1992)

37. S. Z. LIU, Y. J. LU, M. M. KAPPES, J. A. IBERS: The structure of the C_{60} molecule - x-ray crystal-structure determination of a twin at 110K.
Science **254**, 408 (1991)

38. W. KRÄTSCHMER, L. D. LAMB, K. FOSTIROPOULOS, D. R. HUFFMAN: Solid C_{60}: a new form of carbon.
Nature (London, United Kingdom) **347**, 354 (1990)

39. J. C. LI, T. YU, M. S. YE, X. J. FAN: The effects of the vacuum sublimation process on the composition of C_{60}/C_{70} films.
Thin Solid Films **345**, 236 (1999)

40. J. ABREFAH, D. R. OLANDER, M. BALOOCH, W. J. SIEKHAUS: Vapor pressure of Buckminsterfullerene.
Applied Physics Letters **60**, 1313 (1992)

41. E. A. KATZ: Potential of fullerene-based materials for the utilization of solar energy.
Physics of the Solid State **44**, 647 (2002)

42. S. H. YANG, C. L. PETTIETTE, J. CONCEICAO, O. CHESHNOVSKY, R. E. SMALLEY: UPS of Buckminsterfullerene and other large clusters of Carbon.
Chemical Physics Letters **139**, 233 (1987)

43. S. J. SQUE, R. JONES, S. OEBERG, P. R. BRIDDON: Transfer doping of diamond: Buckminsterfullerene on hydrogenated, hydroxylated, and oxygenated diamond surfaces.
Journal of Materials Science: Materials in Electronics **17**, 459 (2006)

44. P. STROBEL, M. RIEDEL, J. RISTEIN, L. LEY: Surface

transfer doping of diamond.
Nature **430**, 439 (2004)

45. S. I. TROYANOV, P. A. TROSHIN, O. V. BOLTALINA, I. N. IOFFE, L. N. SIDOROV, E. KEMNITZ: Two isomers of $C_{60}F_{48}$: An indented fullerene.
Angewandte Chemie-International Edition **40**, 2285 (2001)

46. S. KAWASAKI, T. AKETA, H. TOUHARA, F. OKINO, O. V. BOLTALINA, I. V. GOLDT, S. I. TROYANOV, R. TAYLOR: Crystal structures of the fluorinated fullerenes $C_{60}F_{36}$ and $C_{60}F_{48}$.
Journal of Physical Chemistry B **103**, 1223 (1999)

47. J. S. CHICKOS, W. E. ACREE: Enthalpies of vaporization of organic and organometallic compounds, 1880-2002.
Journal of Physical and Chemical Reference Data **32**, 519 (2003)

48. R. HETTICH, C. M. JIN, R. COMPTON: Determination of the electron-affinities of fluorinated fullerenes ($C_{60}F_{44,46}$, $C_{70}F_{52,54}$) by Fourier-transfrom mass-spectrometry.
International Journal of Mass Spectrometry and Ion Processes **138**, 263 (1994)

49. P. STROBEL, M. RIEDEL, J. RISTEIN, L. LEY, O. BOLTALINA: Surface transfer doping of diamond by fullerene.
Diamond and Related Materials **14**, 451 (2005)

50. F. P. BUNDY, W. A. BASSETT, M. S. WEATHERS, R. J. HEMLEY, H. K. MAO, A. F. GONCHAROV: The pressure-temperature phase and transformation diagram for carbon; Updated through 1994.
Carbon **34**, 141 (1996)

51. G. DAVIES, T. EVANS: Graphitization of diamond at zero pressure and at a high-pressure.
Proceedings of the Royal Society of London Series A **328**, 413 (1972)

52. A. G. WHITTAKER: Carbon - new view of its high-temperature behavior.
Science **200**, 763 (1978)

53. S. SQUE: Personal website of Steve Sque (http://www.stevesque.com/diamond/structure/)

54. J. E. FIELD: Properties of Natural and Synthetic Diamond,. Academic Press, 1992

55. M. E. STRAUMANIS, E. Z. AKA: Precision determination of lattice parameter, coefficient of thermal expansion and atomic weight of carbon in diamond.
Journal of the American Chemical Society **73**, 5643 (1951)

56. S. DIMITRIJEV: Principles of Semiconductor Devices. Oxford University Press, 2007

57. J. SUNG, J. LIN: Diamond Nanotechnology: Synthesis and Applications. Pan Stanford Publishing Pte. Ltd., 2009

58. C. E. NEBEL: Electronic properties of CVD diamond.
Semiconductor Science and Technology **18**, S1 (2003)

59. W. SASLOW, BERGSTRE.TK, M. L. COHEN: Band structure and optical properties of diamond.
Physical Review Letters **16**, 354 (1966)

60. D. AWSCHALOM: Awschalom group, University of California Santa Barbara (http://awsch-web.physics.ucsb.edu)

61. R. H. WENTORF: Cubic form of boron nitride.
Journal of Chemical Physics **26**, 956 (1957)

62. R. H. TELLING, C. J. PICKARD, M. C. PAYNE, J. E. FIELD: Theoretical strength and cleavage of diamond.
Physical Review Letters **84**, 5160 (2000)

63. DIAMOND MATERIALS: The CVD Diamond Booklet (available at www.diamond-materials.com). (2011)

64. E. HECHT: Optics. Pearson Higher Education

65. L. H. WEI, P. K. KUO, R. L. THOMAS, T. R. ANTHONY, W. F. BANHOLZER: Thermal conductivity of isotopically modified single-crystal diamond.
Physical Review Letters **70**, 3764 (1993)

66. L. TANG, C. TSAI, W. W. GERBERICH, L. KRUCKEBERG, D. R. KANIA: Biocompatibility of chemical-vapor-deposited diamond.
Biomaterials **16**, 483 (1995)

67. P. JOHN, N. POLWART, C. E. TROUPE, J. I. B. WILSON: The oxidation of (100) textured diamond.
Diamond and Related Materials **11**, 861 (2002)

68. F. K. DE THEIJE, O. ROY, N. J. VAN DER LAAG, W. J. P. VAN ENCKEVORT: Oxidative etching of diamond.
Diamond and Related Materials **9**, 929 (2000)

69. C. A. KLEIN, G. F. CARDINALE: Youngs modulus and poissons ratio of cvd diamond.
Diamond and Related Materials **2**, 918 (1993)

70. A. VLASOV, V. RALCHENKO, S. GORDEEV, D. ZAKHAROV, I. VLASOV, A. KARABUTOV, P. BELOBROV: Thermal properties of diamond/carbon composites.
Diamond and Related Materials **9**, 1104 (2000)

71. C. KITTEL: Einführung in die Festkörperphysik. Oldenburg, 2005

72. J. WRACHTRUP, F. JELEZKO: Processing quantum information in diamond.
Journal of Physics: Condensed Matter **18**, S807 (2006)

73. T. M. WILLEY, C. BOSTEDT, T. VAN BUUREN, J. E. DAHL, S. G. LIU, R. M. K. CARLSON, L. J. TERMINELLO, T. MOLLER: Molecular limits to the quantum confinement model in diamond clusters.
Physical Review Letters **95** (2005)

74. J. WRACHTRUP, S. Y. KILIN, A. P. NIZOVTSEV: Quantum computation using the C-13 nuclear spins near the single NV defect center in diamond.
Optics and Spectroscopy **91**, 429 (2001)

75. A. D. GREENTREE, B. A. FAIRCHILD, F. M. HOSSAIN, S. PRAWER: Diamond integrated quantum photonics.
Materials Today **11**, 22 (2008)

76. K. B. HOLT: Diamond at the nanoscale: applications of diamond nanoparticles from cellular biomarkers to quantum computing.
Philosophical Transactions of the Royal Society a-Mathematical Physical and Engineering Sciences **365**, 2845 (2007)

77. W. HARNEIT: Fullerene-based electron-spin quantum computer.
Physical Review A: Atomic, Molecular, and Optical Physics **65**, 032322 (2002)

78. W. HARNEIT, K. HÜBENER, B. NAYDENOV, S. SCHÄFER, M. SCHELOSKE: $N@C_{60}$ quantum bit engineering.
Physica Status Solidi B: Basic Solid State Physics **244**, 3879 (2007)

79. W. HARNEIT, C. MEYER, A. WEIDINGER, D. SUTER, J. TWAMLEY: Architectures for a spin quantum computer based on endohedral fullerenes.
Physica Status Solidi B: Basic Research **233**, 453 (2002)

80. K. HUEBENER, R. S. SCHOENFELD, J. KNIEPERT, C. OELMUELLER, W. HARNEIT: ODMR of NV centers in nano-diamonds covered with $N@C_{60}$.
Physica Status Solidi B-Basic Solid State Physics **245**, 2013 (2008)

81. A. KRÜGER: Neue Kohlenstoffmaterialien. B.G. Teubner Verlag, 2007

82. G. KERN, J. HAFNER, J. FURTHMÜLLER, G. KRESSE:

(2x1) reconstruction and hydrogen-induced de-reconstruction of the diamond(100) and (111) surfaces.
Surface Science **352**, 745 (1996)

83. S. H. YANG, D. A. DRABOLD, J. B. ADAMS: Ab-inition study of diamond C(100) surfaces.
Physical Review B **48**, 5261 (1993)

84. P. G. LURIE, J. M. WILSON: Diamond surface: 1. structure of clean surface and interaction with gases and metals.
Surface Science **65**, 453 (1977)

85. A. J. MAYNE, D. RIEDEL, G. COMTET, G. DUJARDIN: Atomic-scale studies of hydrogenated semiconductor surfaces.
Progress in Surface Science **81**, 1 (2006)

86. C. NÜTZENADEL, O. M. KÜTTEL, L. DIEDERICH, E. MAILLARD-SCHALLER, O. GRÖNING, L. SCHLAPBACH: STM investigations with atomic resolution on the (2x1) monohydride natural doped diamond (100) surface.
Surface Science **369**, L111 (1996)

87. K. BOBROV, A. J. MAYNE, G. DUJARDIN: Atomic-scale imaging of insulating diamond through resonant electron injection.
Nature (London, United Kingdom) **413**, 616 (2001)

88. S. P. MEHANDRU, A. B. ANDERSON: Adsorption of H, Ch_3, CH_2 and C_2H_2 on 2x1 reconstructed diamond (100) - theoretical-study of structures, bonding, and migration.
Surface Science **248**, 369 (1991)

89. J. B. CUI, J. RISTEIN, L. LEY: Electron affinity of the bare and hydrogen covered single crystal diamond (111) surface.
Physical Review Letters **81**, 429 (1998)

90. F. MAIER, J. RISTEIN, L. LEY: Electron affinity of plasma-hydrogenated and chemically oxidized diamond (100) sur-

faces.
Physical Review B **64**, 165411 (2001)

91. M. I. LANDSTRASS, K. V. RAVI: Resistivity of chemical vapor deposited diamond films.
Applied Physics Letters **55**, 975 (1989)

92. F. MAIER, M. RIEDEL, B. MANTEL, J. RISTEIN, L. LEY: Origin of surface conductivity in diamond.
Physical Review Letters **85**, 3472 (2000)

93. K. BOBROV, G. COMTET, G. DUJARDIN, L. HELLNER: Electronic structure of the hydrogenated diamond C(100)-(2 x 1): H surface.
Surface Science **482**, 437 (2001)

94. K. BOBROV, A. MAYNE, G. COMTET, G. DUJARDIN, L. HELLNER, A. HOFFMAN: Atomic-scale visualization and surface electronic structure of the hydrogenated diamond C(100)-(2x1): H surface.
Physical Review B **68**, 8 (2003)

95. L. HELLNER, A. J. MAYNE, R. BERNARD, G. DUJARDIN: Hydrogenated diamond crystal C(100) conductivity studied by STM.
Diamond and Related Materials **14**, 1529 (2005)

96. T. TSUNO, T. TOMIKAWA, S. SHIKATA, T. IMAI, N. FUJIMORI: Diamond (001) single-domain 2x1 surface grown by chemical-vapor-deposition.
Applied Physics Letters **64**, 572 (1994)

97. AGILENT TECHNOLOGIES: Ion Getter Pump sales brochure. (2012)

98. S. WEIDLICH: Nachweis der Implantation einzelner Ionen in Festkörpern, Diploma thesis, 2011

99. J. MELNGAILIS: Focused ion-beam technology and applications.
Journal of Vacuum Science and Technology B **5**, 469 (1987)

100. J. GIERAK: Focused ion beam technology and ultimate applications.
Semiconductor Science and Technology **24** (2009)

101. F. LOSKE, J. LÜBBE, J. SCHÜTTE, M. REICHLING, A. KÜHNLE: Quantitative description of C_{60} diffusion on an insulating surface.
Physical Review B **82**, 155428 (2010)

102. P. RAHE, R. LINDNER, M. KITTELMANN, M. NIMMRICH, A. KÜHNLE: From dewetting to wetting molecular layers: C_{60} on $CaCO_3(10\bar{1}4)$ as a case study.
Physical Chemistry Chemical Physics **14**, 6544 (2012)

103. R. E. STALLCUP, J. M. PEREZ: Atomic structure of steps and defects on the clean diamond (100)-2x1 surface studied using ultrahigh vacuum scanning tunneling microscopy.
Applied Physics Letters **81**, 4538 (2002)

104. R. BECHSTEIN, C. GONZÁLEZ, J. SCHÜTTE, P. JELÍNEK, R. PÉREZ, A. KÜHNLE: All-inclusive imaging of the rutile $TiO_2(110)$ surface using NC-AFM.
Nanotechnology **20**, 505703 (2009)

105. S. HIRTH, F. OSTENDORF, M. REICHLING: Lateral manipulation of atomic size defects on the $CaF_2(111)$ surface.
Nanotechnology **17**, S148 (2006)

106. S. TORBRÜGGE, M. REICHLING, A. ISHIYAMA, S. MORITA, O. CUSTANCE: Evidence of Subsurface Oxygen Vacancy Ordering on Reduced CeO2(111).
Physical Review Letters **99**, 056101 (2007)

107. P. RAHE, J. SCHÜTTE, A. KÜHNLE: NC-AFM contrast formation on the calcite $(10\bar{1}4)$ surface.
Journal of Physics-Condensed Matter **24**, 084006 (2012)

108. P. RAHE, M. NIMMRICH, A. GREULING, J. SCHÜTTE, I. STARÁ, J. RYBÁČEK, G. HUERTA-ANGELES, I. STARÝ, M. ROHLFING, A. KÜHNLE: Toward Molecular Nanowires Self-Assembled on an Insulating Substrate:

Heptahelicene-2-carboxylic acid on Calcite ($10\bar{1}4$).
Journal of Physical Chemistry C **114**, 1547 (2010)

109. S. Maier, L.-A. Fendt, L. Zimmerli, T. Glatzel, O. Pfeiffer, F. Diederich, E. Meyer: Nanoscale engineering of molecular porphyrin wires on insulating surfaces.
Small **4**, 1115 (2008)

110. S. A. Burke, J. M. Mativetsky, R. Hoffmann, P. Grütter: Nucleation and submonolayer growth of C_{60} on KBr.
Physical Review Letters **94**, 096102 (2005)

111. T. Dienel, C. Loppacher, S. C. B. Mannsfeld, R. Forker, T. Fritz: Growth-mode-induced narrowing of optical spectra of an organic adlayer.
Advanced Materials **20**, 959 (2008)

112. L. H. Chua, R. B. Jackman, J. S. Foord, P. R. Chalker, C. Johnston, S. Romani: Interaction of hydrogen with chemical-vapor-deposited diamond surfaces - a thermal desorption study.
Journal of Vacuum Science and Technology A **12**, 3033 (1994)

113. P. Rahe, R. Bechstein, A. Kühnle: Vertical and lateral drift corrections of scanning probe microscopy images.
Journal of Vacuum Science and Technology B **28**, C4E31 (2010)

114. D. R. Alfonso, D. A. Drabold, S. E. Ulloa: Structural, electronic and vibrational properties of Diamond(100), Diamond(111) and Diamond(110) Surfaces from ab-initio calculations.
Physical Review B **51**, 14669 (1995)

115. Y. Yu, C. Z. Gu, L. F. Xu, S. B. Zhang: Ab initio structural characterization of a hydrogen-covered diamond (001) surface.
Physical Review B **70**, 125423 (2004)

116. T. HOM, W. KISZENICK, B. POST: Accurate lattice-constants from multiple reflection measurements: 2. Lattice constants of germanium, silicon and diamond.
Journal of Applied Crystallography **8**, 457 (1975)

117. Y. M. L. YANG, M. P. DEVELYN: Structure and energetics of clean and hydrogenated diamond(100) surfaces by molecular mechanics.
Journal of the American Chemical Society **114**, 2796 (1992)

118. Y. L. KUANG, Y. F. WANG, N. LEE, A. BADZIAN, T. BADZIAN, T. T. TSONG: Surface structure of homoepitaxial diamond (001) films, a scanning tunneling microscopy study.
Applied Physics Letters **67**, 3721 (1995)

119. P. KRUGER, J. POLLMANN: Dimer reconstruction of Diamond(001), Si(001) and Ge(001) surfaces.
Physical Review Letters **74**, 1155 (1995)

120. F. H. HERBSTEIN: Methods of measuring Debye temperatures and comparison of results for some cubic crystals.
Advances in Physics **10**, 313 (1961)

121. D. J. CHADI: Stabilities of single-layer and bilayer steps on Si(001) surfaces.
Physical Review Letters **59**, 1691 (1987)

122. K. BOBROV, A. J. MAYNE, A. HOFFMAN, G. DUJARDIN: Atomic-scale desorption of hydrogen from hydrogenated diamond surfaces using the STM.
Surface Science **528**, 138 (2003)

123. P. STROBEL, J. RISTEIN, L. LEY, K. SEPPELT, I. V. GOLDT, O. BOLTALINA: Surface conductivity induced by fullerenes on diamond: Passivation and thermal stability.
Diamond and Related Materials **15**, 720 (2006)

124. T. OUYANG, K. P. LOH, D. C. QI, A. T. S. WEE, M. NESLADEK: Chemical bonding of fullerene and fluorinated ful-

lerene on bare and hydrogenated diamond.
ChemPhysChem **9**, 1286 (2008)

125. S. A. Burke, J. M. Mativetsky, S. Fostner, P. Grütter: C_{60} on alkali halides: Epitaxy and morphology studied by noncontact AFM.
Physical Review B: Condensed Matter and Materials Physics **76**, 035419 (2007)

126. M. Körner, F. Loske, M. Einax, A. Kühnle, M. Reichling, P. Maass: Second-Layer Induced Island Morphologies in Thin-Film Growth of Fullerenes.
Physical Review Letters **107**, 016101 (2011)

127. P. A. Redhead: Thermal desorption of gases.
Vacuum **12**, 203 (1962)

128. D. Sanvitto, M. De Seta, F. Evangelisti: Growth of thin C_{60} films on hydrogenated Si(100) surfaces.
Surface Science **452**, 191 (2000)

129. A. L. Smith, M. V. Korobov: Solubility of the fullerenes.
Abstracts of Papers of the American Chemical Society **218**, U726 (1999)

130. X. D. Wang, T. Hashizume, H. Shinohara, Y. Saito, Y. Nishina, T. Sakurai: Adsorption of C_{60} and C_{84} on the Si(100)2x1 surface studied by using the scanning tunneling microscope.
Physical Review B **47**, 15923 (1993)

131. B. Rezek: Atomic and Kelvin force microscopy applied on hydrogenated diamond surfaces.
New Diamond and Frontier Carbon Technology **15**, 275 (2005)

132. C. Toma, A. Volodin, G. Bogdan, W. Deferme, K. Haenen, M. Nesladek, C. Van Haesendonck: Tip voltage controlled local modification of hydrogenated diamond surface with an atomic force microscope.

Physica Status Solidi a-Applications and Materials Science **204**, 2920 (2007)

133. B. W. SMITH, M. MONTHIOUX, D. E. LUZZI: Encapsulated C_{60} in carbon nanotubes.
Nature **396**, 323 (1998)

134. S. C. BENJAMIN, A. ARDAVAN, G. A. D. BRIGGS, D. A. BRITZ, D. GUNLYCKE, J. JEFFERSON, M. A. G. JONES, D. F. LEIGH, B. W. LOVETT, A. N. KHLOBYSTOV, S. A. LYON, J. J. L. MORTON, K. PORFYRAKIS, M. R. SAMBROOK, A. M. TYRYSHKIN: Towards a fullerene-based quantum computer.
Journal of Physics-Condensed Matter **18**, S867 (2006)

135. M. KOROBOV, A. SMITH: Solubility of the Fullerenes. In: *Fullerenes*. Wiley-Blackwell, 2000

136. E. I. ALTMAN, R. J. COLTON: Nucleation, growth and structure of fullerene films on Au(111).
Surface Science **279**, 49 (1992)

137. L. GRILL: Large molecules on surfaces: deposition and intramolecular STM manipulation by directional forces.
Journal of Physics-Condensed Matter **22** (2010)

Publications and Presentations

(presenting author underlined)

Publications in peer-reviewed journals

- **Transition of Molecule Orientation during Adsorption of Terephthalic Acid on Rutile TiO_2(110)**
  Rahe, P; Nimmrich, M; Nefedov, A; Naboka, M; Wöll, C; Kühnle, A
  Journal of Physical Chemistry C **113**, 50, 17471 (2009)

- **Toward Molecular Nanowires Self-Assembled on an Insulating Substrate: Heptahelicene-2-carboxylic acid on Calcite** ($10\bar{1}4$)
  Rahe, P; Nimmrich, M; Greuling, A; Schütte, J; Starà, IG; Rybàček, J; Huerta-Angeles, G; Starỳ, I; Rohlfing, M; Kühnle, A
  Journal of Physical Chemistry C **114**, 3, 1547 (2010)

- **Atomic-resolution imaging of clean and hydrogen-terminated C(100)-(2x1) diamond surfaces using non-contact AFM**
  Nimmrich, M; Kittelmann, M; Rahe, P; Mayne, AJ; Dujardin, G; von Schmidsfeld, A; Reichling, M; Harneit, W; Kühnle, A
  Physical Review B **81**, 20, 201403(R) (2010)

- **Racemic and Optically Pure Heptahelicene-2-carboxylic Acid: Its Synthesis and Self-Assembly into Nanowire-**

Like Aggregates
Rybàček, J; Huerta-Angeles, G; Kollàrovič, A; Starà, IG; Starỳ, I; Rahe, P; Nimmrich, M; Kühnle, A
European Journal of Organic Chemistry **5**, 853 (2011) (cover)

- **On-Surface Covalent Linking of Organic Building Blocks on a Bulk Insulator**
  Kittelmann, M; Rahe, P; Nimmrich, M; Hauke, CM; Gourdon,A; Kühnle, A
  ACS Nano **5**, 11, 8420 (2011)

- **Molecular Self-Assembly of Enantiopure Heptahelicene-2-Carboxylic Acid on Calcite** ($10\bar{1}4$))
  Hauke, CM; Rahe, P; Nimmrich,M; Schütte, J; Kittelmann, M; Starà, IG; Starỳ, I; Rybàček, J; Kühnle, A
  Journal of Physical Chemistry C **116**, 7, 4637 (2011)

- **From dewetting to wetting molecular layers: C_{60} on $CaCO_3$($10\bar{1}4$) as a case study**
  Rahe, P; Lindner,R; Kittelmann,M; Nimmrich, M; Kühnle, A
  Physical Chemistry Chemical Physics **14**, 18, 6544 (2012)

- **Influence of charge transfer doping on the morphologies of C_{60} islands on hydrogenated diamond C(100)-(2x1)**
  Nimmrich, M; Kittelmann, M; Rahe, P; Harneit, W; Mayne, AJ; Dujardin, G; Kühnle, A
  Physical Review B **85**, 3, 035420 (2012)

- **Substrate templating upon self-assembly of hydrogen-bonded molecular networks on an insulating surface**
  Rahe, P; Nimmrich, M; Kühnle, A
  SMALL accepted May 2012

Conference Talks

- **NC-AFM on hydrogenated and on clean diamond (100)**
  Nimmrich, M; Kittelmann, M; Rahe, P; Mayne, AJ; Dujardin, G; von Schmidsfeld, A; Reichling, M; Harneit, W; Kühnle, A
  (NCAFM 2010, Kanazawa, Japan)

- **Effect of Transfer Doping on the Structure Formation of C_{60} Self-Assembly on Hydrogenated Diamond C(100)-(2x1):H**
  Nimmrich, M; Kittelmann, M; Rahe, P; Harneit, W; Mayne, AJ; Dujardin, G; Kühnle, A
  (MRS Fall Meeting 2011, Boston, USA)

- **The NV Color Center Qubit in Diamond as Readout for Molecular Qubits**
  Harneit, W; Schönfeld, RS; Nimmrich, M; Kühnle, A
  (MRS Fall Meeting 2011, Boston, USA)

- **Self-assembly and chiral recognition of heptahelicene acid on an insulating surface**
  Hauke, CM; Rahe, P; Nimmrich,M; Schütte, J; Kittelmann, M; Starà, IG; Starý, I; Rybàček, J; Kühnle, A
  (ECOSS 28, Wroclaw, Poland)

- **On-surface covalent linking on an insulating substrat**
  Kittelmann, M; M; Rahe, P; Nimmrich, M; Hauke, CM; Gourdon,A; Kühnle, A
  (ECOSS 28, Wroclaw, Poland)

- **NC-AFM Aufnahmen von reinem und wasserstoffterminierten Diamant C(100)**
  Kittelmann, M; Nimmrich, M; Rahe, P; Mayne, AJ; Dujardin, G; von Schmidsfeld, A; Reichling, M; Harneit, W; Kühnle, A
  (DPG 2011, Dresden, Germany)

- **Phase transition of a molecular film and on-surface covalent linking**

Kittelmann, M; Rahe, P; Hauke, CM; Nimmrich, M; Kühnle,A
(NCAFM 2011, Lindau, Germany)

- **Adsorption and structure formation of organic molecules on $CaCO_3(10\bar{1}4)$ - Impact for molecular self-assembly on insulating substrates**
  Rahe, P; Nimmrich, M; Schütte, J; Kittelmann, M; Kühnle, A
  (NCAFM 2011, Lindau, Germany)

Poster Presentations

- **Atomic-resolution imaging of high-purity diamond (100) using non-contact AFM**
  Nimmrich, M; Kittelmann, M; Rahe, P; Mayne, AJ; Dujardin, G; Reichling, M; Harneit, W; Kühnle, A
  (AAFMT 2011, Karlsruhe, Germany)

- **Adsorption and self-assembly of C_{60} on hydrogenated and pure diamond C(100)**
  Nimmrich, M; Kittelmann, M; Rahe, P; Kühnle, A
  (ECOSS 28, Wroclaw, Poland)

- **Molecular Self-Assembly on Calcite**
  Rahe, P; Nimmrich, M; Greuling, A; Schütte, J; Starà, IG; Rybàček, J; Huerta-Angeles, G; Starỳ, I; Rohlfing, M; Kühnle, A
  (NCAFM 2009, New Haven, USA)

- **Creating 1D nanostructures: Heptahelicene-carboxylic acid on calcite**
  Rahe, P; Nimmrich, M; Schütte, J; Kühnle, A
  (MRS Fall Meeting 2010, Boston, USA)

- **Chiral recognition and homochiral island formation on an insulating substrate**
  Hauke, CM; Rahe, P; Nimmrich,M; Schütte, J; Kittelmann, M; Starà, IG; Starỳ, I; Rybàček, J; Kühnle, A
  (NCAFM 2011, Lindau, Germany)